

Université du Québec
Institut National de la Recherche Scientifique
Centre Énergie, Matériaux et Télécommunication (INRS-EMT)

Generation, characterization and applications of ultrashort laser pulses

By

Alborz Ehteshami

A thesis submitted for the achievement of the degree of

Master of Science, M.Sc

in Energy and Materials Sciences

Jury Members

President of the jury
and Internal Examiner

François Vidal
INRS-EMT

External Examiner

Feruz Ganikhanov
*University of Rhode
Island*

Director of Research

François Légaré
INRS-EMT

DEDICATION

This thesis is dedicated to my beloved

Parents

&

Siblings

ACKNOWLEDGEMENTS

It is my proud privilege to convey my sincere gratitude to my supervisor, Prof. François Légaré. I am grateful for the opportunity to have joined his team. I believe his patience and guidance eased my transition into this field. Moreover, his insightful feedback pushed me to sharpen my thinking and brought my work to a higher level.

Throughout the writing of this dissertation, I have received a great deal of support and assistance from my good friend Arash Aghigh. I owe a debt of gratitude to him. Afterwards, I would like to thank Reza Safaei, who introduced me to INRS, and Légaré's team. Reza's support continued throughout the entire duration of my study. I am also grateful to my friend and colleague Elissa Haddad for her support and assistance on the French interpretation.

This master thesis has been carried out at National Institute of Scientific Research (INRS), and a number of people including the technical staff of the Advanced Laser Light Source (ALLS) deserve recognitions for their support and help. It's hardly possible to think of conduction experiments at ALLS without the support of Philippe Lassonde and Antoine Laramée. They are always happy to share their experience, and I've learned a lot from them.

I would like to express my gratitude to Dr Atiye Pezeshki and Azza Hadj Youssef for their contribution. I have collaborated with both of them, and they were very professional and supporting during each of these individual projects.

Lastly, my family (Morteza, Shabahang, Niloofar and Sahand) have been an inspiration throughout my life. I would like to give special thanks for their support and love throughout my study.

FORWARD CREDITS

- In the experiment conducted in section 3.5, the Strontium Titanate thin film sample was prepared by Azza Hadj Youssef a fellow PhD candidate from Prof. Andreas Peter Ruediger team and I was in charge of demonstrating inversion symmetry break using second harmonic generation microscopy.
- In the experiment conducted in section 3.6.2, the fundamental idea of using molecular architecture to enhance second harmonic generation in Transition metal dichalcogenides (TMDs) was proposed by Prof. Emanuele Origio and the follow up experiments were conducted in collaboration among two teams. Dr. Atiye Pezeshki was in charge of preparing the 2DM hybrids and I was in charge of investigating the enhance of second harmonic generation using laser scanning microscopy.

ABSTRACT

During my M.Sc. at INRS, I worked on three topics: (1) To transfer the concept of Frequency Resolved Optical Switching (FROSt) to pulse characterization in microscopy. (2) To use ultrashort laser pulses for material characterization using second harmonic generation optical microscopy. (3) To develop a novel technique for the compression of laser pulses.

FROSt is based on a pump-probe setup where the pump creates a transient gate and the probe are the pulses to characterize. The transient gate is established by using a pump to induce a change in the transmissivity of a material by photoexciting electrons from the valence band to the conduction band. Thus, the important requirement of using FROSt is to have sufficient pump intensity to photoexcite the material. During my M.Sc. thesis, I have worked to implement this technique for the temporal characterization of an ultrafast Ti:Sapphire laser oscillator used in our non-linear microscopy lab. The goal was to have the capability to measure the temporal profile of laser pulses in the focus of a high numerical aperture microscope objective. Even though we have not reach success yet with this goal, we know what to do in the future to implement FROSt for this application.

Working on the implementation of FROSt for the microscopy lab encouraged me to become familiar with the nonlinear microscopy world. Second harmonic generation (SHG) is a second order nonlinear effect, which only occurs when the inversion symmetry of the medium is broken. Implementing this concept inside a microscopic system creates a powerful measurement technique capable of analyzing symmetry properties. transition metal dichalcogenide (TMD) belongs to a big part of two-dimensional materials (2DMs) family in which the inversion symmetry of the medium is governed by the number of layers. Alternation of the exciton charging effects in this family leads to tunability in the SHG emission from this medium. This concept has been demonstrated using electrostatical doping and during my M.Sc. thesis, I worked on the evaluation of attaining the same outcome by manipulating the molecular architecture (stacking a 2D continuous molecular layer into a two-dimensional building block to manipulate the properties). We have demonstrated this concept in a small magnitude. This work was achieved in collaboration with the group of Prof. Emanuele Orgiu and under his scientific leadership.

A significant number of applications like high harmonics generation (HHG) demands high pulse energy to reach high peak power. Principally, the peak intensity of the pulse is inversely proportional to the pulse temporal duration and thus nonlinear post temporal compression plays an important role. The product of pulse temporal duration and spectral width is known as the time-bandwidth product which governs the limits and boundaries of pulse temporal duration. In non-linear pulse compression, to extend the pulse temporal compression, the spectral width is first broadened. An excellent successful example of this method is known as the spectral broadening induced by self-phase modulation in noble gases. The broadening efficiency of this technique is inversely proportional to the duration of the input pulse. During my M.Sc. thesis I have worked on spectral broadening induced by Raman response through molecular gases (N_2O). Our data signify a promising broadening efficiency which is maintained even at the 1000 fs regime.

Keywords: Ultrashort pulse characterization ; Frequency resolved optical switching (FROSt) ; Second harmonic generation microscopy ; Transition metal dichalcogenide (TMD) ; Second harmonic generation enhancement (SHG enhancement) ; Hollow core fiber (HCF) ; Spectral broadening induced by molecular gases ; Spectral broadening through Nitrous Oxide (N_2O)

RÉSUMÉ

Au cours de ma maîtrise à l'INRS, j'ai travaillé sur trois sujets : (1) le transfert de la technique FROSt (*Frequency Resolved Optical Switching*) pour caractériser des impulsions en microscopie, (2) l'utilisation d'impulsions laser ultra-brèves pour la caractérisation de matériaux en utilisant la microscopie optique de second harmonique et (3) le développement d'une nouvelle technique pour la compression d'impulsions laser.

La technique FROSt est basée sur une configuration pompe-sonde où la pompe crée une porte transitoire et la sonde est constituée des impulsions à caractériser. La porte transitoire est établie en utilisant une pompe pour induire un changement dans la transmissivité d'un matériau par photoexcitation des électrons de la bande de valence à la bande de conduction. Ainsi, la principale exigence pour utiliser le FROSt est d'avoir une intensité de pompe suffisante pour photoexciter le matériau. Au cours de ma maîtrise, j'ai travaillé à la mise en œuvre de cette technique pour la caractérisation temporelle d'un oscillateur laser Titane-Saphir ultrarapide utilisé dans notre laboratoire de microscopie non-linéaire. L'objectif était de pouvoir mesurer le profil temporel des impulsions lasers au foyer d'un objectif de microscope à grande ouverture numérique. Même si nous n'avons pas encore atteint cet objectif, nous savons ce qu'il faut faire à l'avenir pour implémenter le FROSt pour cette application.

Travailler sur la mise en œuvre du FROSt pour le laboratoire de microscopie m'a encouragé à me familiariser avec le monde de la microscopie non-linéaire. La génération de second harmonique (SHG) est un effet non-linéaire de second ordre, qui ne se produit que lorsque la symétrie d'inversion du milieu est rompue. L'implémentation de ce concept dans un système de microscopie permet de créer une technique de mesure puissante capable d'analyser les propriétés de symétrie. Les dichalcogénures de métaux de transition (TMD) appartiennent à une grande partie de la famille des matériaux bidimensionnels (2DM) dans laquelle la symétrie d'inversion du milieu est régie par le nombre de couches. L'altération des effets de charge des excitons dans cette famille conduit à l'accordabilité de l'émission de SHG de ce milieu. Ce concept a été démontré en utilisant le dopage électrostatique et pendant ma maîtrise, j'ai travaillé sur la possibilité d'obtenir le même résultat en manipulant l'architecture moléculaire (empilage d'une couche moléculaire continue 2D en un bloc de construction bidimensionnel pour manipuler les propriétés). Nous avons démontré ce concept à petite échelle.

Un nombre important d'applications comme la génération d'harmoniques d'ordre élevé (HHG) nécessite des impulsions d'énergie élevée pour atteindre des puissances crêtes très élevées. Principalement, la puissance crête de l'impulsion est inversement proportionnelle à la durée de l'impulsion et donc la post-compression temporelle non-linéaire joue un rôle important. Le produit de la durée de l'impulsion par la largeur spectrale est connu sous le nom de produit temps-fréquence et régit les limites des durées d'impulsions. Dans la compression non-linéaire d'impulsions, pour étendre la compression temporelle des impulsions, le spectre est d'abord élargi. Un excellent exemple de réussite de cette méthode est connu sous le nom d'élargissement spectral induit par l'automodulation de phase dans les gaz nobles. L'efficacité de l'élargissement obtenu avec cette technique est inversement proportionnelle à la durée de l'impulsion d'entrée. Au cours de ma maîtrise, j'ai travaillé sur l'élargissement spectral induit par la réponse moléculaire dans les gaz moléculaires (N_2O). Nos données indiquent une efficacité d'élargissement prometteuse qui est maintenue même dans les échelles de 1000 fs.

Mots clés: impulsions ultra-brèves caractérisation ; FROSt ; la microscopie de second harmonique ; dichalcogénures de métaux de transition (TMD) ; amélioration de la SHG ; de fibres à cœur creux (HCF) ; compression d'impulsions et élargissement spectral basés sur la réponse moléculaire Raman

SYNOPSIS

Pendant ma maîtrise sous la direction du Prof. François Légaré, j'ai travaillé sur trois sujets liés à la génération, la caractérisation et les applications des impulsions lasers ultra-brèves. Avant ma maîtrise, j'avais une expérience très limitée en optique et les trois projets auxquels j'ai participé au cours des deux dernières années et demie m'ont permis d'acquérir de l'expérience en optique non-linéaire. Plus précisément, les trois sujets sur lesquels j'ai travaillé sont les suivants: (i) la caractérisation temporelle des impulsions lasers au foyer d'un objectif de microscope en utilisant la technique FROSt (*Frequency Resolved Optical Switching*), (ii) la microscopie de second harmonique pour la caractérisation de matériaux, et (iii) l'élargissement spectral des impulsions lasers femtosecondes en utilisant la réponse moléculaire Raman rotationnelle. Nous passerons ici en revue brièvement chacun des projets.

(i) Caractérisation d'impulsions à l'aide de la technique FROSt

Le développement des lasers à verrouillage de mode au milieu des années 60 [1] a donné naissance au problème de la mesure des impulsions ultra-brèves, car les impulsions optiques générées par cette classe de lasers étaient d'une durée nettement plus courte que le temps de réponse de tout photodétecteur [2]. L'autocorrélation en intensité basée sur la génération de second harmonique a été la première approche fructueuse pour caractériser la durée des impulsions ultra-brèves sans avoir besoin d'impulsions de référence connues [3]. Cette technique est basée sur la mesure de l'impulsion ultra-brève par elle-même en utilisant un processus non-linéaire tel que la génération de second harmonique [4]. Cependant, cette technique ne fournit qu'une estimation de la durée de l'impulsion puisque différentes structures temporelles d'impulsion peuvent donner le même résultat d'autocorrélation par SHG. Par ailleurs, il n'est pas toujours suffisant de connaître uniquement la durée de l'impulsion. Par exemple, la structure de l'impulsion peut jouer un rôle important dans la compréhension du résultat d'une expérience telle que l'étude des vibrations moléculaires [5]. Pour mesurer la structure temporelle exacte d'une impulsion laser, il faut connaître son amplitude et sa phase spectrales. Cependant, la caractérisation de la phase d'impulsions inconnues est demeurée un défi jusqu'en 1991. Ce problème a finalement été résolu par l'introduction de la technique FROG (*Frequency Resolved Optical Gating*) [6].

La technique FROG permet de déterminer l'évolution de l'intensité et de la phase d'une impulsion ultra-brève arbitraire, en un seul tir ou plusieurs tirs. L'appareil expérimental est simple (Figure 1) et peut être assemblé en une journée une fois que les composants sont disponibles. La technique FROG peut utiliser pratiquement tout phénomène optique non-linéaire à réponse presque instantanée, comme la génération de second harmonique (SHG) par exemple. La SHG est une conversion instantanée de deux photons en un

photon à une fréquence exactement le double de celle du faisceau incident [7]. De plus, la SHG est un processus paramétrique où l'énergie des photons doit toujours être conservée (Eq.4). En plus de l'énergie des photons, la quantité de mouvement des photons (Eq.5) doit également être conservée. En d'autres termes, pour que ce processus se déroule efficacement, la condition d'accord de phase (Eq.6) doit être satisfaite [8].

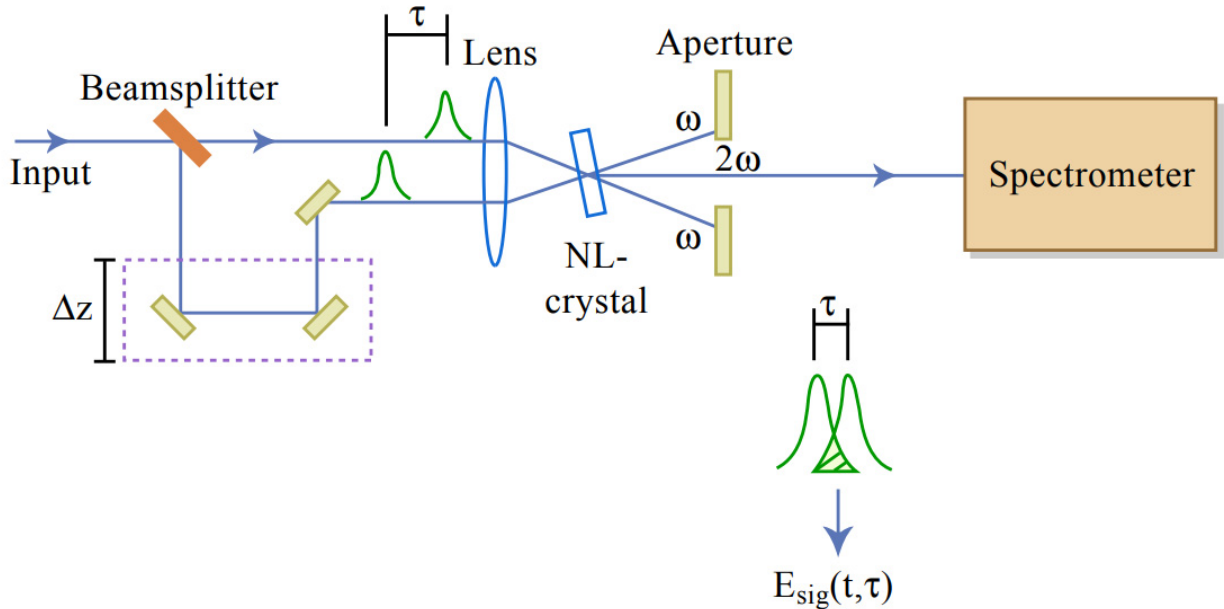


Figure 1: Montage d'un FROG basé sur la génération de second harmonique. La génération d'harmonique non-linéaire agit comme une porte optique.

Grâce aux progrès des technologies laser ultrarapides et de l'optique non-linéaire, les impulsions ultra-brèves de l'UV à l'infrarouge moyen sont largement accessibles. Les impulsions sur une large gamme spectrale sont souvent combinées simultanément dans des expériences pompe-sonde. La caractérisation d'une telle variété d'impulsions nécessite différentes techniques de métrologie, en fonction de leurs spécifications (c'est-à-dire l'énergie, la longueur d'onde centrale et la largeur de bande). En outre, les technologies de pointe permettent de générer des impulsions dont le spectre dépasse une octave, ce qui est encore plus difficile à caractériser avec les approches classiques.

Les approches basées sur la conversion de fréquence se sont avérées fiables dans la reconstruction des impulsions. Cependant, l'interaction paramétrique non-linéaire sous-jacente nécessite de remplir la condition d'accord de phase. Dans le cas des techniques basées sur la conversion de fréquence, telles que le SHG FROG, c'est le facteur limitant pour la largeur de bande d'impulsion pouvant être mesurée. Par exemple, la mesure d'impulsions à $0,8 \mu\text{m}$ d'une durée de quelques cycles avec le SHG FROG requiert un cristal de bêta-borate de baryum (BBO) d'une épaisseur de quelques μm seulement. Pour contourner cette difficulté, la condition d'accord de phase peut être grandement assouplie en utilisant des non-linéarités de

troisième ordre telles que le FROG basé sur un réseau transitoire et le FROG basé sur un changement de polarisation.

La technique alternative de caractérisation d'impulsions appelée FROSt (*Frequency Resolved Optical Switching*) est une technique nouvellement développée au laboratoire ALLS (*Advanced Laser Light Source*) basée sur l'absorption transitoire dans les solides. L'impulsion à caractériser sonde la commutation ultra-rapide de la transmission optique transitoire d'un solide, déclenchée par une impulsion pompe. La commutation provient de la dynamique des porteurs de charge photoexcités et agit comme une lame temporelle, tranchant l'onde de l'impulsion sonde dont le spectre transmis est ensuite enregistré en fonction du délai entre la pompe et la sonde. À partir du spectrogramme obtenu, nous extrayons le profil temporel de l'impulsion sonde et du commutateur à l'aide d'algorithmes ptychographiques. Cette approche ne repose pas sur une conversion non-linéaire de fréquence, et n'est donc pas limitée par la contrainte d'accord de phase ni par l'intensité de l'impulsion. Cette méthode est un outil puissant pour caractériser la sortie d'un système d'amplification paramétrique optique (OPA) puisque la sortie d'un OPA est une impulsion de longueur d'onde variable, généralement d'énergie suffisante (μJ) pour induire le processus de photoexcitation requis.

Comme mentionné précédemment, l'approche du FROSt est basée sur la photoexcitation d'un solide par une forte pompe et le contrôle de l'altération du spectre de la sonde induite par le solide photoexcité. La preuve de concept de cette technique a été réalisée en utilisant des impulsions de l'ordre des μJ d'un système laser avec un taux de répétition de 100 Hz. En résumé, nous ne disposons pas de l'information complète sur les limites de cette technique : par exemple, nous pensons que le temps de relaxation du matériau solide (après photoexcitation) peut limiter l'utilisation de cette technique avec des sources lasers à taux de répétition élevé. Comme les systèmes d'oscillateurs à haut taux de répétition sont très utilisés dans le monde de l'optique (en particulier en microscopie non-linéaire), une étude a été menée ici pour en savoir plus sur les limitations du FROSt pour caractériser leur sortie.

L'approche optique exploitée par cette technique est aussi simple que pour le SHG FROG non-colinéaire. Pour débiter l'expérience, le chevauchement temporel dans le montage est d'abord vérifié en utilisant la SHG dans un cristal de BBO. Ensuite, il suffit de passer directement à notre solide (ZnSe) et de mesurer la transmission de la sonde avant et après le chevauchement temporel avec la pompe : nous recherchons une porte transitoire (Figure 2.18) qui est utilisée pour reconstruire l'impulsion en fonction de la position de la ligne de retard pour le seuil de chute de transmission à chaque longueur d'onde du spectre de la sonde.

La chute de transmission pour les portes mesurées était toujours d'environ 0,86 %, ce qui est nettement inférieur à la chute de 98 % à la Figure 2.16 (pour une source de puissance crête élevée). Il convient de mentionner que, puisque cette chute de transmission est extrêmement faible (proche du niveau de bruit du laser et du sélecteur d'impulsion), pour observer cette porte, j'ai dû trouver un moyen de stabiliser

énormément le laser et le sélecteur d'impulsion. Le seuil de chute de transmission requis actuellement pour réussir à reconstruire l'impulsion en utilisant l'algorithme FROSt est de 10 %. Ainsi, bien que nous ayons trouvé notre porte ici, nous ne pouvons pas reconstruire l'impulsion puisque la chute de transmission n'est pas suffisante pour l'algorithme. Selon nos calculs, pour avoir une chute de transmission suffisante en utilisant une pompe à 800 nm avec des impulsions de 15 nJ, nous devons avoir un faisceau de diamètre au focus d'au moins 3,45 μm . Il est possible d'atteindre la taille de tache focale souhaitée à l'aide d'un objectif de microscope.

(ii) Étude de l'accordabilité de la SHG grâce à l'architecture moléculaire

Lorsque nous réfléchissons aux propriétés d'un matériau, nous pensons souvent qu'elles sont basées uniquement sur ce dont le matériau est constitué. Le métal conduit l'électricité parce que ses atomes sont maintenus ensemble par des liaisons métalliques - qui laissent les électrons libérer à travers le matériau lorsqu'un champ électrique est appliqué. Le béton est solide parce qu'il contient du ciment qui emprisonne de manière rigide des morceaux incompressibles de sable et de gravier. Le caoutchouc vulcanisé est souple, mais quand même durable, car il est constitué de chaînes de polymères souples qui sont fermement liées entre elles. Cependant, il y a autre chose qui peut affecter le comportement d'un matériau : sa taille. Cela est particulièrement vrai pour certains matériaux lorsque leurs dimensions sont réduites à l'échelle nanométrique (c'est-à-dire que leur taille peut raisonnablement être exprimée en nanomètres - généralement inférieure à quelques centaines de nanomètres, jusqu'à moins d'un nanomètre). La conductivité électrique, la réactivité chimique, les propriétés mécaniques et même la manière dont un matériau interagit avec la lumière peuvent toutes changer à l'échelle nanométrique.

Les matériaux bidimensionnels (2DM) font référence à une famille de matériaux très intéressante qui ne comportent qu'une ou quelques couches d'atomes [9]. Le membre le plus connu de cette famille, le graphène, a été découvert en 2004 [10] et depuis lors, ce type de matériau a été largement étudié [11–15]. Dans cette famille, dans les plans liés de manière covalente, les réseaux cristallins d'atomes sont assemblés par des interactions de van der Waals (vdW) hors-plan entre les couches. Le ditellure de molybdène (MoTe_2), le disulfure de molybdène (MoS_2) et le diséléniure de tungstène (WSe_2) appartiennent aux dichalcogénures de métaux de transition (TMD) qui constituent un grand groupe de la famille des 2DM [16]. Les dichalcogénures de métaux de transition suivent la formule générale MX_2 , où M représente l'atome de métal de transition (molybdène ou tungstène) et X représente un atome de chalcogène (tellure, soufre ou sélénium) [17]. Les TMD couvrent tout le spectre de la conductivité électrique (de l'isolant et des semi-conducteurs aux métaux) [18], ce qui permet de fabriquer des transistors ultra-minces de faible puissance [19]. Les membres de cette famille sont composés de trois plans atomiques et leur réseau hexagonal présente une

symétrie d'ordre 3 qui peut supporter la symétrie d'inversion. Les TMD ont des transitions inter-bandes qui suivent la règle de sélection résultant de la rupture de la symétrie d'inversion.

En fonction du nombre de couches pair ou impair dans les TMD (Figure 3.13), la symétrie d'inversion de ces matériaux peut être rompue, ce qui donne la possibilité de générer un signal de second harmonique à partir de ceux-ci. De façon plus détaillée, dans les TMD (avec une phase hexagonale - 2H), la symétrie d'inversion est rompue dans les structures avec un nombre impair de couches, ce qui entraîne un signal de SHG important dans les structures avec des couches impaires. En revanche, le signal de SHG est négligeable dans les structures avec des couches paires puisque la symétrie d'inversion n'est pas rompue [16,20–22]. Cependant, la tendance mentionnée est inverse pour les TMD de forme 1T' (phase monoclinique) [23]. Il est à noter qu'un signal de SHG négligeable peut être mesuré lorsque la symétrie d'inversion n'est pas rompue, ce qui est causé par les effets de surface du matériau [17].

L'idée d'utiliser des solides de la famille des 2DM comme blocs de construction pour assembler verticalement des structures empilées (connues sous le nom d'hétérostructures de van der Waals (vdWH)) est très étudiée dans la communauté scientifique [24–31]. En bref, des couches individuelles de 2DM sont combinées pour former un bloc de plans qui peut être manipulé et superposé à d'autres [32,33]. Cela permet d'obtenir des structures plus complexes, car les propriétés finales des vdWH sont très différentes de celles des 2DM isolés. Entre autres, on retrouve de grands changements dans les propriétés électroniques [34–37], optiques [38,39] et magnétiques [40–42]. Toutefois, les matériaux de type 2DM ne sont estimés qu'à quelques centaines [43]. Cependant, l'ajout de molécules (une couche moléculaire 2D continue) à un bloc de la famille des 2DM élargirait considérablement la gamme des propriétés potentielles de cette famille. Il existe un nombre illimité de degrés de liberté (figure 3.17) dans le design et la synthèse moléculaire [44–46] qui peuvent modifier les propriétés du bloc. Ce concept permet à l'architecture artificielle des matériaux 2D d'activer des propriétés atomiques/moléculaires spécifiques, et les propriétés finales des blocs peuvent être sélectionnées par un design moléculaire minutieux. Enfin, l'intégration d'une monocouche moléculaire cristalline dans une hétérostructure de van der Waals (vdWH) multicouche forme un nouveau type d'assemblage connu sous le nom de vdWH hybride [47–54].

Cette expérience a été conçue pour évaluer la possibilité d'utiliser des couches moléculaires pour contrôler la génération de second harmonique dans les TMD. Pour en évaluer l'ampleur, l'émission de SHG de quelques TMD a été comparée avec et sans la couche moléculaire supplémentaire. Au cours de cette étude, les échantillons sans couche moléculaire supplémentaire (couche moléculaire continue en 2D) sont appelés les échantillons originaux (TMD) et l'échantillon avec les couches moléculaires supplémentaires est appelé le TMD hybride (ou TMD à architecture moléculaire). Pour ce faire, le disulfure de molybdène (MoS_2) et le diséléniure de tungstène (WSe_2) ont remplacé le ditellure de molybdène (MoTe_2) original. La Figure

3.22 représente le dispositif utilisé comme référence dans notre expérience. Ce dispositif est une hétérostructure entièrement inorganique où un dispositif de type p (WSe_2) est combiné à un dispositif de type n (MoS_2) [38].

Les effets du dopage moléculaire sur un dispositif de type n et sur un dispositif de type p devraient être opposés. En d'autres termes, nous pensons que notre dispositif hybride présentera une amélioration de la SHG dans le WSe_2 et une diminution de la SHG dans le MoS_2 . Fondamentalement, notre étude permet de suivre simultanément l'effet opposé de la couche moléculaire continue 2D prévu dans le WSe_2 et le MoS_2 . En fin de compte, nous avons démontré (Figure 3.23, Figure 3.24) la possibilité de contrôler la SHG, à une petite échelle, grâce à l'architecture moléculaire de la surface des TMD.

(iii) Compression d'impulsions et élargissement spectral basés sur la réponse moléculaire Raman

Il existe de nombreuses sources de lumière dans le monde, mais l'amplification de la lumière par émission stimulée de radiation, communément appelée laser, est la source la plus utilisée par les scientifiques car elle peut fournir un rayonnement amplifié répétitif à des échelles de temps très brèves (nano/pico/femto/attosecondes). Plus précisément, les sources de lumière peuvent être divisées en sources cohérentes et sources incohérentes. La catégorie des sources cohérentes comprend les diodes laser, les modules de diodes laser, les lasers accordables, les lasers HeNe et les lasers femtosecondes, tandis que la catégorie des sources incohérentes comprend plutôt une variété de DEL, la lumière blanche et les sources SLD à large bande.

Un oscillateur laser simple (Figure 4.1) est composé d'un milieu de gain laser, d'une source de pompage et d'une cavité optique [55]. À l'intérieur de la cavité optique, la lumière est piégée pour être amplifiée en passant à travers le matériau du milieu de gain à répétition (confinée dans un résonateur). Le tout est conçu de manière à ce qu'une partie de la lumière puisse être extraite sous forme de faisceau lumineux afin de fonctionner comme un oscillateur [56]. Dans des conditions normales, il y a toujours plus d'atomes au niveau d'énergie le plus bas par rapport au niveau d'énergie excité du milieu de gain. Cependant, pour que l'amplification fonctionne correctement, le milieu de gain doit être maintenu dans un état d'inversion de population (le nombre d'atomes au niveau d'énergie supérieur doit être plus élevé que celui du niveau d'énergie inférieur). Cette condition est maintenue dans un oscillateur laser grâce au mécanisme de pompage [57].

L'autofocalisation a posé un défi pour l'amélioration de la puissance de sortie des lasers pendant près de deux décennies (Figure 1.1). Cette question a finalement été contournée par l'introduction de l'amplification par dérive de fréquence (*chirped pulse amplification* ou CPA) en 1985 [58]. Avant la CPA, les systèmes

laser devaient demeurer bien en deçà du seuil d'intensité d'autofocalisation (GW/cm^2) pour éviter d'endommager les optiques du système [59,60]. Le concept à la base de la technique CPA est l'abaissement de l'intensité optique pendant l'étape d'amplification. Ce principe est illustré à la Figure 4.2.

Des développements importants ont été réalisés au cours des six dernières décennies pour générer des impulsions lasers intenses ultra-brèves [61–65]. Parallèlement au développement des sources lasers énergétiques, des techniques de post-compression ont été développées pour générer des impulsions à cycle unique [66]. Afin de bénéficier de l'intensité crête maximale possible, les développements de la post-compression ont été cruciaux puisque la puissance crête de l'impulsion est inversement proportionnelle à la durée de l'impulsion [67].

En principe, le produit temps-fréquence (*time-bandwidth product* ou TBP) d'une impulsion est toujours supérieur au minimum théorique [63,68,69]. Lorsqu'une impulsion a la durée minimale possible, on dit qu'elle est à la limite de Fourier. Elle est également décrite comme une impulsion à phase spectrale plate [4]. Ce phénomène est à la base des techniques de post-compression non-linéaire, qui nécessitent d'abord d'augmenter la largeur de bande spectrale des impulsions. Généralement, cela se produit en exploitant un phénomène non-linéaire comme l'automodulation de phase pour élargir spectralement l'impulsion avant la compression.

L'automodulation de phase fait référence au phénomène par lequel un faisceau laser se propageant dans un milieu interagit avec ce milieu et s'impose une modulation de phase à lui-même. L'origine physique du phénomène réside dans le fait que le champ puissant d'un faisceau laser est capable d'induire un changement appréciable de l'indice de réfraction du milieu en fonction de l'intensité. Le milieu réagit alors et inflige un changement de phase à l'onde entrante, ce qui entraîne l'automodulation de phase (SPM). Dans le cas où l'onde d'entrée provient d'un laser pulsé, la variation temporelle de l'intensité du laser entraîne une SPM dans le temps. Comme la dérivée temporelle de la phase d'une onde est simplement la fréquence angulaire de l'onde, la SPM apparaît également comme une modulation de fréquence. Ainsi, le faisceau de sortie apparaît avec un élargissement spectral auto-induit.

En 1981, une nouvelle méthode de compression d'impulsions a été introduite, consistant en la propagation de la lumière à travers une fibre monomode pour introduire un élargissement spectral à la fois par l'automodulation de phase et par un retard de groupe. Comme la largeur de bande spectrale est plus grande, la compression avec un miroir chirpé nous permet d'obtenir une impulsion relativement plus courte que l'impulsion initiale. Les fibres monomodes sont limitées à la gamme d'énergie des nJ, qui peut être qualifiée de faible énergie. Cette limitation est due à l'apparition de non-linéarités d'ordre élevé. En 1996, avec l'introduction d'une nouvelle technique basée sur l'utilisation de fibres à cœur creux (*hollow core fibers* ou

HCF) et de gaz nobles, ce problème a été surmonté permettant la compression d'impulsions à des énergies mJ.

En général, la compression d'impulsions via la SPM est limitée par un facteur de compression [70]. Par exemple, une fibre de 6 mètres est nécessaire pour compresser d'un ordre 33 des impulsions de 170 fs [71]. En utilisant plutôt la réponse moléculaire, nous pouvons atteindre un facteur de compression plus élevé tout en ayant une configuration plus compacte.

Ici, nous discuterons de l'élargissement spectral induit par la réponse moléculaire de l'azote (N_2) et de l'oxyde nitreux (N_2O). Les gaz nobles sont des milieux inactifs en Raman, et la plupart des techniques proposées pour l'élargissement spectral et la compression d'impulsions dans les HCF ont été axées sur eux. En somme, les gaz moléculaires ou plus spécifiquement les gaz actifs en Raman ont été initialement négligés car ils ont une réponse non-linéaire retardée liée à l'excitation de modes rotationnels ou vibrationnels [72]. L'objectif de cette étude est de comprendre le comportement et le potentiel des gaz moléculaires ayant une forte réponse Raman pour l'élargissement spectral. Ce projet peut avoir des applications pour la génération de supercontinuum [73], la compression temporelle d'impulsions et pour repousser le *cutoff* de la génération d'harmoniques d'ordre élevé [74].

L'interaction du fort champ électrique d'un laser avec des gaz moléculaires crée des paquets d'ondes. Cette interaction induit un moment de force important dans les molécules qui entraîne un mouvement vibrationnel et un alignement rotationnel [75]. Ces événements dépendent de la relation entre la durée de l'impulsion incidente et le mouvement moléculaire. Par exemple, les molécules continueront à tourner même après l'interaction si l'impulsion est plus courte que le mouvement moléculaire [76].

Lorsque la durée de l'impulsion incidente est comparable à l'échelle de temps du mouvement moléculaire (régime d'excitation via l'impulsion), un mouvement appelé "kick rotor" se produit, qui préserve la quantité de mouvement donnée par le laser après le passage de l'impulsion [77,78]. En d'autres termes, des paquets d'ondes sont créés en accord avec le mouvement rotationnel cohérent des molécules. L'élargissement spectral établi grâce à la réponse rotationnelle et le gain Raman est décrit comme la fonction de réponse moléculaire retardée $R(\tau)$ par rapport à l'impulsion d'entrée.

La convolution (Eq.28) présente une montée abrupte à la tête et une chute lente à la queue. Il en résulte la génération d'une nouvelle fréquence en tête de $\Delta n(t)$ qui crée un spectre asymétrique. Le chevauchement de l'enveloppe de l'impulsion avec la queue et la tête de $\Delta n(t)$ déterminera le degré d'asymétrie. L'efficacité de l'élargissement spectral par alignement moléculaire est maximisée lorsque la durée de l'impulsion se situe à l'échelle de temps de l'alignement rotationnel maximal [79].

L'aspect pratique de l'élargissement spectral et de la compression d'impulsions à l'aide de gaz moléculaires (réponse rotationnelle et gain Raman) a été démontré à l'aide de miroirs chirpés post-compression. Ici, la sortie de la HCF avec une impulsion d'entrée de 120 fs a été compressée avec des miroirs chirpés. Comme chaque réflexion des miroirs chirpés introduit une quantité spécifique de chirp, du verre de quartz a également été utilisée pour le réglage fin. Au total, une dispersion de retard de groupe négative de 176 fs² a été introduite dans l'impulsion, et l'impulsion principale avec 50 % de l'énergie initiale a été compressée à 7,8 fs (limite de Fourier ~ 6,2 fs).

Nous poursuivons notre étude de l'élargissement spectral induit par réponse moléculaire (N₂ section 4.2) en utilisant le N₂O. Ce milieu gazeux a été choisi, car il présente une non-linéarité relativement importante par rapport au N₂ : nous prévoyons un élargissement plus important en raison de la non-linéarité plus grande de cette molécule. En outre, l'alignement rotationnel maximal de N₂ se produit à environ 120 fs. Cependant, le N₂O est un gaz plus lent, et nous nous attendons à un alignement rotationnel maximal à environ 280 fs [80].

Le comportement global de cette technique est compliqué et nécessite une étude plus approfondie. En se basant sur les simulations 1D et sur la théorie, nos attentes initiales nous portaient à croire que l'efficacité de l'élargissement serait maximale à l'échelle temporelle de la réponse moléculaire. Ainsi, nous nous attendions à ce que l'alignement maximal se produise autour de 280 fs (N₂O). Cependant, nos données à la Figure 4.12 ne confirment pas cette hypothèse. La tendance générale de la Figure 4.12 semble indiquer qu'il existe une relation inverse entre la durée d'impulsion et la puissance crête requise pour saturer l'efficacité de l'élargissement. Néanmoins, nos mesures à haute pression sont en accord avec le fait que l'efficacité maximale de l'élargissement serait à l'échelle temporelle de l'alignement moléculaire. En résumé, lorsque nous ne sommes pas limités à la puissance crête d'entrée ou à la pression du système, l'efficacité d'élargissement maximale suit le comportement attendu. Cependant, l'efficacité de l'élargissement pour différentes durées d'impulsions d'entrée est extrêmement sensible à la puissance crête d'entrée. Les impulsions de plus courte durée nécessitent une puissance crête ou une pression moléculaire plus élevée pour atteindre l'élargissement maximal possible.

TABLE OF CONTENTS

DEDICATION	III
ACKNOWLEDGEMENTS	V
FORWARD CREDITS	VII
ABSTRACT	IX
RÉSUMÉ.....	XI
SYNOPSIS.....	XIII
TABLE OF CONTENTS	XXIII
LIST OF FIGURES.....	XXV
LIST OF ABBREVIATIONS AND SYMBOLS.....	XXIX
Chapter 1 Introduction	1
1.1 Introduction to the study	2
1.2 Organization of the study	3
Chapter 2 Pulse characterization with Frequency Resolved Optical Switching.....	9
2.1 Preliminary information	11
2.1.1 Brief introduction on electromagnetic radiation	11
2.1.2 Brief introduction on second order nonlinear optical response and the impact of phase matching	13
2.1.3 Description of ultrashort laser pulses.....	16
2.2 The intensity autocorrelation.....	19
2.3 Frequency resolved optical gating (FROG)	21
2.4 Frequency resolved optical switching (FROSt)	23
2.5 Investigation of transient gate at different repetition rates	26
2.5.1 Future plan.....	32
Chapter 3 Second Harmonic Generation Microscopy	35
3.1 Brief introduction on microscopy.....	37
3.2 Nonlinear optical microscopy	39

3.3 SHG microscopy	40
3.4 Technical overview of our SHG Microscopy system.....	45
3.5 Illustration of using SHG microscopy to evaluate noncentrosymmetry.....	47
3.6 Molecular architecture to tune SHG from TMDs.....	50
3.6.1 Introduction.....	51
3.6.2 Controlling SHG through molecular architecture in TMDs.....	56
Chapter 4 Pulse compression and spectral broadening based on Raman molecular response	65
4.1 Pulse evolution through a fiber	68
4.2 Spectral broadening via molecular response	72
4.3 Spectral broadening via molecular response: beyond nitrogen	74
4.3.1 Influence of input pulse temporal duration at molecular gas spectral broadening.....	75
4.3.2 Influence of the input peak power on the molecular gas spectral broadening	79
Chapter 5 Conclusion.....	81
REFERENCES.....	85
APPENDIX.....	107

LIST OF FIGURES

Figure 1: Montage d'un FROG basé sur la génération de second harmonique. La génération d'harmonique non-linéaire agit comme une porte optique.	xiv
Figure 1.1: History of laser intensity [21].	3
Figure 2.1: Overview of the electromagnetic spectrum. Extracted from [73].	12
Figure 2.2: Quality of light waveform prospects. Adapted from [75].	12
Figure 2.3: Optical setup for the first experimental observation of SHG: Focusing a ruby laser beam on a quartz crystal, lead to appearance of relatively weak beam which is separated from the input beam by a prism. Extracted from [78].	13
Figure 2.4: Illustration of second-order nonlinear parametric processes including, (a): second harmonic generation (SHG), (b): sum frequency generation (SFG), (c): difference frequency generation (DFG). The schematic is represented in top and the transition energy diagram is represented in bottom.	14
Figure 2.5: (a): Refractive index is related to the frequency, thus the condition in Eq.7 cannot be satisfied. (b): Birefringent materials have ordinary and extraordinary refractive indices. Phase matching can be satisfied through using the extraordinary polarization for ω and ordinary for 2ω . Adapted from [83].	15
Figure 2.6: Simple illustration of the relationship between the pulse duration and the spectral width for (a-c): short-long pulse. Adapted from [83].	16
Figure 2.7: Ultrashort pulse filed representation. Extracted from [61].	17
Figure 2.8: The temporal shape of 800nm Gaussian laser pulse of (a): Flat phase, (b): First order phase - shifted in time, (c): Second order phase- broadened through 200 fs ² chirp. Adapted from [89].	19
Figure 2.9: Non-collinear autocorrelator setup: Two replicas of the pulse with an adjustable delay are spatially overlapped on a SHG crystal. Adapted from [89].	20
Figure 2.10: Gating the electric field temporally and then recording the spectrum of the gate in terms of the delay. $G(t-\tau)$ denotes the gate or window function (the overlap between $E(t)$ and $E(t-\tau)$). This allows simultaneous record of the arrival time and frequency of an optical wave. Extracted from [83].	21
Figure 2.11: SHG-FROG (a): Reconstructed spectrogram trace. (b): The intensity (black line) and phase (blue line) temporal evolution. Here we have a 52 fs pulse with third order phase behavior ($\phi_3=1465$ fs ³)	22
Figure 2.12: Principle of the frequency resolved optical switching. The initial spectrum of the probe is recorded in terms of the time delay. Extracted from [26].	23
Figure 2.13: Transient absorption processes. This absorption will act as a semiconductor switch.	23
Figure 2.14: The FROSt spectrogram of the 7 μ m MID IR source. The silicon medium was photoexcited by the 800 nm pump.	25
Figure 2.15: The intensity and phase temporal evolution of the pulse. The temporal duration of the pulse is 153 fs (Second order phase: -192 fs ² , Third order phase: -7621 fs ³). The FROSt reconstruction was performed by Philippe Lassonde.	25
Figure 2.16: The arrival of the 800 nm pump will induce a gradual drop on the 7 μ m transmission of the probe.	26
Figure 2.17: Initial experimental setup to investigate FROSt operation at different repetition rates	26
Figure 2.18: Transient gate which creates a gate for the probe and the reconstruction occurs based on the location of each frequency cut-off.	27
Figure 2.19 Inside the Tsunami Oscillator. Modification intended for exploiting the maximum energy.	28
Figure 2.20: Probe output spectrogram at 400 kHz repetition rate.	29

Figure 2.21: Using chirped mirrors to compress the input pulse from (a): 470 fs, $\phi_2=9.76 \times 10^3$ fs ² to (b): 66 fs, $\phi_2=16$ fs ² . (left): Reconstructed spectrogram. (right): Pulse intensity and phase vs. delay.....	31
Figure 2.22: Transmission of ZnSe using a microscope objective. The X axis provides the relative position of the sample from the focal spot. This plot provides the sensitivity of the focal spot for inducing a 54% transmission drop.	32
Figure 2.23: Recommended setup.....	33
Figure 3.1: SHG and fluorescence spectra in comparison to the fundamental spectra. Changing the fundamental wavelength directly changes the SHG position ($\lambda_{\text{SHG}}=0.5 \lambda_{\text{Fundamental}}$), though the broad spectrum of fluorescence remains unchanged and is only affected in magnitude. Adapted from [103]......	36
Figure 3.2: (a): The first compound microscope made by Janssen (1590's). (b): Hook's compound microscope (1665) used for discovery of cell. Adapted from [108].	37
Figure 3.3: Significant early development of optical microscope thought the years [104,110–113]......	38
Figure 3.4: The transition energy diagram of (a): SHG and (b) 2PEF. SHG photon is emitted through a virtual transition at exactly double the incident photon energy. However, in a 2PEF a photon is emitted through real electron energy transition and always has less energy than double the incident photon energy.....	39
Figure 3.5: The calibration map prepared for P-SHG scan. A fully eight-shaped fit represents a linear polarization and an oval (circular) fit represents a circular polarization point.	42
Figure 3.6:(a): Typical wave-vector mismatch in SHG. (b): Perfect phase matching in SHG. Adapted from [114]...	43
Figure 3.7: (a) Fluorescence has isotropic emission. However (b) SHG directionality is based on the orientation and distribution of the nonlinear dipoles. Extracted from [97]. (c): The SHG and THG radiation patterns in tightly focus microscopy. Extracted from [166]. Backward generation is not shown to simplify the understanding.	44
Figure 3.8: SHG microscopy image of MoSe ₂ in forward (transmission) and backward (reflection) directions. The SH signal dominates in the forward direction, though backward generation is a real asset, especially when there are limitations in forward detection. Sample was provided by Franz J. F. Löchner, Institute of Applied Physics, Abbe Center of Photonics, Friedrich Schiller University Jena.	45
Figure 3.9: Multiphoton Microscope Setup	45
Figure 3.10: A 2000×2000um SHG microscopy image of SrTiO ₃ nanoislands.	48
Figure 3.11: SH signal of SrTiO ₃ vs. the fundamental power at fixed polarization.	49
Figure 3.12: SH signal of SrTiO ₃ vs. the fundamental polarization.	50
Figure 3.13: The SH intensity of TMDs is highly dependent on the number of layers. The SH image of the following TMDs is shown on the left and the SH intensity as a function of the number of layers is shown on the right. (a): WS ₂ and (b): WSe ₂ taken from [205]. (c): MoS ₂ extracted from [206]. (d): MoTe ₂ extracted from [204]. The concept of figure is adapted from [194].....	52
Figure 3.14: (a): Gated monolayer WSe ₂ (TMD) to tune the SH signal. (b): SHG spectra on resonance with the exciton at selected gate voltages. The tunability origins can be understood by the formation of positive and negative trions at high carrier density. Extracted from [45].	53
Figure 3.15: (a): Gated monolayer of MoTe ₂ combined with a drop of ionic liquid which is capable of manipulating electron population and inducing a phase transition. (b): SH intensity vs. gate voltage. The crystal structure of monolayer of MoTe ₂ is represented in (c) 2H phase. and (d) 1T' phase. (e): SHG microscopy image of 2H monolayer of MoTe ₂ at 0 V gate. (f): SHG microscopy image of the original 2H monolayer of MoTe ₂ at 4.1 V gate which induces a phase transition into 1T'. Adapted from [185].	54
Figure 3.16: The integration of molecular layers into 2DM building blocks widens the range of potential properties. Molecular layers associated with the freedom of (a): shape, (b): class of materials and (c): thickness. Extracted from [51].	55
Figure 3.17: The formed MoTe ₂ flakes using mechanically exfoliating. This figure was provided by Dr. Atiye Pezeshki using an optical microscope.	56

Figure 3.18: SHG image of a MoTe ₂ flake. The signal is extremely weak and close to noise level, even at the damage threshold of the sample. The small pink box presents the optical image of the same flake.	57
Figure 3.19: Using the reflection of the fundamental beam from silver coat to locate the single flake of interest in different rounds of measurements. The flake is located inside the smaller square.	58
Figure 3.20: SH signal of the MoTe ₂ original and hybrid flakes vs. the fundamental power at fixed polarization.	59
Figure 3.21: Optical image of the flake. (a): before, (b): after scan. The flake was damaged by the laser. This figure was provided by Dr. Atiye Pezeshki using an optical microscope.	59
Figure 3.22: Optical image of a p–n heterojunction used as the reference device for our study. The left triangle is a p-type Tungsten diselenide (WSe ₂) and the right triangle is a n-type Molybdenum disulphide (MoS ₂). The central lozenge is the overlay of WSe ₂ on MoS ₂ . This figure was provided by Dr. Atiye Pezeshki using an optical microscope.	60
Figure 3.23: Evaluation of SHG tunability using molecular architecture. Original TMDs are represented in blue. Control samples (no direct effect expected) are represented in red. Finally, the molecular architected TMDs are represented in purple. The molecular architected TMDs (purple) are expected to induce (a): SHG enhancement on WSe ₂ . (b): SHG diminution in MoS ₂ . However, the data doesn't agree with our expectation.	62
Figure 3.24: Evaluation of SHG tunability using molecular architecture (after purification of the Cl ₂ -A molecule). Original TMDs are represented in blue. Control samples (no direct effect expected) are represented in red. Finally, the molecular architected TMDs are represented in purple. The architected TMDs (purple) are expected to induce (a): SHG enhancement on WSe ₂ . (b): SHG diminution in MoS ₂ . The data agrees with our expectation.	63
Figure 4.1: Schematic of a laser oscillator. Extracted from [89].	66
Figure 4.2: The output of an oscillator is used as a seed to be stretched, amplified and then compressed. Extracted from [256].	67
Figure 4.3: SPM-broadened spectra for an unchipped Gaussian pulse. Spectra are labeled by the maximum ϕ_{NL}	70
Figure 4.4: Spectral broadening vs. pulse temporal duration at fixed peak power for (a): Kerr medium (Ar) and (b): delayed response medium (N ₂) at a fixed pressure of 1000 mbar.	73
Figure 4.5: SHG FROG pulse characterization (a): measured, (b): reconstructed, 120 fs input pulses were spectrally broadened in HCFs (N ₂ gas medium) and then temporally compressed (7.8fs) using chirped mirrors.	74
Figure 4.6: Gas-filled HCF spectral broadening experimental setup. The technical details are explained in appendix.	75
Figure 4.7: Spectral broadening over molecular pressure at 40 fs input pulse with 3GW peak power.	76
Figure 4.8: Gray area: Ultra-broad spectra measured at the output of HCF using 150 fs input pulses (2000 mbar). Dashed line: Spectra measured at vacuum condition. The delayed molecular response results in the generation of new frequencies at the leading edge of $\Delta n(t)$	76
Figure 4.9: Ultra-broad spectra measured at the HCF outlet using 280 fs input pulses (2000 mbar). In this regime, the spectrum is more symmetric since this pulse duration matches the time resolution of scale of the maximum rotational alignment of N ₂ O molecules.	77
Figure 4.10: Spectral broadening over molecular pressure at 280 fs input pulse with 3GW peak power.	77
Figure 4.11: (a): Broad spectra measured at the HCF outlet using 1000 fs input pulses (2000 mbar). The broadening is less efficient compared to Figure 4.9 and Figure 4.10 (280 fs). Though the method is still relatively efficient at increasing the bandwidth of input pulse. (b): Spectral broadening over molecular pressure at 1000 fs input pulse with 3GW peak power.	78
Figure 4.12: Spectral broadening by nitrous oxide at 200mbar for a variety of input peak powers.	80
Figure A: Grating position vs. pulse duration. Reference table to change the pulse duration.	108
Figure B: Reduction of the beam waist to ensure high O/I transmission inside the HCF.	109
Figure C: Evaluation of the gas contamination by spectral measurements made at different times for a pressure of 200 mbar.	110

Figure D: External contamination evaluation by scanning the broadening over period of time at 1000 mbar 110

Figure E: Calibration curves of the visible and NIR spectrometers. 111

Figure F: Spectral broadening over molecular pressure with 3 GW peak power. Input pulse duration (a): 40 fs, (b): 100 fs, (c): 150 fs, (d): 280 fs, (e): 350fs, (f): 500fs, (g): 1000fs. 114

Figure G: Spectral broadening over molecular pressure with 8 GW peak power. Input pulse duration (a): 100 fs, (b): 150 fs, (c): 280 fs. 115

Figure H: Output/Input HCF transmission of the experimental results presented in Figure F and Figure G. (a): 40 fs, (b): 100 fs, (c): 150 fs, (d): 280 fs, (e): 350fs, (f): 500fs, (g): 1000fs. 116

LIST OF ABBREVIATIONS AND SYMBOLS

Abbreviations

ALLS	Advanced Laser Light Source
c.c.	Complex Conjugate
CPA	Chirped Pulse Amplification
CARS	Coherent anti-Stokes Raman Scattering
DFG	Difference Frequency Generation
EMT	Energie Matériaux Télécommunications
eV	Electron Volt
FROG	Frequency Resolved Optical Gating
FROSt	Frequency Resolved Optical Switching
FWHM	Full-Width Half Maximum
GDD	Group Delay Dispersion
HCF	Hollow Core Fibers
INRS	Institut National de la Recherche Scientifique (French)
OR	Optical Rectification
OPO	Optical Parametric Oscillation
O/I	Output vs. Input
IM	Imaginary
Laser	Light Amplification by Stimulated Emission of Radiation
NA	Numerical Aperture
NL	Non-Linear
OPA	Optical Parametric Amplifier
SFG	Sum Frequency Generation
SH	Second Harmonic
SHG	Second Harmonic Generation
SPM	Self-Phase Modulation
TMD	Transition Metal Dichalcogenide
THG	Third Harmonic Generation
PMT	Photomultiplier Tube
vdW	Van Der Waals
2DM	Two-Dimensional Material
2PEF	Two-Photon Excited Fluorescence

Chemicals

Ar	Argon (Gas)
BaB ₂ O ₄	Barium borate (Crystal)
Cl ₂ -A	Chlorine Diatomic (Molecule)
DZM	3-deaza-3-methyladenine (Molecule)
N ₂	Nitrogen (Gas)
N ₂ O	Nitrous Oxide (Gas)
MoS ₂	Molybdenum Disulphide (2DM)
MoTe ₂	Molybdenum Ditelluride (2DM)
SrTiO ₃	Strontium Titanate (Thin film Crystal)
WSe ₂	Tungsten diselenide (2DM)
ZnSe	Zinc Selenide (Crystal)

Units

m	Meter
mm	Millimeter (10 ⁻³ Meter)
µm	Micrometer (10 ⁻⁶ Meter)
nm	Nanometer (10 ⁻⁹ Meter)
J	Joule
mJ	Millijoule (10 ⁻³ Joule)
µJ	Microjoule (10 ⁻⁶ Joule)
nj	Nanojoule (10 ⁻⁹ Joule)
kHz	Kilohertz (10 ³ Hertz)
MHz	Megahertz (10 ⁶ Hertz)
s	Second
ns	Nanosecond (10 ⁻⁹ Second)
ps	Picosecond (10 ⁻¹² Second)
fs	Femtosecond (10 ⁻¹⁵ Second)
W	Watt
mW	Milliwatt (10 ⁻³ Watt)
GW	Gigawatt (10 ⁹ Watt)
TW	Terrawatt (10 ¹² Watt)
PW	Petawatt (10 ¹⁵ Watt)

Notations

B	Magnetic Field
C	Contrast
c	Speed of Light
E	Electric Field
f	Frequency of Light
F_{rep}	Repetition Rate
I	Intensity
k	Wave Number
M	Magnification
n	Refractive Index
n_2	Nonlinear Refractive Index
P	Polarization
P_{avg}	Average Power
β	Hyperpolarizability
φ	Phase
λ	Wavelength
τ	Pulse Duration
ω	Angular Frequency
χ	Susceptibility
$\Delta\nu$	Frequency-Domain Width
Δt	Time-Domain Width
\propto	Proportional

Chapter 1

Introduction

1.1 Introduction to the study

In 1916, almost 42 years before the construction of the first laser, *Albert Einstein* introduced a physical amplification phenomenon called stimulated emission [1]. In this process, an incident optical signal of a suitable frequency causes an excited electron to lose its energy and returns to a lower level, which leads to emitted radiation. The first evidence of stimulated emission was indirectly reported in 1928 by *Rudolf Ladenburg* [2]. A decade later, he completed this work by proposing a direct method to demonstrate the existence of stimulation emission as well [3]. In 1953, *Charles H. Townes* and *James. P. Gordon* built the first ever maser (microwave amplification by stimulated emission of radiation) [4]. The introduction of this device initiated the idea of extending this principle to higher frequencies. Thus began the race to build the first ever laser (initially known as optical maser) [5]. Eventually the first ever laser (ruby crystal medium) was built by *H. Maiman* [6] in 1960 and this technology has been key in observing a wide variety of nonlinear optical effects including second harmonic generation (first observed by *Franken et al.* in 1961) [7]. Second harmonic generation (SHG), is nowadays used for a wide variety of applications including frequency conversion of laser wavelengths, pulse characterization [8,9] and laser scanning microscopy for material and biomedical imaging [10].

There are various number of applications (specially nonlinear effects) that rely on peak power, and they consequently confirm the necessity of pulsed lasers. Q-switching (also known as giant pulse formation) laser was one of the first steps on the path to achieve high peak power lasers. This idea was first proposed in 1958 by *Gordon Gould* [5] and then independently in 1962, *Fred J. McClung* and *Robert W. Hellwarth* [11] successfully generated 100 times higher peak power over the ordinary ruby lasers through a Kerr-cell switching technique. A typical, Q-switching laser can produce optical pulses in the order of 10 to 20 ns.

Mode locking is another successful approach to generate pulsed lasers. In this concept, the optical pulses can be as short as the Fourier transform of the bandwidth [12] and through the broad spectral bandwidth of dye lasers the path to ultrafast pulse generation began to accelerate. In 1972, *Erich Ippen* and *Charles Shank* reported the generation of 1.5 ps pulses by passive mode locking continuous wave (CW) dye lasers [13]. Dye lasers had important limitations and more importantly, maintenance of dye solutions were quite tricky and complex. This issue pushed the developers toward solid-state lasers. Although in 1987 pulses as short as 6 fs [14] were reported through the combine effect of pulse broadening and dispersion compensation, producing pulses below 100 fs was an extremely complicated and cumbersome task which limited this regime to a small number of laboratories [5]. The introduction of Ti-Sapphire lasers (1982, CW) combined with passive Kerr lens mode-locking (1990) revolutionized the ultrafast field by producing pulses as short

as 60 fs only through circulation inside the oscillator cavity [15]. In other words, Kerr lens mode locking paved the way for the generation of femtosecond pulses with high peak power directly from the laser cavity.

The introduction of chirped pulse amplification (CPA) technique was a major breakthrough (Figure 1.1) in laser science [16]. This technique resolved the pulse amplification limitation caused by a nonlinear phenomenon called self-focusing [17]. CPA was initially introduced in 1985 by *Prof. Gérard Mourou* and *Prof. Donna Strickland*. Their contribution was recognized by the 2018 physics Nobel Prize. The combination of mode locking Ti-Sapphire laser and CPA delivers an outstanding high-power pulse. With the help of gas-filled hollow core fibers [18], intense single-cycle pulses starting with a Ti-Sapphire laser system [19] has been generated. This approach is widely used in ultrafast laboratories for strong-field physics applications [20].

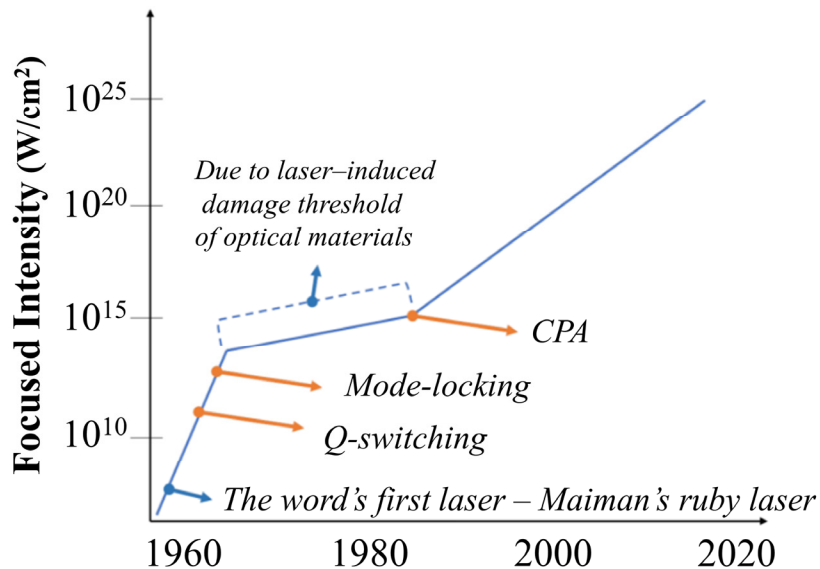


Figure 1.1: History of laser intensity [21].

1.2 Organization of the study

During my M.Sc. under the supervision of Prof. François Légaré, I worked on three topics related to the generation, characterization, and applications of ultrashort laser pulses. Prior to my M.Sc., I had very limited experience with optics and the three projects in which I have been involved over the last two and half years have helped me gain experience in nonlinear optics. More specifically, the three topics on which I have worked are: (i) temporal characterization of laser pulses at the focus of a microscope objective using Frequency Resolved Optical Switching (FROSt), (ii) second harmonic generation microscopy for material characterization, and (iii) spectral broadening of femtosecond laser pulses using the rotational Raman molecular response. Below, I will provide the scientific context motivating this research work.

For the development and applications of ultrafast laser systems, it is essential to have characterization techniques capable of measuring the temporal profile and spectral phase of the pulses [8]. For example, in SHG microscopy, the signal generated at the focus of the microscope scales inversely with the laser pulse duration [22]. In the group of Prof. François Légaré, we are using SHG microscopy for high spatial resolution imaging of biological samples and materials. However, we do not have a characterization technique capable of measuring the temporal profile of the laser pulses at the focus of the microscope objective. Indeed, through pulse temporal and phase characterization at the focus of the microscope, we can have better control of the nonlinear process in the microscope. In the context of my M.Sc. project, I have been working to expand the Frequency Resolved Optical Switching (FROSt) technique to temporally characterize laser pulses at the focus of our laser scanning microscope. This technique has been recently introduced by the group of Prof. François Légaré and is based on gating the pulses using transient absorption in a solid [23]. Contrary to current techniques based on Frequency Resolved Optical Gating (FROG) [24] and Spectral Phase Interferometry for Direct Electric-field Reconstruction (SPIDER) [25], FROSt is free of phase matching since it is not based on nonlinear optical conversion where phase matching has to be fulfilled [26]. For example, at the Advanced Laser Light Source (ALLS) laboratory, SHG-FROG is commonly used to characterize few-cycle laser pulses and satisfying the phase-matching condition imposes the use of very thin nonlinear optical crystals (e.g. 10 microns thick beta barium borate for measuring sub-10 femtosecond pulses at 800 nm) [27]. However, with FROSt, one needs to simply inject carriers in the conduction band of a low bandgap material with pump pulses and afterwards, to probe with the pulses to characterize the drop of transmissivity as a function of the time delay [26]. From the measured transmitted spectrogram (spectra vs. pump-probe delay), the pulses are retrieved using a ptychographic algorithm [28]. My goal was to apply this approach for the characterization of low energy pulses (few nanojoules) directly from a Ti:Sapphire oscillator used for SHG microscopy. Typically, the ultrafast light source for nonlinear microscopy is a high repetition rate (MHz range) near-infrared laser. This source induces a high number of generated photons while maintaining a low amount of energy per pulse to avoid ionization and damage in the imaged material. This was actually the main reason to further investigate the possibility of characterizing low energy pulses using the FROSt technique. While we have obtained some spectrograms showing a transient gate induced by the pump pulses, we have not been able to reach sufficient intensity to observe a permanent drop of transmissivity as it was observed in ALLS [26]. For this reason, we have not been able to obtain the temporal profile of the low energy pulses with FROSt. However, as discussed in greater details in section 2.5, the optical configuration that we have used so far was not focusing the pump pulses enough to reach the fluence required to induce a permanent drop of transmissivity. As mentioned, our goal here was to extend the FROSt technique to the SHG microscopy system and this further encouraged me to become familiar with the nonlinear microscopy world.

Second harmonic generation (SHG) is an instantaneous coherent process where two photons with equivalent frequency convert into a single photon with double the frequency of the initial photons [22,29]. This is a second order nonlinear process which only occurs in non centrosymmetric structural organization [22]. This is the case for most piezoelectric [30], pyroelectric and ferroelectric [31] materials. It is also the case for some biological tissues made of collagen [32–35], cartilage [36–38], microtubules, and skeletal muscle [39,40]. Implementing this concept inside a microscopic system makes a powerful measurement technique to verify the inversion symmetry of a material [41].

The possibility of controlling linear optical behaviors like refractive index gave birth to widely used electro-optic modulators [42,43]. This concept inspires to control nonlinear properties as well. For instance, controlling the second order susceptibility (responsible for second harmonic (SH) signal) can give birth to SHG transistors which forms resourceful possibilities [44] and here, we discuss the prospect of tuning the SHG emission of a transition metal dichalcogenide (TMD) through the alternation of exciton charging effects. This concept has been successfully demonstrated with electrostatic doping [45,46] and here we look for an alternative approach which is free of external gating to achieve a similar outcome. To comprehend this concept better, TMDs and their larger family, which is two-dimensional materials (2DMs) will be discussed.

The family of 2DMs is limited to materials with only a single or few layers of atoms [47] and since its first introduction in 2004 [48], this research field has gained enormous attraction. Generally, when we think about material properties, we usually only consider the type of that material. Though, this assumption is not entirely correct. Significant properties like conductivity or even light-matter interactions are associated to the size and dimension of a material as well [49]. There are various studies that superimpose different 2DMs - as building blocks [50] - to manipulate and obtain more complex structures (superlattices) and achieve superior functionalities [50]. Though, due to the processing incompatibility between the dissimilar 2D materials, there are difficulties involving high-order superlattice structures [51]. An interesting approach to avoid this issue is to use molecular layers into these superlattices (hybrid superlattices). This approach widens the range and potential properties of this family since there is an unlimited number of degree of freedom in the design of molecular arrangements (molecular architecture) which can change the whole block's properties [51]. In Chapter 3 of this thesis, with the help of the SHG microscopy system, I worked on the evaluation of attaining SHG tunability through molecular architecture. For this experiment, a 2D continuous molecular layer was vertically stacked in a building block to tune the SHG. In summary, we evaluated the ability to manipulate the optical properties of superlattices and the outcome is explained in details in Chapter 3.

As mentioned earlier, our goal here was to gain expertise in different aspects of nonlinear optics. After working on ultrashort pulse characterization and then using ultrashort pulses for material characterization (using SHG microscopy), I wanted to learn more about spectral broadening and ultrashort pulse compression techniques. Usually, the generation of ultrashort pulses with few optical cycle duration requires first to increase the bandwidth of the laser pulses, and then to compensate the nonlinear spectral phase through dispersion compensation [52]. In 1987, a newly developed technique for pulse compression was introduced by propagating pulses through a single mode fiber. The idea is to broaden the spectrum through self-phase modulation [14]. This technique was successfully used to compress a 50 fs pulse to 6 fs at 620 nm [14]. Though, single-mode fibers are limited to the energy range of nJ which can be labeled as low energy due to the appearance of high order nonlinearities. In 1996, by replacing the single-mode fibers with hollow core fibers (HCFs) filled with noble gases, this issue was rectified and a state-of-the-art pulse compression at mJ level by self-phase modulation (SPM) was made possible. Here in the group of Prof. François Légaré, a study is underway on pulse compression in HCF using molecular gases [27,53–55].

Pulse compression induced by self-phase modulation in HCF using noble gases is a well-known topic, since they have a high ionization potential and insignificant dispersion at low pressure [56–60]. Raman active gases by delayed nonlinear response from the excitation of rotational or vibrational modes have been neglected till recently [27]. Here in our team an investigation was conducted (led by Reza Safaei and Fan Guangyu) to study the spectral broadening (induced by Raman active gas) by using nitrogen (N_2) as the molecular gas filling the HCF [55]. In this study, the broadening induced by N_2 is completely asymmetrical and favors the generation of frequencies at longer wavelengths (red-shifted). This spectral broadening is established on the nonadiabatic molecular response, which is described as the delayed molecular response. Basically, the molecular response to the pulse temporal profile is delayed, which generates new frequency at the leading edge. Perhaps the main highlight of spectral broadening by this technique in comparison to SPM based broadening is the efficiency of this technique for picosecond pulses, which is significant as an application for Yb laser sources. The path to understanding the nonlinear physical aspects of broadening caused by this molecule was further continued in another publication, which is out of the scope of my thesis [53]. After working as an experimental team member on this study, I pursued my own investigation with N_2O which has a slower molecular response in comparison to N_2 . The broadening was scanned with respect to the input pulse duration, input pulse peak power and molecular pressure. Our finding indicates asymmetrical broadening relatively broader in comparison to N_2 . The result of this investigation is explained in Chapter 4.

To summarize, for each chapter, a literature review is provided to put my work in context. Chapter 2 discusses the implementation of FROSt to characterize pulses with nanojoule energy. In Chapter 3, SHG

microscopy is used to evaluate the SHG tunability of TMDs. Finally, Chapter 4 discusses spectral broadening and pulse compression using nonlinear propagation in hollow core fibers filled with molecules. Finally, a conclusion to discuss potential outlook is provided.

Chapter 2

Pulse characterization with Frequency Resolved Optical Switching

Ultrashort pulses are the best tool to track and control ultrafast phenomena since they are the shortest artificial events ever created by humans; they are considered as the ruler to measure ultrafast events [61]. One essential requirement of using ultrashort pulses to probe an event is to make sure that these pulses are shorter than the measured event [62]. Intensity autocorrelation based on second harmonic generation was the first successful approach to characterize the temporal duration of ultrashort pulses without the requirement of known reference pulses [63]. This technique is based on measuring the ultrashort pulse by itself using a nonlinear process such as second harmonic generation [61]. Though, this technique provides only an estimation of the pulse temporal duration since different pulse temporal structures can give the same SHG autocorrelation. However, only knowing the temporal duration of the pulse is not always sufficient. For instance, the pulse structure can play a significant role in understanding the result of an experiment such as the study of molecular vibrations [64]. To measure the exact temporal structure of a laser pulse, its spectral amplitude and phase are required. The spectral amplitude can be easily measured with a spectrometer. However, characterizing the phase of unknown pulses remained a challenge until 1991. This issue was finally resolved by the introduction of frequency resolved optical gating (FROG) [62]. Like autocorrelation, FROG uses a nonlinear process as a gate, but instead of recording the nonlinear output using a detector, it records the spectrum as a function of time delay. Although the experimental setup is extremely simple, this technique manages to reconstruct the pulse structure by solving the two-dimensional phase-retrieval problem [24].

We can categorize advanced methods to characterize ultrashort pulses into two main groups. Techniques like FROG (introduced by Trebino in 1991) [62] and dispersion scan [65] (introduced by Miranda in 2012) are considered as spectrographic techniques [9]. Another approach to characterize ultrashort pulses is based on interferometry. One of the first techniques to characterize pulses based on this approach was spectral phase interferometry [66]. In this technique, we use a well-known characterized pulse as a reference and interfere it with the pulse of interest in the spectrometer. In this approach, the reference pulse has to cover the spectral range of the pulse of interest and the characterization is based on the interference measurement of the two pulses in the spectrometer. This technique does not require any nonlinear event, but it still requires a reference pulse with the shared spectrum which is rarely available [66]. In a next step a more advanced characterization technique based on interferometry was introduced. The idea was to use the replica of the pulse to interfere while it frequency shifted. This technique is called spectral shearing interferometry [67–69]. Finally, in 1998, the spectral phase interferometry for direct electric-field reconstruction (SPIDER) technique was introduced [70]. In this technique (which is an advanced technique), the pulse of interest is duplicated and then distanced temporarily to make two pulses well separated with no overlap. A third pulse (from the same input) by the help of dispersive optical element is strongly temporally stretched (it is stretched enough that each frequency is spaced in the time domain). By combining the two copies of the

duplicated pulse with the stretched pulse in a nonlinear crystal, sum frequency generation occurs and each of the two duplicate pulses overlaps with different parts of the long-stretched pulse. The output of the sum frequency generation is then detected by the help of a spectrometer [25]. This technique is useful for retrieving the spectral phase of the pulse.

SPIDER and FROG are both very strong techniques to fully characterize ultrashort pulses and depending on the case each have advantages and disadvantages. For instance, FROG is more suitable for longer pulses since SPIDER requires special optics to stretch the pulse sufficiently [9].

Frequency resolved optical switching (FROSt) is a newly developed technique in the ALLS laboratory [26]. This spectrographic technique is very strong for the characterization of ultra-broadband pulses, since it doesn't require the phase matching condition to create the nonlinear gate. This allows the use of this technique for characterization of ultra broadband pulses over a wide spectral range [26]. In other words, FROSt is a very strong method to characterize pulses in different spectral ranges with minimum adjustments. Nevertheless, there are some unanswered questions about this technique like the threshold of the laser pulse repetition rate which will be discussed in this chapter.

2.1 Preliminary information

Above, we have mentioned that Intensity autocorrelation, FROG, and SPIDER are using nonlinear processes for gating the ultrashort pulses to characterize it. The most widely used nonlinear process is second harmonic generation. To better explain the limits of SHG based characterization techniques, this nonlinear process will be discussed in section 2.1.2. In addition, to clearly explain why pulse characterization techniques are essential, we will discuss the effect of linear propagation on the temporal structure of laser pulses in section 2.1.3. Moreover, a brief introduction on some of the basic concepts of electromagnetic radiation is presented in the following section.

2.1.1 Brief introduction on electromagnetic radiation

In the electromagnetic spectrum (Figure 2.1), energy distribution is quantified by wavelength [71]. Another way to distinguish electromagnetic waves is frequency. Basically, frequency of light represents the number of waves that pass a point in space during any time interval. Usually frequency is represented in Hertz (Hz), which provide the number of optical cycles within one second [72]. However, for historical reasons, wavelength is usually used to represent and distinguish electromagnetic waves from each other [71].

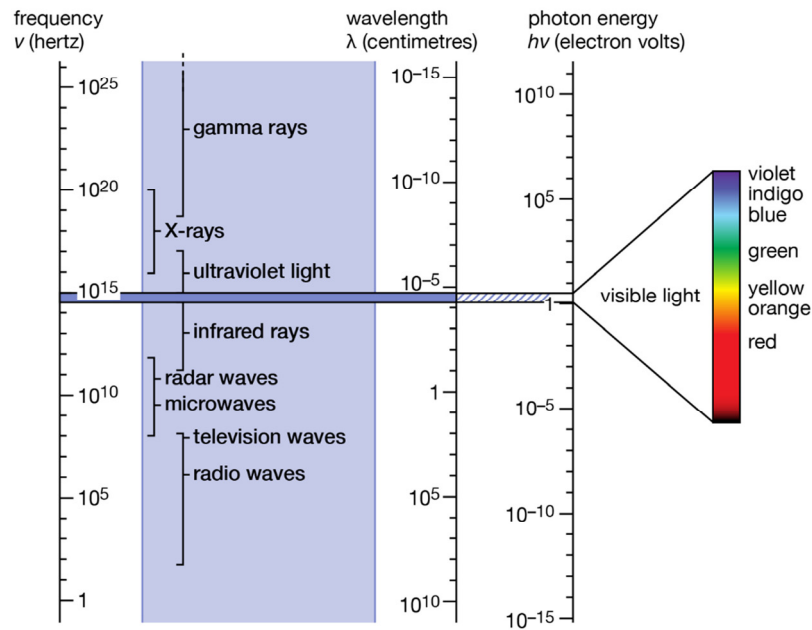


Figure 2.1: Overview of the electromagnetic spectrum. Extracted from [73].

Electromagnetic light sources can be categorized based on their properties; some common properties of light can be observed in Figure 2.2. Basically, a light source can be called monochromatic when it has only a single optical frequency (single wavelength) or in another word the bandwidth ($\Delta\nu$) is zero. Even though a laser beam doesn't have a zero bandwidth, its bandwidth is narrow enough to follow some monochromatic behavior. Theoretically laser systems are only quasi - monochromatic, but in the practical world they are commonly known as a monochromatic sources [74].

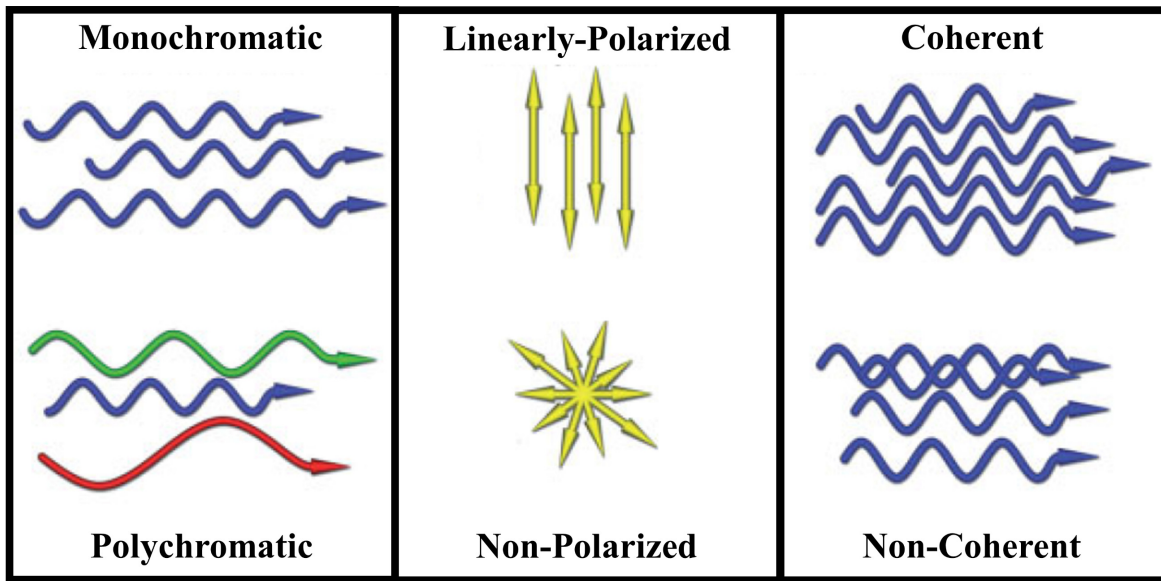


Figure 2.2: Quality of light waveform prospects. Adapted from [75].

The electric field of light is perpendicular to the direction of propagation. The output of a source is called linearly polarized when the electric field vectors vibrate in a single plane [15]. Another important quality to distinguish light sources is coherence. The output of a light source is said to be coherent when there is a fixed relationship between the electric field values in different locations, or in other words when waves maintain their same phase relationship while propagating through space. Coherence is an important property of the laser output [76].

Ultimately, since the bandwidth of a laser is finite, eventually the different frequencies in a laser beam will get out of phase with each other. Principally, the time required for two oscillations differing in frequency by $\Delta\nu$ to get out of phase by a full cycle is $1/\Delta\nu$ and by the end of this period, destructive interference between different frequency components of the pulse can occur. This period is known as coherence time which is usually represented by the corresponding coherence length $L_c = c/\Delta\nu$. In the case of ultrashort pulses, since their spectral bandwidth can be large, they have a short coherence length. Furthermore, the more bandwidth they have, the shorter they can be if the spectral phase is flat (all colors arriving together). Therefore, pulse characterization is very critical in ultrafast science and technologies, and the main nonlinear process used to characterize unknown pulses is second harmonic generation. This process is discussed in the following section.

2.1.2 Brief introduction on second order nonlinear optical response and the impact of phase matching

The discovery of the laser in 1960 [77] as a light source created an opportunity to explore non-linear effects due to their strong electric field, which lead to the experimental observation of nonlinear processes such as second harmonic generation [78] (Figure 2.3) and self-focusing [17].

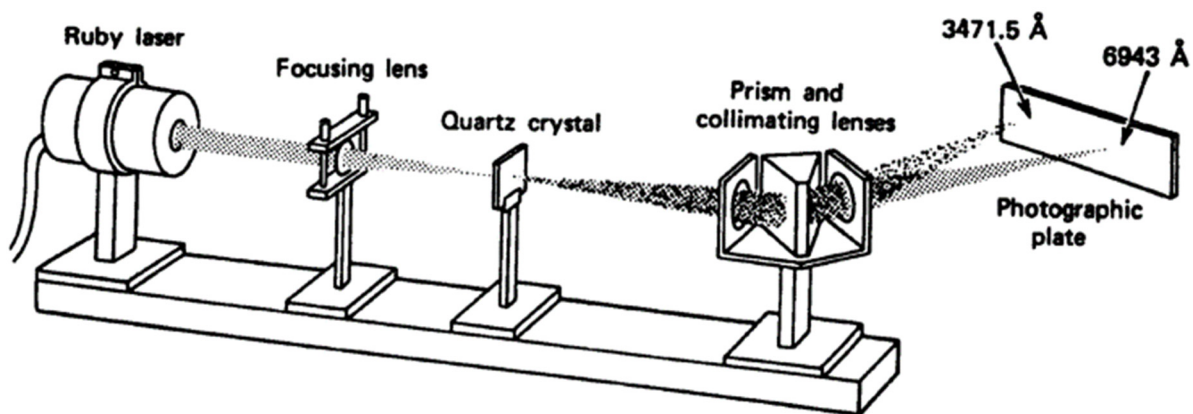


Figure 2.3: Optical setup for the first experimental observation of SHG: Focusing a ruby laser beam on a quartz crystal, lead to appearance of relatively weak beam which is separated from the input beam by a prism. Extracted from [78].

Principally, the strength of the electric field (E) affects the dipole moment per unit volume also known as polarization (P) of a material system. This relationship separates the linear and nonlinear phenomena. To observe nonlinear phenomena, a strong electric field is required to be applied to a medium such that the dipole will enter into nonlinear oscillations. Linear behavior of light which is represented in Eq.1 (like absorption and reflection) can be expressed by the linear relationship between the induced polarization and the electric field [79].

$$P(t) = \epsilon_0 \chi^{(1)} \cdot E(t) \quad \text{Eq.1}$$

where $\chi^{(1)}$ represents the linear susceptibility and ϵ_0 represents permittivity of free space.

Eq.2 represents the polarization with regular light, under a strong electric field; the polarization has also nonlinear terms which appear in the Taylor series:

$$P(t) = \epsilon_0 [\chi^{(1)} \tilde{E}^1(t) + \chi^{(2)} \tilde{E}^2(t) + \chi^{(3)} \tilde{E}^3(t) + \dots] \quad \text{Eq.2}$$

In this equation, each term represents the behavior of a nonlinear order: For instance, light propagation in a second order nonlinear medium is represented as:

$$P^{(2)}(t) = \epsilon_0 \chi^{(2)} \tilde{E}^2(t) \quad \text{Eq.3}$$

This term is responsible for a number of processes (Figure 2.4) including second harmonic generation (SHG) [78], sum frequency generation (SFG) [80], difference frequency generation (DFG) [80], and optical rectification (OR) [81].

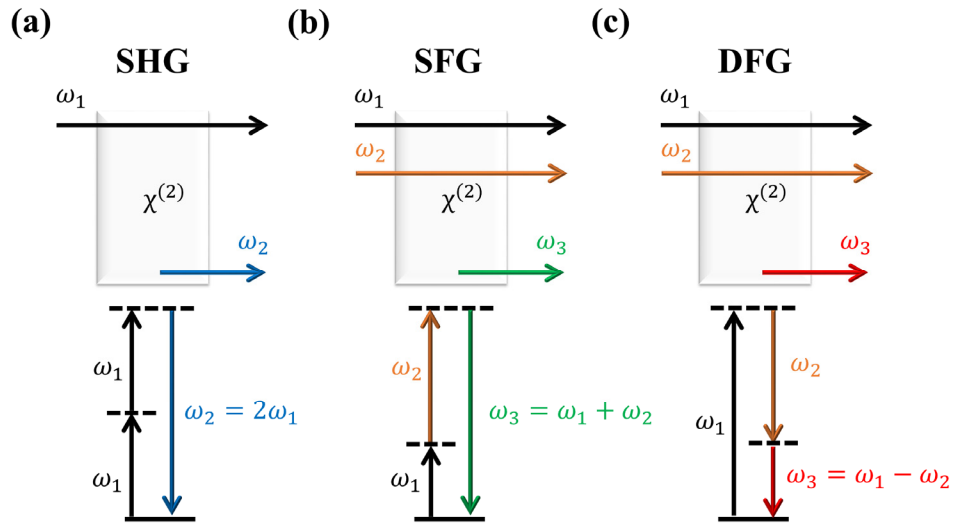


Figure 2.4: Illustration of second-order nonlinear parametric processes including, (a): second harmonic generation (SHG), (b): sum frequency generation (SFG), (c): difference frequency generation (DFG). The schematic is represented in top and the transition energy diagram is represented in bottom.

SHG is an instantaneous conversion of two photons to one photon at exactly double the frequency of the incident beam [79]. Furthermore, SHG is a parametric process where the photon energy always needs to be conserved (Eq.4): On the contrary, Two-photon excited fluorescence (2PEF) is an example of a non-parametric process which is discussed in more details in the next chapter (Figure 3.4).

$$\omega + \omega = \omega_{\text{SHG}} \quad \text{Eq.4}$$

In addition to the photon energy, the photon momentum is expected to be conserved as well. In other words, for this process to occur efficiently the following condition must be satisfied [82].

$$k_{\omega} + k_{\omega} = k_{2\omega} \quad \text{Eq.5}$$

Generally, the photon momentum is related to:

$$k_{\omega} = n_{\omega} \frac{\omega}{c} = n_{\omega} \frac{2\pi}{\lambda} \quad \text{Eq.6}$$

Where n_{ω} is the index of refraction at the ν_{ω} . The term phase matching happens when both Eq.5 and Eq.6 are simultaneously satisfied. Considering the SHG process from Eq.5 and Eq.6, phase matching is achieved when:

$$n_{\omega} = n_{2\omega} \quad \text{Eq.7}$$

However, dispersion prevents the refractive index of ω and 2ω to be equal (Figure 2.5a). This condition is circumvented (Figure 2.5b) through birefringent materials or quasi-phase matching [22,82].

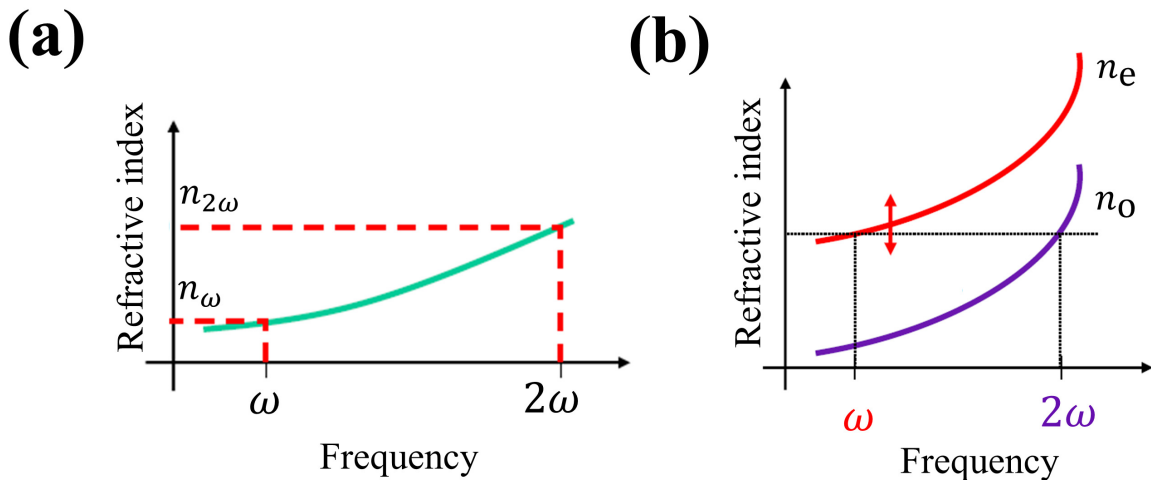


Figure 2.5: (a): Refractive index is related to the frequency, thus the condition in Eq.7 cannot be satisfied. (b): Birefringent materials have ordinary and extraordinary refractive indices. Phase matching can be satisfied through using the extraordinary polarization for ω and ordinary for 2ω . Adapted from [83].

Moreover, since the refractive index is related to the frequency (Eq.6), satisfying the phase matching condition over a broad spectral range is difficult. For instance, phase matching for BBO crystal (a common birefringent crystal) does not occur below 400 nm. Overall, the phase matching condition is satisfied when the momentum and energy of photons are conserved throughout a nonlinear process. Satisfying phase matching in bulk materials is critically important on the efficiency of SHG. The SHG phase matching (for nanoscale materials) is further discussed in Chapter 3.

This section was an introduction to the SHG process and the importance of satisfying the phase matching condition. Later in section 2.4, we will introduce the FROSt technique for ultrashort pulse characterization. One of the main advantages of this technique in comparison to SHG based pulse characterization techniques is the fact that it does not require satisfying the phase matching condition.

In the following section, we discuss some of the ultrashort pulse properties like: intensity, spectral phase, pulse temporal duration and time-bandwidth product. This section is helpful to understand what we are looking to characterize while going through different techniques in the upcoming sections.

2.1.3 Description of ultrashort laser pulses

A pulse can be simply explained as a very short burst of electromagnetic energy, with its time-dependent electric field component being the product of a temporal envelope with an oscillating sine function [84]. The relationship between the temporal width and the spectral width of a pulse is inverse (Figure 2.6), and this means that the broader a pulse is in terms of spectral bandwidth, the shorter its duration can be [85].

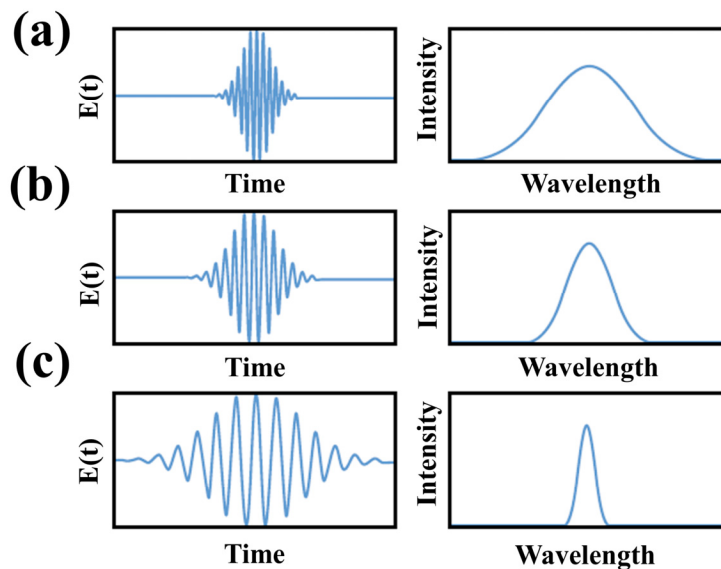


Figure 2.6: Simple illustration of the relationship between the pulse duration and the spectral width for (a-c): short-long pulse. Adapted from [83].

An ultrashort pulse can begin with a specific frequency and end at an entirely different frequency: this is defined by the chirp. Additionally, the variation of frequencies of the pulse in time can be altered because of various reasons, some even as simple as linear propagation through air [61]. That's why it's very important to characterize the temporal structure (amplitude and phase) of laser pulses.

Proper description of a pulse can be given by its electric field (Figure 2.7) expression using scalar approximation in Eq.8:

$$E(t) = \sqrt{2I(t)/\epsilon_0 c} e^{i(\omega_0 t - \phi(t))} \quad \text{Eq.8}$$

The temporal intensity and phase of the pulse are commonly known as $I(t)$ and $\phi(t)$ respectively. Though, only the imaginary part of the temporal electric field Eq.8 is usually sufficient to represent the pulse [86].

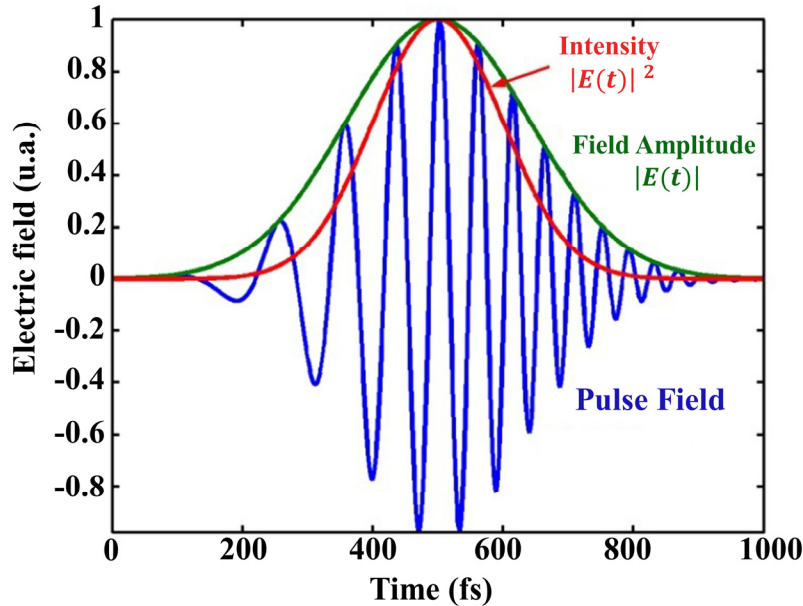


Figure 2.7: Ultrashort pulse field representation. Extracted from [61].

The frequency and the temporal domain are linked through the Fourier transform [87]. Through this function (Eq.9), the electric field of the pulse in the time domain can be converted into the frequency domain (Eq.10).

$$\tilde{E}(\omega) = \int_{-\infty}^{\infty} E(t) e^{-i\omega t} dt \quad \text{Eq.9}$$

$$\tilde{E}(\omega) = \sqrt{S(\omega)} e^{-i\varphi(\omega)} \quad \text{Eq.10}$$

In this equation, the spectral amplitude and phase is represented as $S(\omega)$ and $\varphi(\omega)$ respectively. We can also get the spectrum by [61]:

$$S(\omega) = |\tilde{E}(\omega)|^2 \quad \text{Eq.11}$$

Directly measuring the time-dependent electric field of a laser pulse is not possible with standard detection devices (e.g. photodiodes). These detectors cannot provide the required sub-femtosecond temporal resolution (an optical cycle at 800 nm is 2.66 fs) [88]. Thus, pulse characterization techniques are based on measuring the spectra of the laser pulses with a standard spectrometer, and the spectral phase is retrieved using advanced pulse characterization techniques. The time-domain electric field is obtained using the Fourier transform of the complex spectral amplitude by the following equation [87]:

$$E(t) = 1/2\pi \int_{-\infty}^{\infty} \tilde{E}(\omega) e^{i\omega t} d\omega \quad \text{Eq.12}$$

Here in this section, we have just described the pulse electric field in time and frequency domain. We have also briefly pointed out the prospect of transforming the information from the frequency domain into the time domain.

Evolution of the ultrashort pulse phase

The temporal phase ($\phi(t)$) can be written in terms of a Taylor series at the time zero. A typical pulse phase can be described by using only a few terms of this series.

$$\phi(t) = \phi_0 + t\phi_1 + t^2\phi_2/2 + \dots \quad \text{Eq.13}$$

Another important information in the time domain is the instantaneous frequency which is represented as $\nu_{inst}(t)$.

$$\nu_{inst}(t) = \nu_0 - (d\phi/dt)/2\pi \quad \text{Eq.14}$$

The Taylor series introduced in Eq.13 includes different orders of the phase. Principally these orders are responsible for different phase distortion phenomena, and we are going to briefly discuss a few of them.

Basically, the first term in Eq.13 is ϕ_0 which is known as the zeroth order phase or absolute phase. The absolute phase represents the relative phase of the carrier wave (Figure 2.7, blue line) in comparison to the reference envelope (Figure 2.7, green line) and this information is only interesting in pulses with one or few optical cycles and not relevant for multi-cycle pulses [61]. The second term in Eq.13 is ϕ_1 and it refers to the linear shift (Figure 2.8b) in frequency or time. This term doesn't affect the pulse shape and it would either affect the temporal delay in arrival of the pulse (linear term in spectral phase resembles as a shift in time) or spectrally shift the pulse (linear term in temporal phase resembles as a shift in frequency) [85]. The third term in Eq.13 is ϕ_2 and it's responsible for the second-order phase (Figure 2.8c). A pulse with the second order phase is commonly known as a linearly chirped pulse. This term is extremely important since it describes the frequency as a function of time, also called the chirp. The instantaneous frequency (Eq.14)

of the pulse is increased/decreased linearly in time, which leads to positively/negatively chirping a pulse. It's noteworthy to mention that by removing the chirp we can obtain the shortest temporal duration of a pulse which is known as the Fourier limited pulse (Figure 2.8a) [85].

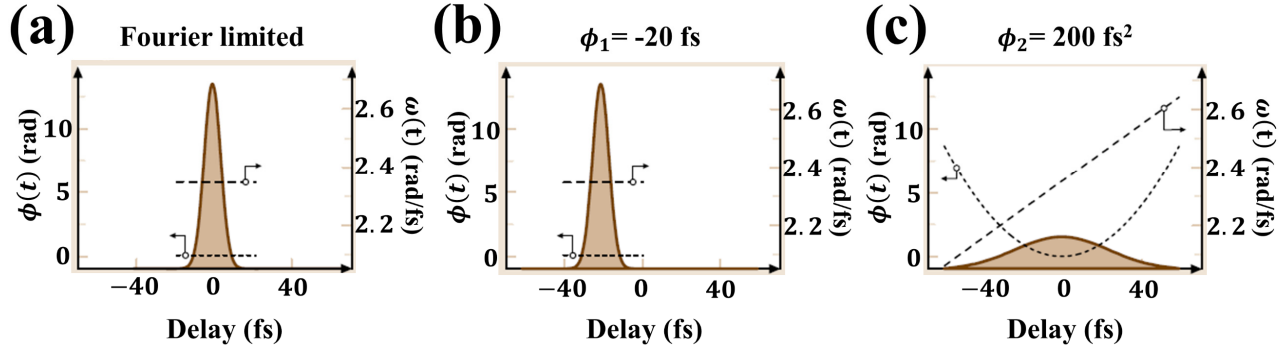


Figure 2.8: The temporal shape of 800nm Gaussian laser pulse of (a): Flat phase, (b): First order phase - shifted in time, (c): Second order phase- broadened through 200 fs² chirp. Adapted from [89].

Principally, temporal pulse duration (Δt) provides information about the pulse in terms of seconds and on the other hand the spectral width ($\Delta \nu$) provides information in terms of Hz. TBP given by Eq.15 makes it possible to estimate to what extent the pulse is close to the limited Fourier pulse since the TBP is minimal in this case [61].

$$TBP = \Delta \nu \cdot \Delta t \quad \text{Eq.15}$$

For example, the minimum obtainable TBP for a Gaussian pulse is 0.441 ($\Delta \nu \cdot \Delta t = \frac{2 \ln 2}{\pi}$) [89]. It's noteworthy to mention that Δt and $\Delta \nu$ are determined based on the intensity FWHM rather than electric field.

Ultimately, in this section, we got familiar with the representation of different features of ultrashort pulses in time and frequency domain. In the next section, we will resume our early discussion about the characterization techniques of ultrashort pulses.

2.2 The intensity autocorrelation

The information about spectra (directly acquired by a spectrometer) of a light source is not sufficient to comprehend it, and we are missing key elements like pulse temporal duration and phase. Here we will briefly discuss the journey toward one of the first ultrashort pulse characterization techniques.

Optical detectors like photodiodes and photomultipliers are devices capable of photon detection by emitting electrons in response to them [71]. The electronic response is relatively slow (1 ns) which means they only

have the capability to determine the integral of the pulse intensity [61]. More importantly, the optical detectors are too slow in comparison to ultrashort pulses and ultimately the only available event short enough to monitor the pulse is the pulse itself.

Historically, intensity autocorrelation, $A^{(2)}(\tau)$ is one of oldest [63,90–93] successful approaches to characterize the temporal duration of ultrashort pulses: due to its simplicity, this technique is still widely used to estimate the pulse duration [84]. This method (Figure 2.9) is based on splitting the beam into two beams and overlapping the main pulse with the delayed version of itself on a nonlinear medium to record the intensity of the nonlinear optical signal (such as the second harmonic) by a detector that allows to scan the intensity of the ultrashort pulse over time. This approach is noise free and we are only detecting the created gate from the temporal overlap of the two pulses [94].

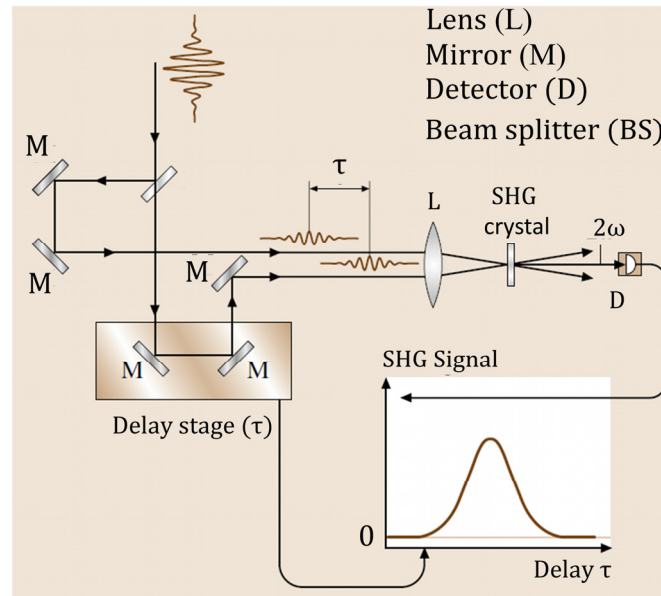


Figure 2.9: Non-collinear autocorrelator setup: Two replicas of the pulse with an adjustable delay are spatially overlapped on a SHG crystal. Adapted from [89].

In the case of SH intensity autocorrelation, the second harmonic signal is proportional to the product of the intensities of two pulses (Eq.16).

$$A^2(\tau) = \int_{-\infty}^{\infty} I(t)I(t - \tau)dt \quad \text{Eq.16}$$

This technique is not very accurate on the pulse shape, and we are required to assume a Gaussian or another temporal shape from it. In this method, the shape of the pulse is always symmetric, and we cannot distinguish any asymmetric shapes (like third order spectral phase). The intensity autocorrelation (Eq.16) basically only provides information about the evolution of the intensity in time and lacks any information about the actual phase. Retrieval of the spectral phase through reconstruction algorithms of the pulse based on intensity

autocorrelation is considered as an unsolvable 1D phase retrieval mathematical problem [95]. In summary, intensity autocorrelation is not sufficient, and even combining this information with the spectrum is unsuccessful to determine the phase of the pulse [96].

2.3 Frequency resolved optical gating (FROG)

Frequency resolved optical gating was the solution to the long-lasting issue of being blind about the spectral phase of ultrashort pulses. In this approach the problem is solved in the joint time-frequency domain [97,98] by measuring (Figure 2.10) the spectrogram of the pulse [99].

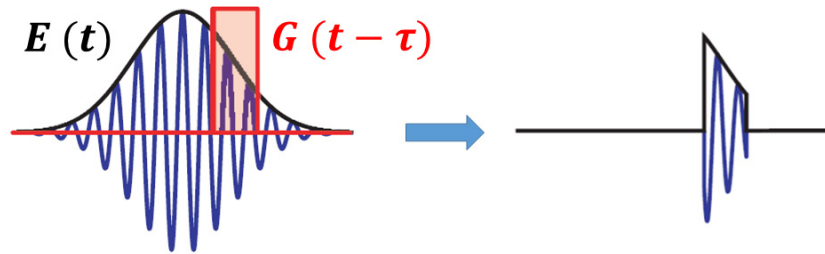


Figure 2.10: Gating the electric field temporally and then recording the spectrum of the gate in terms of the delay. $G(t-\tau)$ denotes the gate or window function (the overlap between $E(t)$ and $E(t-\tau)$). This allows simultaneous record of the arrival time and frequency of an optical wave. Extracted from [83].

In the simplest form, the optical approach of FROG is as simple as autocorrelation: creating a gate through the nonlinear interaction of the pulse with a delayed version of itself. However, the information is recorded using a spectrometer instead. Basically, this amounts to recoding (Figure 2.10) the critical information of spectrum vs. delay.

$$I_{FROG}^{SHG}(\omega, \tau) = \left| \int_{-\infty}^{\infty} E(t)E(t-\tau)e^{-j\omega t} dt \right|^2 \quad \text{Eq.17}$$

Eventually, this approach (Eq.17) reconstructs the spectral phase with the proper inversion algorithm [3, 25]. FROG is a two-dimensional phase retrieval problem which has a unique solution: basically FROG trace retrieval is an inverse problem, matching the correct question to the solution you already have [100].

As mentioned, FROG is based on the appearance of a nonlinear gate and the most common approach is known as SHG FROG [100]. SHG FROG is very reliable and sensitive for pulse reconstruction, but there are limitations involving the satisfaction of SHG phase matching requirement (section 2.1.2) depending on the input wavelength (Eq.6) and pulse duration [22]. It's noteworthy to mention that the crystal used for SHG FROG should have appropriate thickness, smaller crystal thickness would provide the capability to measure pulses with more bandwidth [61].

Illustration of SHG FROG

In this part, we will go through an example of this technique for the characterization of ultrashort pulses. I took the following FROG trace in ALLS laboratory while working on a subproject. This trace belongs to a Ti-Sapphire oscillator output which was stretched and amplified at 50Hz repetition rate. The amplified output was then compressed using a pair of gratings in the compressor. This trace was acquired using a homemade build SHG FROG, and I reconstructed the pulse based on the algorithm developed by *R. Jafari*, *T. Jones* and *R. Trebino* [101].

Here in Figure 2.11b the intensity and phase of our pulse is represented in the time domain. It's noteworthy to mention that the phase where the intensity (blue line) is zero is meaningless and we are supposed to remove the phase information outside of the interested area, this task is known as phase blanking [61]. Our SHG-FROG trace (Figure 2.11a) illustrates a third order phase (ϕ_3). Basically, ϕ_3 leads to a quadratic group delay where the central frequency arrives before the frequency at the sides.

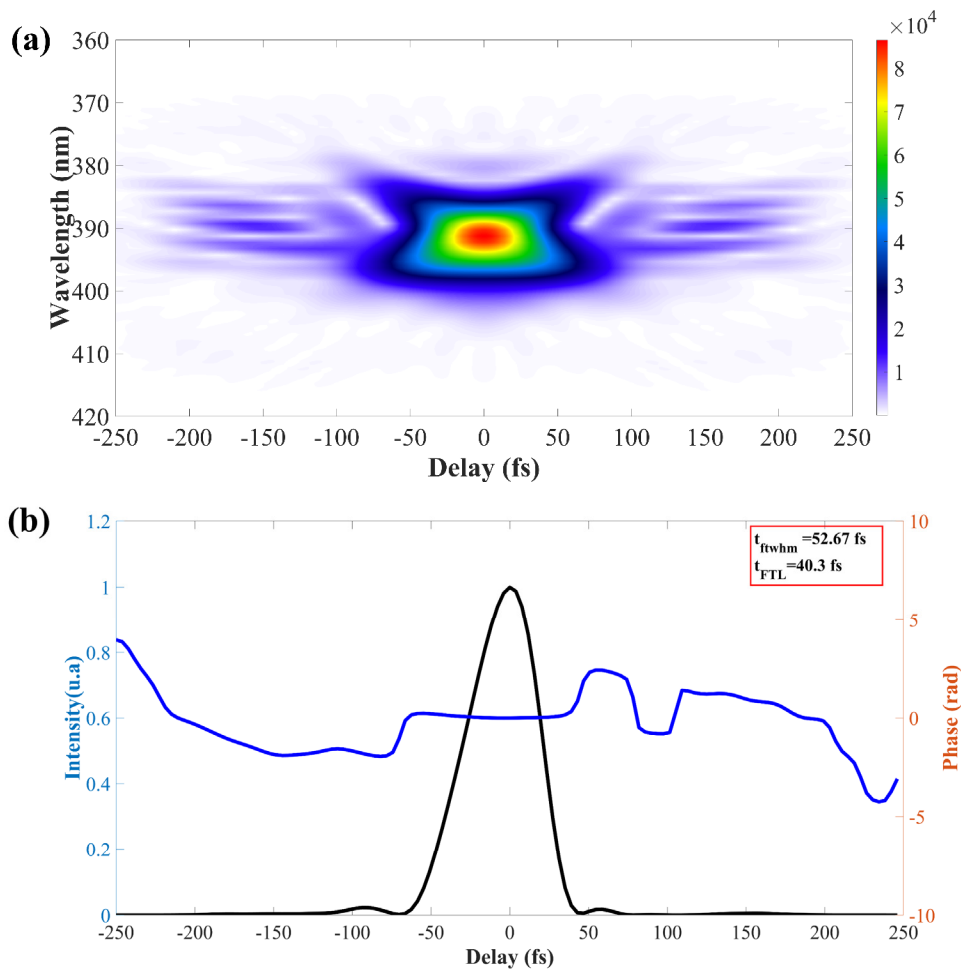


Figure 2.11: SHG-FROG (a): Reconstructed spectrogram trace. (b): The intensity (black line) and phase (blue line) temporal evolution. Here we have a 52 fs pulse with third order phase behavior ($\phi_3=1465$ fs³)

2.4 Frequency resolved optical switching (FROSt)

Frequency resolved optical switching (FROSt) is a newly developed technique at the advanced laser light source (ALLS) laboratory based on transient absorption in solids [26]. The optical approach (Figure 2.12) of FROSt can be as simple as a pump and probe setup.

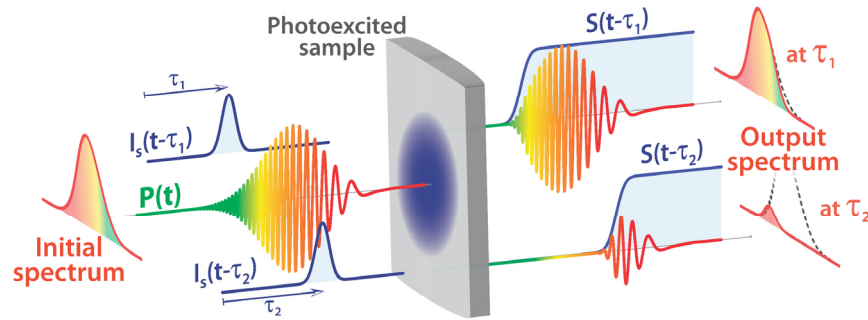


Figure 2.12: Principle of the frequency resolved optical switching. The initial spectrum of the probe is recorded in terms of the time delay. Extracted from [26].

In this technique, an intense ultrashort pulse (pump) is used to photoexcite the electrons of a solid (low band gap material) from the valence band to the conduction band. This absorption will act as a semiconductor switch (Figure 2.13) and as a result, the optical transmission of the probe will drop and will recover over a time duration much longer than the pulses that we want to characterize. This switch originates from the photoexcited carrier dynamics, which acts as a temporal knife-edge, slicing the probe pulse waveform [26,102].

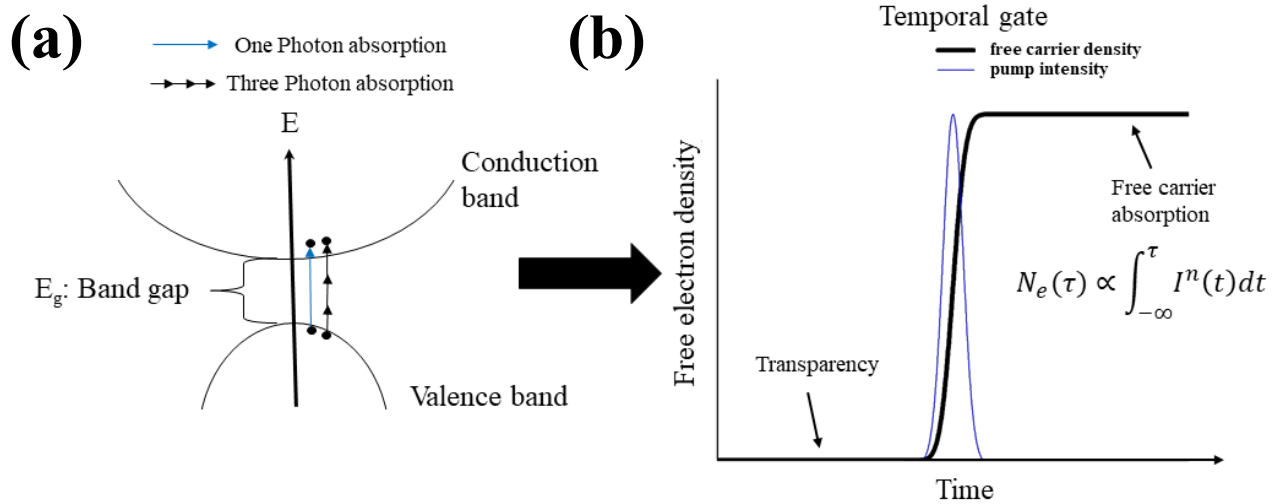


Figure 2.13: Transient absorption processes. This absorption will act as a semiconductor switch.

In this technique, the transmitted spectrum of the probe is recoded as a function of time delay and then the output spectrogram is used to reconstruct the temporal profile of the probe and switch with ptychography algorithm. The critical requirement of this method is to have a pump with sufficient intensity to induce the photoexcitation process and the benefit of this technique is that it avoids phase matching requirements since there are no frequency conversion [26].

In this approach, the transmission drop provides encoded information about the optical switch and the cut-off delay of each frequency provides phase information. The FROSt retrieval algorithm is based on the well-known spatial ptychography used in microscopy [28].

$$I(\omega, \tau) = \left| \int_t P(t)S(t - \tau)e^{i\omega t} dt \right|^2 \quad \text{Eq.18}$$

This algorithm is transposed into the time domain and the phase retrieval algorithm was developed specifically for this pulse characterization technique. The switch $S(t)$ is the temporal equivalent of an object in the traditional ptychography which is formed by pump $I_s(t)$. In this process, the spectral amplitude and phase of the probe are required to be recovered. Ultimately, this technique has the complete capability of temporal characterization of ultrashort pulses [26]. In this technique, the photoexcited solid only affects the switch created by the pump. The reconstructed pulse is free of any influence from it: this concept has been verified through characterization of the same pulse using different solid materials (refer to Figure 8 in [26]).

As we mentioned earlier at the beginning of the chapter, FROSt is a strong tool for the characterization of ultra-broadband pulses [26]. For instance, the output of an OPA pumped by a Ti-Sapphire laser covers a spectrum range from 1.2 μm to 20 μm , and there is no available standalone commercial system to fully characterize the temporal profile of the OPA output in its full spectral range of operation. FROSt can characterize over such broad spectral range with minimum adjustment [26].

Illustration of FROSt

Here we will go through an example of this technique for the characterization of ultrashort pulses. I took the following FROSt trace in ALLS laboratory while working on a subproject. Using an OPA we generated a signal and an idler at 1.4 and 1.8 μm . After the amplification, 7 μm mid IR pulses were generated using a difference frequency generation (DFG) in a 180 μm -thick GaSe crystal.

When we take a FROSt trace, we can use any pump as long as it has sufficient intensity to photoexcite the medium. Here we use the 7 μm mid IR source as our probe and to pump, we use the available 800 nm which has sufficient intensity. It's noteworthy to mention that the pump and probe should overlap spatially and temporally in the medium. Figure 2.14 represents the probe transmission evolution while we change the delay between the pump and probe.

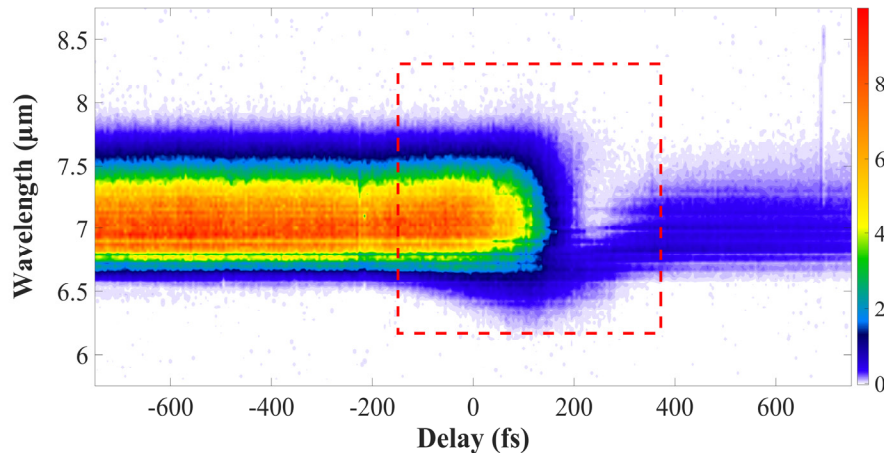


Figure 2.14: The FROSt spectrogram of the 7 μm MID IR source. The silicon medium was photoexcited by the 800 nm pump.

The acquired trace in Figure 2.14 contains the critical information regarding the delay position for the cut-off transmission at each specific wavelength of the probe spectrum. Using this information, the FROSt algorithm was used by my teammate to reconstruct the pulse (Figure 2.15). The 7 μm Mid IR source generates ultrashort pulses with 153 fs temporal duration, which is near the Fourier transform limit (146 fs).

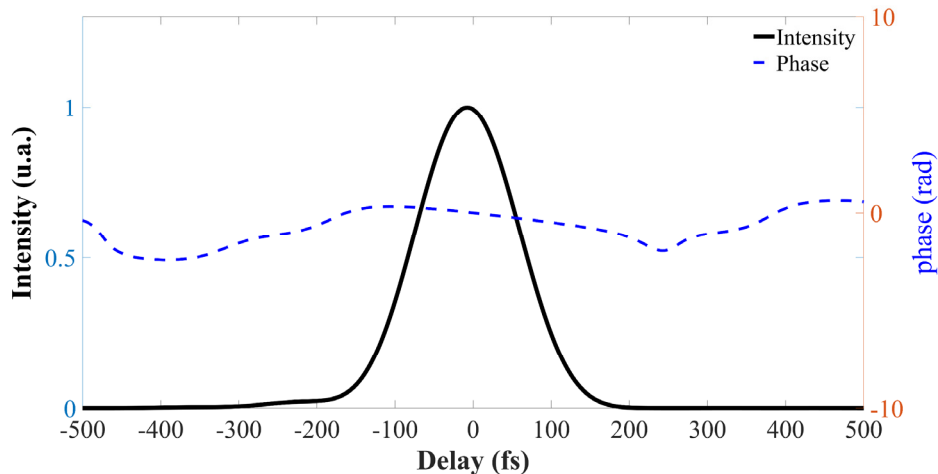


Figure 2.15: The intensity and phase temporal evolution of the pulse. The temporal duration of the pulse is 153 fs (Second order phase: -192 fs^2 , Third order phase: -7621 fs^3). The FROSt reconstruction was performed by Philippe Lassonde.

Figure 2.16 shows the transmission of the probe as a function of the delay for one specific wavelength. The temporal overlap will induce a gradual drop of transmission, and here we have a 98% drop. Currently, the FROSt algorithm is capable of reconstructing traces which have at least 10% transmission drop. This information is important for our upcoming discussion in section 2.5, since we would like to further develop this technique for high repetition rate lasers.

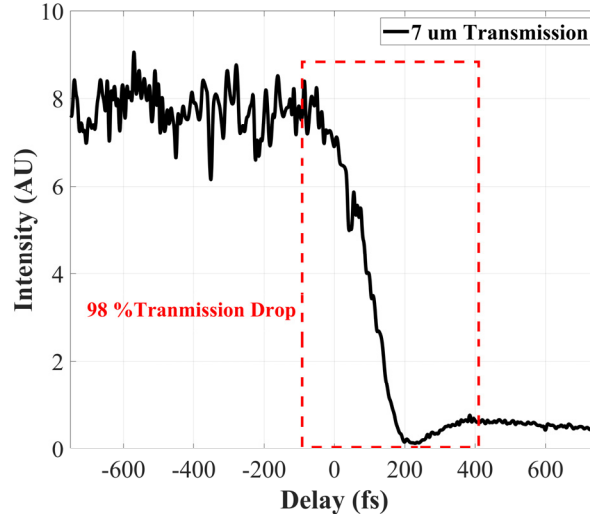


Figure 2.16: The arrival of the 800 nm pump will induce a gradual drop on the 7 μm transmission of the probe.

2.5 Investigation of transient gate at different repetition rates

As mentioned, the optical approach of FROSt is based on photoexciting the solid through a strong pump and monitoring the variation of the probe spectrum induced by the photoexcited solid. The proof of concept of this technique was achieved using μJ pulses with a 100 Hz repetition rate laser system. Essentially, we don't have the complete information about the pump pulse features necessary to create the gate of this technique: For instance, we suspect the relaxation time of the solid material (after photoexcitation) may cause limitation on the operation of this technique on laser sources with high repetition rate. Since high repetition rate oscillator systems are widely applied in the optical world (specially in nonlinear microscopy), an investigation was conducted here to find more about the limitation of using FROSt to characterize it. The overview of the initial experimental setup is represented in Figure 2.17. A 80 MHz Ti-Sapphire oscillator output was used as the source of the investigation.

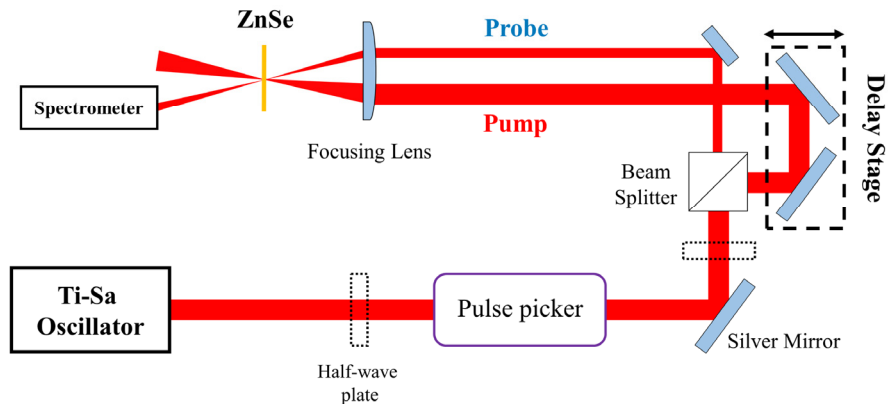


Figure 2.17: Initial experimental setup to investigate FROSt operation at different repetition rates

Lack of transient gate

The optical approach of this technique is as simple as a non-collinear SHG FROG. To start the experiment, first the temporal overlap of the setup is certified using SHG upconversion in a BBO crystal. Then we only need to switch to our solid (ZnSe) and monitor the probe transmission before and after the temporal overlap with the pump: we are looking for a transient gate (Figure 2.18) to reconstruct the spectrum of the probe as a function of the delay. However, no transient gate (drop of transmittance on the probe) was observed through our initial attempt.

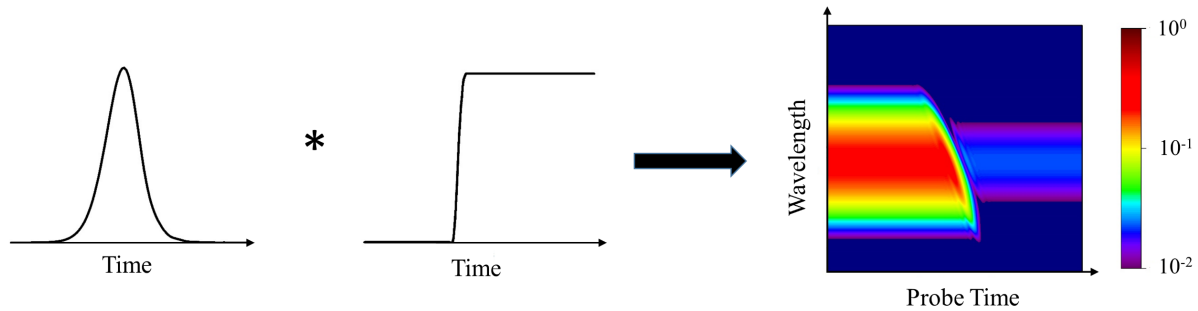


Figure 2.18: Transient gate which creates a gate for the probe and the reconstruction occurs based on the location of each frequency cut-off.

Numerous attempts were conducted to improve the spatial overlap but no transient gate was ever observed. As mentioned, this technique was demonstrated in the ALLS laboratory using a 100 Hz source with μJ pulses. Thus, the lack of sufficient energy (nJ) and the high repetition rate (80 MHz) effect on the solid are the two main possible causes for the unsuccessful observation of the transient gate. At this stage, I investigated different available optical focusing (30cm – 5 cm) geometries at maximum available output power (1000 W) of our laser system to improve the pump fluence. However, this did not solve the problem. At this stage, we highly suspected the repetition rate as the cause of failure, and we did not proceed to further improve the energy density by using objective lens geometry. For this purpose, a pulse picker was used to decrease the repetition rate of the oscillator.

Searching for the transient gate while scanning the laser repetition rate

This task was executed by synchronizing the pulse picker with the clock of the oscillator. Since the transient gate of this investigation is only recognizable based on monitoring the probe transmission, performing clean and accurate pulse picking is critically important for this investigation. For a high-quality pulse picking, we are required to check the quality of the phase lock by the help of an oscilloscope and the key is finding the balance between the maximum energy, the phase lock and the bandwidth of the pulse through alignment and synchronization.

We started the investigation at 100 Hz, which is the exact repetition rate as the proof of concept of this technique in ALLS. For this scan, 10 nJ pump pulses were used at 50 μm diameter, which is the approximate equivalent of 0.5093 mJ/cm^2 and here, no change was observed in the probe transmission. We knew 100Hz is a low enough repetition rate that should work. Consequently, the observation of transient gate means that our pump fluence was not sufficient to photoexcite the solid. One of the first attempts to observe the transient gate was to scan the repetition rate systematically. Although increasing the repetition rate would not change the energy density of the pulses, it would affect the power density. Basically, this may solve our issue since a switch through saturable absorption (transient gate) can occur with extreme power density close to the crystal damage threshold.

The attempt for a systematic increase of repetition rate was unsuccessful to observe any transient gate as well. We tried numerous different approaches to solve the unsuccessful efforts. The first attempt was to repeat the scans at different focusing geometries. With the help of a 5cm focusing lens, we improved the energy density of the pump to 12.73 mJ/cm^2 . We repeated the scan at various number of repetition rates but no transient gate was observed.

Improving the stability of the system

Since the energy and stability of the source was a major restriction for the execution of this experiment, further modification was performed on the main oscillator source (Figure 2.19). The oscillator cavity was completely realigned step by step to maximize the energy while maintaining maximum stability of the system. This task was successfully achieved and the overall output energy was improved from 1000 mW to 2300 mW. In addition, the new output of the oscillator bandwidth was significantly improved, which would allow further pulse temporal compression.

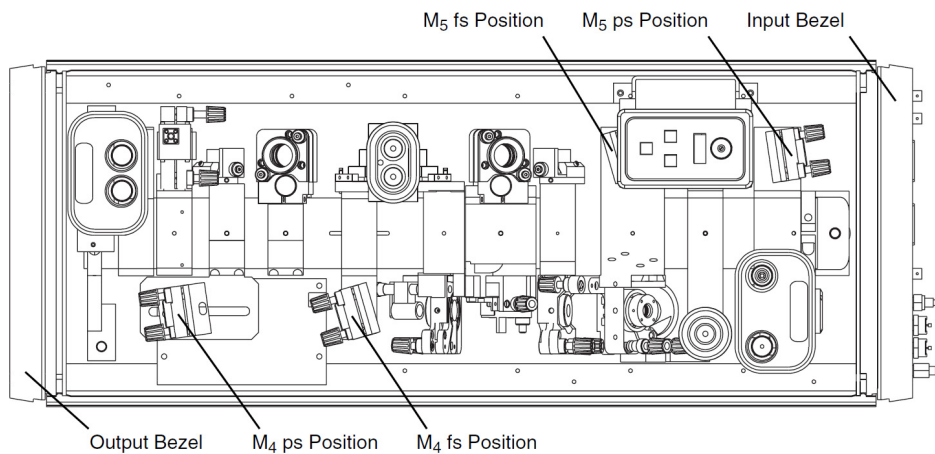


Figure 2.19 Inside the Tsunami Oscillator. Modification intended for exploiting the maximum energy.

Next, I worked on the pulse picker stage to keep the pulse energy at the maximum level with minimum loss while adjusting the repetition rate. To achieve this, the pulse picker stage was kept at over 95% transmission, with time lock synchronization between the oscillator and the electronic pulse picker. This task was quite critical on the upcoming observed data.

Finally, after numerous attempts to improve the stability of the system, a gate (Figure 2.20) was observed while monitoring the probe transmission. The observed gate was scanned for different repetition rates (100 Hz – 80 MHz) and this gate clearly appeared from 100 Hz to 10 MHz. It's noteworthy to mention that this gate was occurring even at 80 MHz, but the signal was noisier.

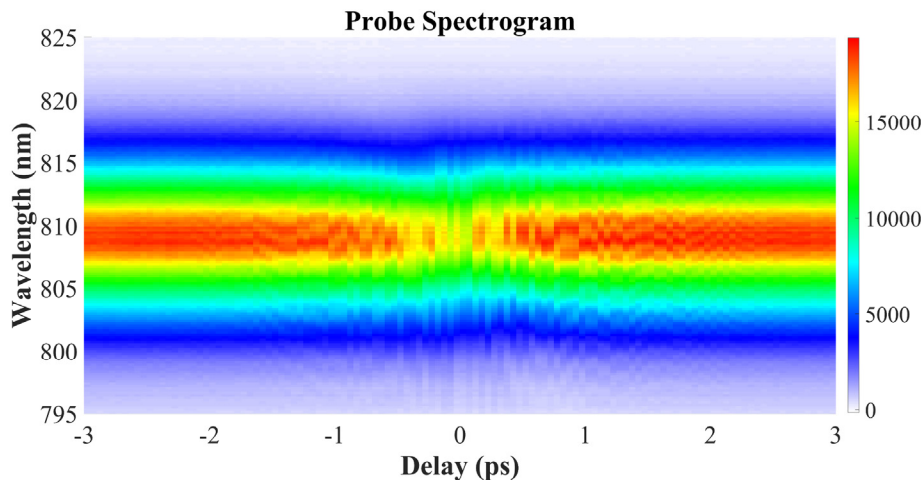


Figure 2.20: Probe output spectrogram at 400 kHz repetition rate.

The appeared gate from 100Hz to 10MHz always had around 0.86% of transmission drop, which is dramatically smaller than the 98% drop of Figure 2.16. It's noteworthy to mention that since this transmission drop is extremely low (close to the laser and pulse picker noise level), to observe this gate I was required to find a way to extremely stabilize the laser and the pulse picker stage. That's why I spend a lot of time learning about maintaining maximum stability of the system, before observing the gate. As mentioned in section 2.4, the current threshold for the transmission drop to successfully reconstruct the pulse using the FROSt algorithm is 10% and here although we have found our gate, we are unable to reconstruct the pulse since the transmission drop was not sufficient for the algorithm.

Improving the transmission drop

To solve this issue and improve the transmission drop for the transient gate we had two different ideas to move forward, the first idea was to improve the energy density by using a tighter focusing geometry. For this purpose, we needed to use an objective lens to reach the sufficient pump fluence. There are some physical difficulties involving this idea: principally the probe beam size must be no bigger than the pump

beam size, so if we are using an objective lens for our pump, we need to find a way to match the focal spot of the pump for the probe as well.

The second idea was to increase the photon energy of the pump. Basically, ZnSe bandgap is equal to 2.7eV and to reach transient absorption with our 800nm (1.54eV) pump we require high energy density. By changing the pump photon energy to 400 nm (3.1 eV) we would need a lower energy density since the photon energy is surpassing the bandgap. For this purpose, we used a BBO crystal for double frequency conversion of the pump. To improve the conversion, our pump was focused onto the BBO crystal using a lens with 5 cm focal length. The new wavelength of our pump was at 400 nm and the silver mirrors used on the optical line of the pump were switched to the UV enhanced aluminum mirrors to maintain maximum propagation transmission. Unfortunately, using a pump with higher photon energy was unsuccessful to activate a clear transient absorption gate at any repetition rate (100Hz to 80MHz). Ultimately, even though our photon energy is higher, we lack the sufficient fluence since we are also losing energy on the SHG conversion.

Improving the SHG conversion through temporal compression of the 800 nm pulse

At this stage, we tried improving the pump SHG conversion through matching the crystal thickness and angle but this was not sufficient. Moreover, we temporally compressed the 800-nm pulse to induce higher SHG conversion using higher input peak power (Eq.19).

$$P_{peak} = \frac{P_{avg}}{F_{rep} \times \tau_{pulse}}, \quad \text{Eq.19}$$

Where τ_{pulse} depends on the pulse shape as well.

I used a home-built FROG system to characterize the 800 nm pulses. Initially our pulse was positively chirped (Figure 2.21a, ϕ_2 : 9.76×10^3 fs², TBP: 1.57): This chirp was introduced to the pulse through the optical path, mainly at the pulse picker stage. This pulse was temporally compressed by introducing a negative chirp (using chirped mirrors). We end up with a 66.6 fs (Figure 2.21b) ultrashort pulse with 0.441 TBP and 16 fs² ϕ_2 which is close to the Fourier transform limit pulse. Before the adjustment of the source for this experiment, the Fourier transform limit of the source was around 100 fs and by adjusting the laser source, the broader spectrum permitted compressing the pulse to 66 fs.

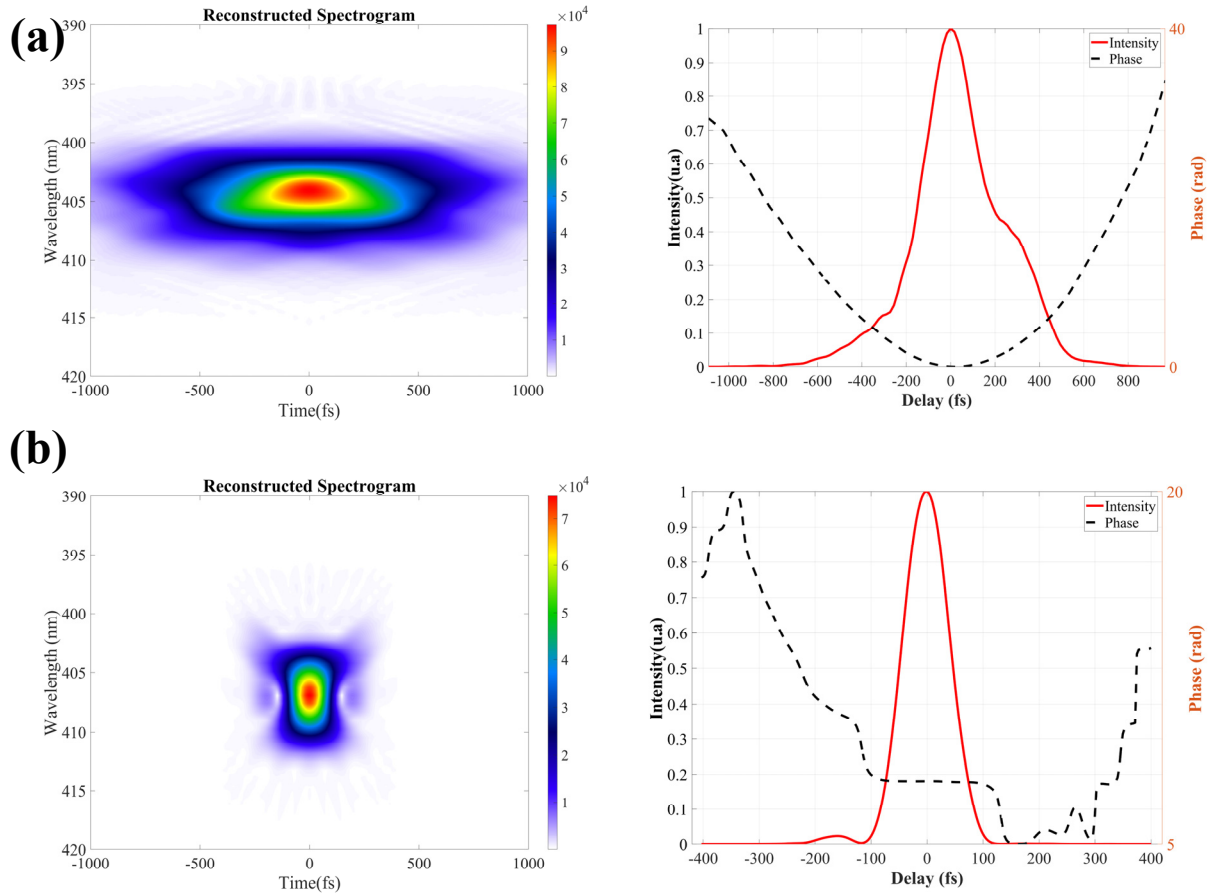


Figure 2.21: Using chirped mirrors to compress the input pulse from (a): 470 fs, $\phi_2=9.76 \times 10^3 \text{ fs}^2$ to (b): 66 fs, $\phi_2=16 \text{ fs}^2$. (left): Reconstructed spectrogram. (right): Pulse intensity and phase vs. delay.

As we discussed, the frequency doubling of the pump was not successful to create the required transient gate for this experiment. To obtain more energy at 400 nm, we compressed the pulse to 66 fs to maximize the SHG conversion on the BBO crystal: throughout this experiment, depending on the input pulse duration, the thickness of the BBO crystal was adjusted for maximum conversion. Unfortunately, even with the maximum available intensity of the double frequency pump at 3.1 eV, we were unable to observe the mandatory transient gate required for FROSt characterization. Basically, using a 400 nm pump would not solve our issue unless we reach higher energy density by either achieving far better SHG conversion or using a tighter focusing geometry.

Based on our calculation to have a sufficient drop of transmission using 800 nm pump with 15 nJ pulses, we are required to at least have a focal beam diameter of $3.45 \mu\text{m}$. The desired focal spot is possible to reach with the help of an objective microscope lens, but as mentioned earlier it's not a straightforward task to do and there are some complications which unfortunately, I was unable to demonstrate due to the heavy schedule of the beam time in the laboratory.

2.5.1 Future plan

This investigation should be continued with the help of an objective lens, which would provide sufficient pump fluence (Figure 2.22) required for the appropriate drop of transmission of the transient gate.

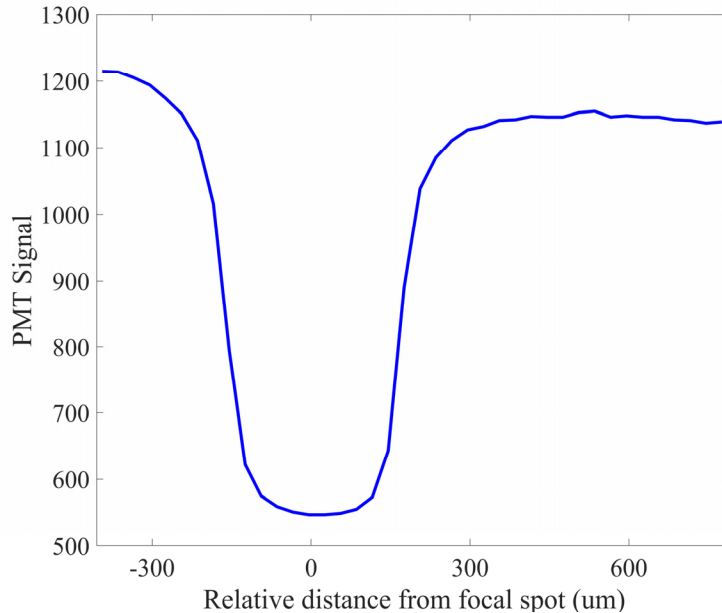


Figure 2.22: Transmission of ZnSe using a microscope objective. The X axis provides the relative position of the sample from the focal spot. This plot provides the sensitivity of the focal spot for inducing a 54% transmission drop.

As mentioned earlier, there are some physical difficulties involving this idea. Principally the probe beam size must be no bigger than the pump beam size: if we are using an objective lens for our pump, we need to find a way to match the focal spot of the probe as well. The spatial overlap of the pump and probe using collinear and nonlinear approach with a single or two objective lenses would involve some technical hitches. There are various physical difficulties to reach spatial overlap using two objective lenses in the non-collinear approach since the focal spot is too close to the objective lens. On the other hand, performing this experiment using a collinear geometry has some issues as well. If our pump and probe lines are overlapping in a collinear geometry, we don't have any suitable way to completely remove the pump line after the ZnSe medium: the distribution of energy between the pump and the probe line is 95/5 and even with the help of a polarizer we cannot completely remove the pump. Eventually, there is always a small leak which can affect the data.

My recommended approach (Figure 2.23) for this experiment is to combine the initial two ideas and use 400 nm pumping in a collinear approach while using an objective lens. We would have sufficient fluence while avoiding any noise from the pump since it is on a completely different wavelength.

Another advantage of using this approach is the fact that we can implement it into a nonlinear microscope system and characterize our pulses exactly at the objective lens of the microscope with minimum adjustments. This information can be extremely useful since the signal intensity in the second harmonic generation is inversely proportional to the input pulse duration [22].

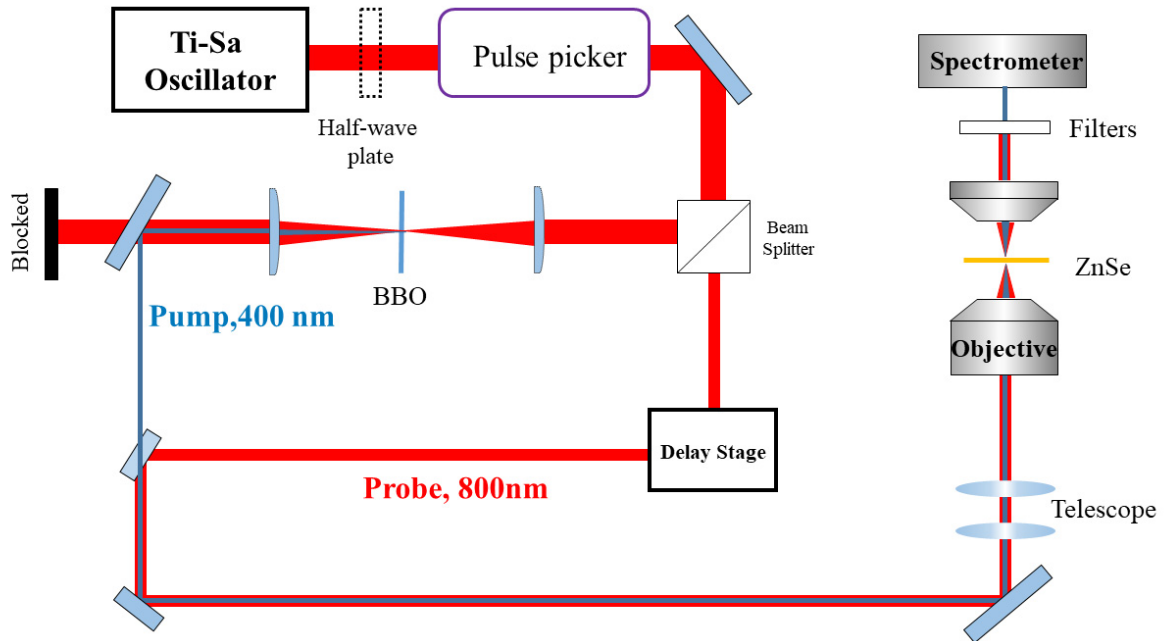


Figure 2.23: Recommended setup.

Chapter 3

Second Harmonic Generation Microscopy

At the end of the second chapter of this thesis, we discussed the possibility of extending the FROST characterization technique to high repetition rate oscillator lasers. For this experiment, an 80 MHz Ti-Sapphire oscillator was used, which is quite common for nonlinear optical microscopy such as two-photon fluorescence and second harmonic generation (SHG) [103]. Principally, the light source of a nonlinear microscopy system preferably has a high repetition rate laser which allows maintaining a low pulse energy to avoid ionization and damage in the imaged material [104]. Another important feature is the pulse duration of the input source: basically, the light source for two-photon fluorescence and SHG microscopy system is preferred to have a relatively short pulse duration, which would allow to obtain a high nonlinear signal (fluorescence and SHG) [22]. The next significant feature for the source of a SHG microscopy system is the fundamental input wavelength [75]. The source of the SHG microscopy is preferred to have an input wavelength which would ensure that the output SHG wavelength is on the edge of the autofluorescence [105]: SHG is always at half the input beam wavelength, however the broad spectrum of auto fluorescence remains unchanged (Figure 3.1). Overall, an 80 MHz Ti-Sapphire oscillator, which delivers around 150 fs pulses with a tunable wavelength, is one of the most common and robust excitation sources for two-photon fluorescence and SHG microscopy [10].

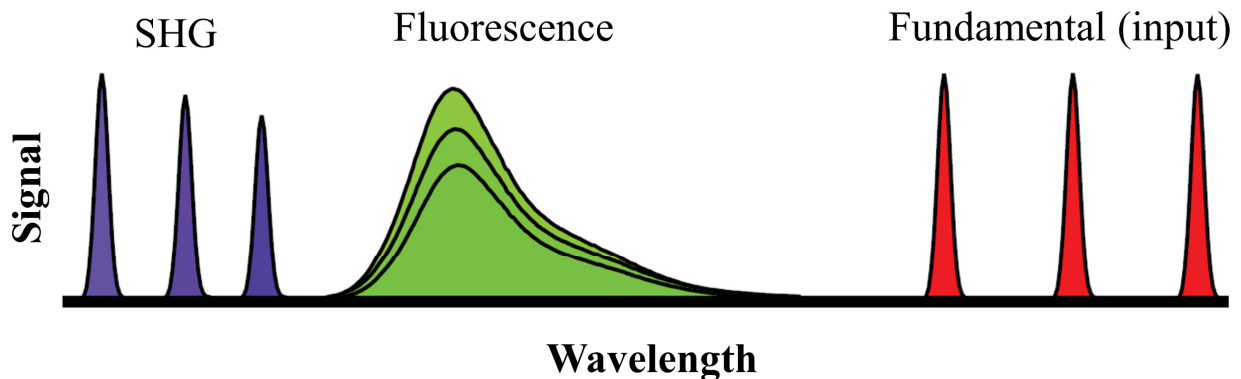


Figure 3.1: SHG and fluorescence spectra in comparison to the fundamental spectra. Changing the fundamental wavelength directly changes the SHG position ($\lambda_{\text{SHG}}=0.5 \lambda_{\text{Fundamental}}$), though the broad spectrum of fluorescence remains unchanged and is only affected in magnitude. Adapted from [103].

As mentioned earlier (section 1.2), the ultimate goal of this master thesis was to gain expertise in different aspects of nonlinear optics, and in chapter two I explained how I learned about ultrashort pulses and different approaches for their temporal characterization. For the investigation in that chapter (section 2.5, Investigation of transient gate at different repetition rate), I required a high repetition rate source which was only available in the nonlinear optical microscopy lab of INRS-EMT. Working in this lab encouraged me to get familiar with the nonlinear microscopy world. First, I started with learning about the optical aspects of this technique. Eventually, through collaboration with the team of Prof. Emanuele Orgiu, I used this

technique to investigate the possibility to modify the SH signal of TMDs by manipulating the molecular architecture. Before discussing this investigation, we will go through a brief introduction on microscopy.

3.1 Brief introduction on microscopy

In the beginning microscope was simply an instrument to magnify tiny objects [106]. The simple microscope (magnifying glass) was initially made of a single lens and it's unclear who invented it [107]. In the 1590s, *Hans and Zacharias Janssen* (lens makers) invented the compound microscope through experimenting with lens combination inside a tube. They discovered that a magnified image by a particular lens can be further magnified by using a secondary lens. This device (Figure 3.2a) delivered the possibility of two-stage magnification. However, the first compound microscopes were unsuccessful to improve the resolution which led to blurry and obscured images. Nevertheless, *Hans and Zacharias Janssen* discovery laid the significant groundwork for the development (Figure 3.2b) of optical microscopes.

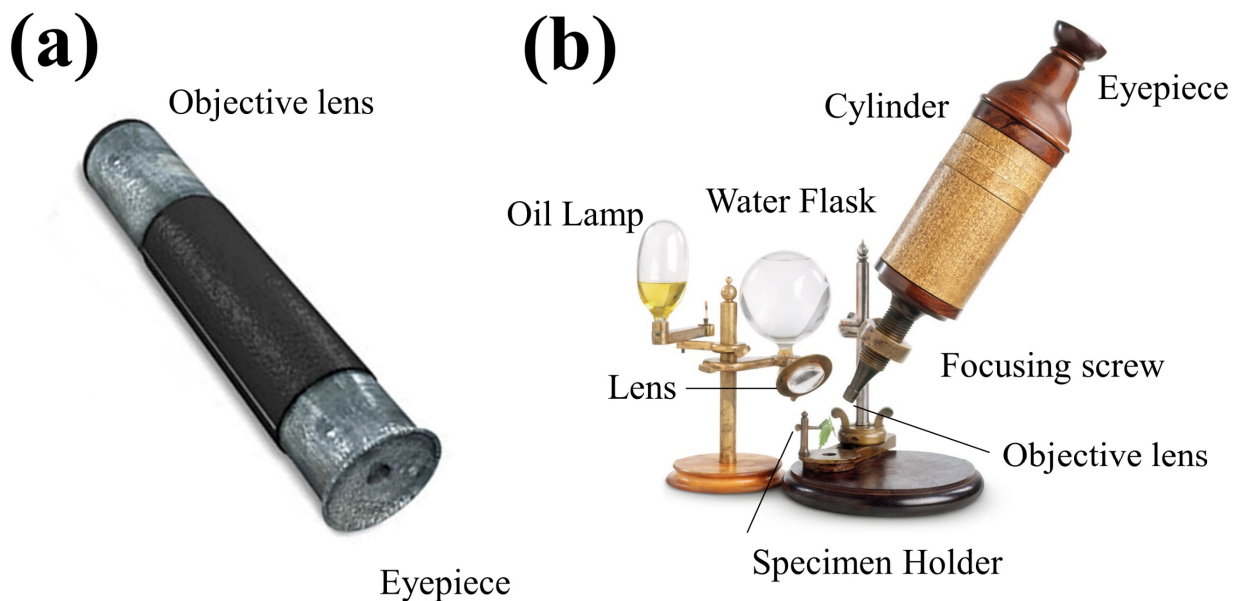


Figure 3.2: (a): The first compound microscope made by Janssen (1590's). (b): Hook's compound microscope (1665) used for discovery of cell. Adapted from [108].

Overall, many individuals were involved in improving the resolution and the contrast of optical microscopes over the years [109]. Figure 3.3 represents a few of the important early accomplishments for the development of optical microscopy.

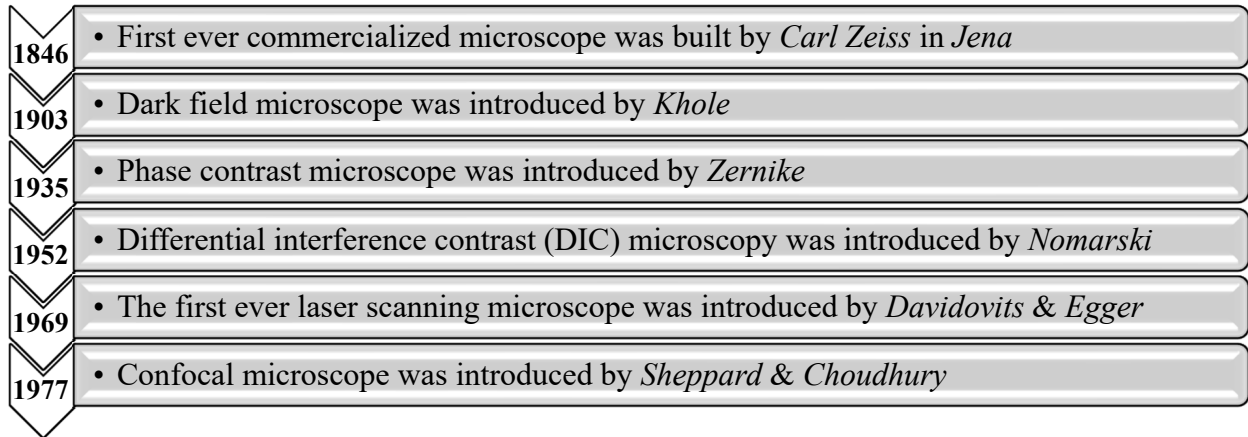


Figure 3.3: Significant early development of optical microscope thought the years [104,110–113].

Two-stage magnification in compound microscope

As mentioned, a compound microscope can be made by the association of two lenses commonly known as an objective lens and an eyepiece alongside a light source and a sample holder. The magnification part occurs in both of these stages, the objective lens creates a magnified image, and the job of the eyepiece is to view the magnified image.

$$M_{Final} = M_{Objective\ lens} \times M_{eyepiece} , \quad \text{Eq.20}$$

An objective lens creates an image of the object onto the field stop, and that creates a limitation in terms of the imaged surface area. For instance, a 4× objective lens image will have a 16-mm diameter field stop. Due to this, every objective lens has an aperture to limit the area of bundle light known as the Numerical Aperture (NA) [111]. In other words, the numerical aperture provides information about the ability of an objective lens to gather light and image it in a fixed distance [111].

In optical microscopy, light is the probe to determine the structure of objects and therefore, light wavelength is a resolution factor [75]. In any type of optical microscopy, it's crucial to know about the properties of the light source such as monochromaticity, polarization, coherency and collimation (Figure 2.2) since each and every one of these properties can affect the quality and lead to inaccurate imaging [75]. To explain better, when we are dealing with light and matter, there are various phenomena that can occur. Light can be transmitted, reflected, absorbed, diffracted. This is why the selection of the source is very crucial [75].

The introduction of the laser [77] made it possible to achieve unprecedented intensity, which not only improved the signal efficiency in linear optical microscopy techniques, but also initiated the nonlinear optical microscopy world as well [114].

3.2 Nonlinear optical microscopy

During the establishment of the theory of quantum mechanics in 1931, Maria Göppert-Mayer predicted “elementary processes with two quantum transitions” which is the equivalent of describing the phenomenon known as two-photon absorption [115,116]. Basically, this theory suggests the possibility to excite electrons to a higher level by using more than a single photon, since the electronic levels are quantified. This concept was experimentally applied only one year after the construction of the first laser [6]. In 1961 second harmonic generation (SHG) was measured for the first time in quartz (Figure 2.3), which began the experimental observation of nonlinear optics [78]. Moreover, the two-photon excited fluorescence (2PEF) in a crystal of $\text{CaF}_2:\text{Sm}^{2+}$ was also reported during this year, which experimentally endorsed Goppert-Mayer's prediction [117]. Let's start by having a closer look at the energy diagram of SHG and 2PEF in the next part.

Jablonski energy diagram of SHG and 2PEF

In the SHG process (Figure 3.4a), the photon pair's total energy is smaller than the energy band gap of the material. Thus, the bond electrons experience a momentary ($\sim 10^{-15}\text{s}$) virtual transition (no real electron energy transition) and returns to the ground state with the emission of a SHG photon. Unlike SHG, the photon pair energy of 2PEF (Figure 3.4b), is greater than the lowest energy level of the excited state. Thus, the bond electrons transit to a real energy level (real electron energy transition) through absorption of two photons. The excited electrons often experience a non-radiative vibrational energy decay ($\sim 10^{-12}\text{s}$) to the lowest excited state. After dwelling for a few nanoseconds in this state, the excited electron returns to the ground state while emitting a single photon. Unlike SHG, 2PEF has always less energy than double the frequency of the incident beam [22,118].

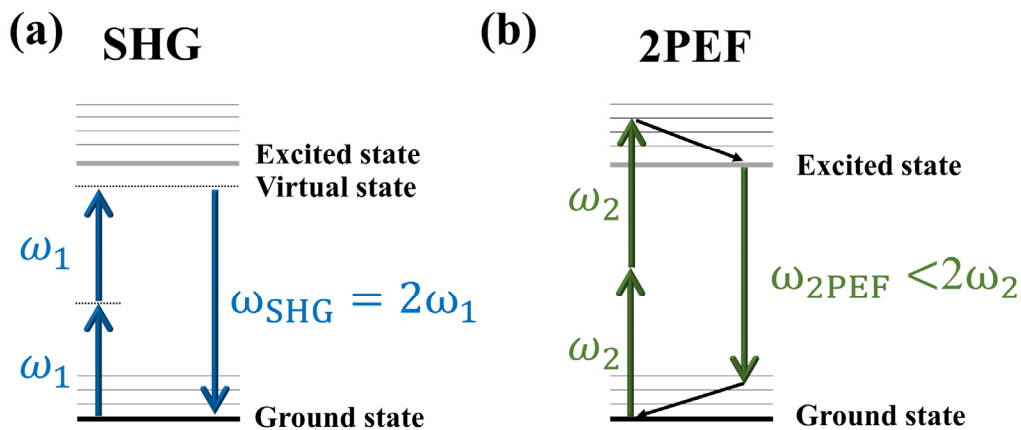


Figure 3.4: The transition energy diagram of (a): SHG and (b) 2PEF. SHG photon is emitted through a virtual transition at exactly double the incident photon energy. However, in a 2PEF a photon is emitted through real electron energy transition and always has less energy than double the incident photon energy.

Nonlinear optical microscopy

Nonlinear optical microscopy techniques (such as 2PEF and SHG microscopy) deliver several advantages including high penetration depth [119–121], intrinsic 3D imaging [122–124] and decreased photodamage to tissue samples [119–121] through using near-infrared lasers [125]. A proper way to categorize nonlinear microscopy techniques is based on the coherency of the produced signal [103]. Principally, the produced signal of incoherent nonlinear microscopy (such as 2PEF) has a random phase and the power of the signal is proportional to concentration of radiating molecules. On the other hand, the phase of coherent microscopes is rigorously arranged by a variety of aspects [41]. The common causes behind the phase of a coherent signal are excitation light phase and the geometric distribution of the radiating molecules [41]. Coherent signal power follows the square of the concentration in radiating molecules. Common known techniques of coherent nonlinear microscopy are second harmonic generation (SHG) [126] and coherent anti-Stokes Raman scattering (CARS) microscopy [127].

2PEF microscopy

The introduction of two-photon excited fluorescence (2PEF) microscopy in 1990, revolutionized the field of microscopy [103]. 2PEF is based on the simultaneous interaction of two photons with a molecule which produces an excited photon with quadratic intensity dependence to the input intensity [103]. This technique has given rise to diverse imaging applications in the field of biology: neuronal plasticity [128], calcium dynamics measurement deep in brain and live animals [129,130], neurodegenerative disease [131], etc. The effect of using longer excitation wavelengths in 2PEF is a higher penetration depth (while slightly compromising the resolution) compared to an ordinary confocal microscope system [132]. There are drawbacks in these systems as well, since absorption can lead to unwanted effects such as photo bleaching (light-induced destruction of fluorophores) [122].

3.3 SHG microscopy

In 1974, *Robert Hellwarth* and *Paul Christensen* used a SHG microscope experimental setup (they implemented SHG into an optical microscope) to observe the crystal structure of ZnSe [133]. Later, *Gannaway* and *Sheppard* applied this concept to a laser scanning microscope to acquire SHG images in various crystals [134]. In 1986, SHG microscopy was demonstrated using biological tissues as well [135].

SHG microscopy is a handy technique in the world of biology, capable of characterizing connective tissues such as skin, tendon, bones, and blood vessels as well as collagen fibers in internal organs such as liver, kidney, and lungs [35,136–150]. Since SHG is only the conversion of photons without any absorption, this allows the reduction of photo toxicity and out-of-plane photo bleaching [41]

Expression of the second order nonlinear converted field

In a dielectric medium, the macroscopic dipole moments sum (\mathbf{p}) induced by an external electric field (\mathbf{E}) is the induced polarization density (\mathbf{P}). Moreover, the optical response is classified into linear and nonlinear governed by the relationship between \mathbf{P} and \mathbf{E} . The general optical response (Eq.2) was previously described in section 2.1.2. In even-order nonlinear responses (such as SHG), the relationship between the induced dipole \mathbf{P} and excitation field (\mathbf{E}) cannot be built unless the inversion symmetry is broken. Hence the SHG is zero and forbidden for centrosymmetric materials [22].

SHG is a second order nonlinear response ($\mathbf{P}^{(2)}(\mathbf{t}) = \epsilon_0 \chi^{(2)} \tilde{\mathbf{E}}^2(\mathbf{t})$) where the full dielectric susceptibility ($\chi^{(2)}$) matrix has 27 elements [22]. It's common to represent the second order susceptibility as $\chi^{(2)} = \mathbf{2d}$ (contracted notation) and subsequently the SHG polarization density can be calculated by:

$$P(2\omega) = \epsilon_0 \chi^{(2)} \cdot E(\omega)E(\omega) \quad P(2\omega) = \epsilon_0 \mathbf{2d} \cdot E(\omega)E(\omega)$$

$$\begin{bmatrix} P_x(2\omega) \\ P_y(2\omega) \\ P_z(2\omega) \end{bmatrix} = 2\epsilon_0 \begin{bmatrix} d_{11} & d_{12} & d_{13} & d_{14} & d_{15} & d_{16} \\ d_{21} & d_{22} & d_{23} & d_{24} & d_{25} & d_{26} \\ d_{31} & d_{32} & d_{33} & d_{34} & d_{35} & d_{36} \end{bmatrix} \begin{bmatrix} E_x(\omega)^2 \\ E_y(\omega)^2 \\ E_z(\omega)^2 \\ 2E_y(\omega)E_z(\omega) \\ 2E_x(\omega)E_z(\omega) \\ 2E_x(\omega)E_y(\omega) \end{bmatrix} \quad \text{Eq.21}$$

The second order susceptibility ($\chi^{(2)}$) tensor is bulky and through the Kleinman symmetry, and certain symmetries of the material, it usually gets simplified to two or three nonzero components [151]. Polarization resolved SHG Microscopy (P-SHG) measurement can give access to the ratio of these tensor components. For instance, here in our group, the tensor matrix holding the structure information of calcium barium niobate epitaxial thin films was calculated [152] based on this concept.

Polarization resolved SHG Microscopy (P-SHG)

As mentioned, the second order susceptibility tensor holds molecular information through the orientation of the molecule and incident beam [22]. However, SHG microscopy alone is unable to uncover all this information. The combination of SHG and polarization provides information regarding the arrangement of the dipolar distribution of the sample, since there is an existing relationship between the generated SHG and the incident electric field [153]. Basically, P-SHG provides interesting information by taking advantage of the sensitivity of polarimetric methods to the molecular orientation distribution [154] and the high specificity of SHG for dense noncentrosymmetric macromolecular organizations [155–158]. P-SHG can successfully differentiate collagen types from others [159] and acquire in-plane molecular structural information [141]. To gain this information, the SH signal is examined based on the incident beam

polarization and ultimately comparing a theoretical model with the intensity angular dependency leads to extracting the mentioned molecular information [153]. However, adjusting accurately the incident polarization is critically important.

Calibration of incident polarization

Usually, the polarization of light is adjusted by the help of a half wave plate, quarter plate, and a polarizer. For accurate data, the polarization of the incident light needs to be adjusted close to the sample holder of the microscope system. Though for precise data, this is not sufficient since the optical components through the path can alter polarization. One approach to avoid this issue is to introduce the required compensation polarization before the entrance of the microscope system [160]. In this approach, with the help of an analyzer, the introduced polarization of the combination of the half wave (HW) plate and the quarter wave (QW) plate is determined. This scan is repeated for different angles of the HW and QW plates. To facilitate this procedure, software written by *Brideau* and *Stys* was used to speed up the calibration process [160]. In brief, the first step before performing a P-SHG scan is to create a calibration map including every linear and circular polarization required for this scan. In Figure 3.5 we can observe the laser polarization as a function of the HW and QW angles that I acquired for the following experiments discussed in this chapter.

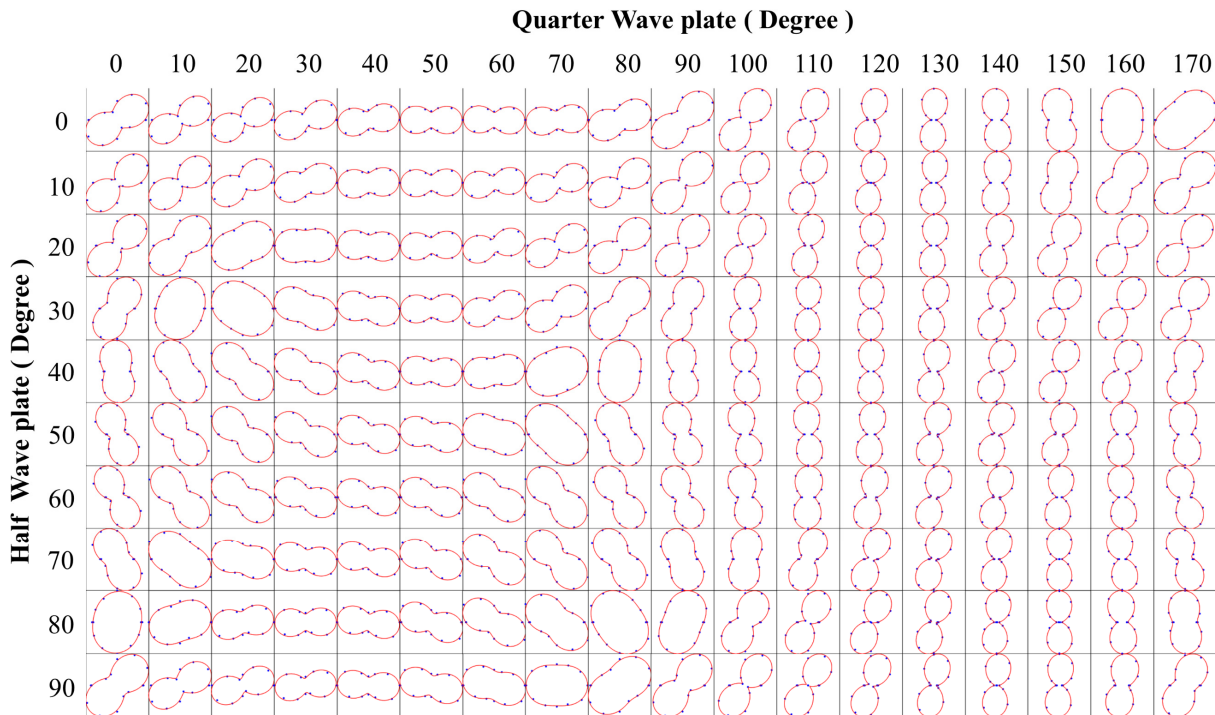


Figure 3.5: The calibration map prepared for P-SHG scan. A fully eight-shaped fit represents a linear polarization and an oval (circular) fit represents a circular polarization point.

A P-SHG calibration map represents the incident polarization of light on the sample holder. Here a circular polarization point is represented as an oval or circular fit and a fully eight shaped fit represent a linear polarization. This map creates a guiding path to avoid ellipticity while scanning different polarization angle for data accusation.

SH intensity and radiation pattern in SHG microscopy

Generally, in the plane wave approximation the SH signal intensity (for very low conversion cases such as SHG microscopy) is expressed as:

$$I_{SHG} = |A_{2\omega}|^2 = \alpha_{2\omega}^2 I_{\omega}^2 (|\chi^{(2)}|^2) (L^2) \left(\text{sinc}^2 \left(\frac{\Delta k L}{2} \right) \right) \quad \text{Eq.22}$$

where $\alpha_{2\omega} = \omega_0 / cn_{\omega}^2 n_{2\omega}$ is a constant, I_{ω}^2 is the input intensity and L is the sample interaction length.

Alongside the intensity dependency of SHG on $|\chi^{(2)}|^2$, SH intensity is also relative to the phase matching condition as well. Basically, in the case of perfect phase matching ($\Delta k = k_{2\omega} - 2k_{\omega} = 0$, Figure 3.6b) or wave-vector phase mismatch ($\Delta k \neq 0$, Figure 3.6a), the SH intensity is governed by the square of the interaction length (L) and $\text{sinc} \left(\frac{\Delta k L}{2} \right)$ term respectively.

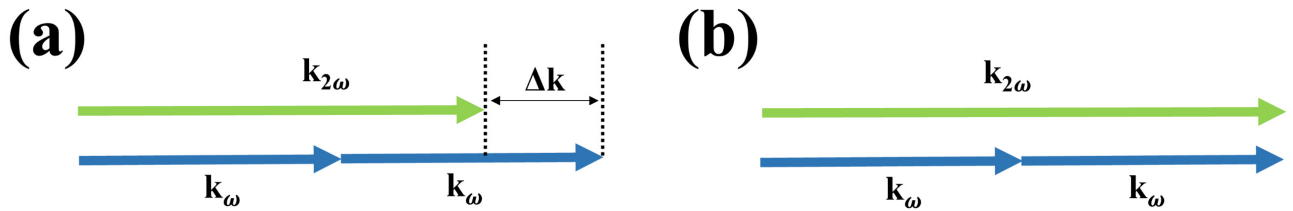


Figure 3.6:(a): Typical wave-vector mismatch in SHG. (b): Perfect phase matching in SHG. Adapted from [114].

Unlike fluorescence (Figure 3.7a) which emits signal isotropically [161], SHG results from the summation of light fields that are induced by molecular arrangement possessing ordered noncentrosymmetric structures and satisfying the phase-matching condition[114]. This leads to producing (Figure 3.7b) highly directed SHG radiation [162,163]. Basically, when the phase matching condition is completely satisfied ($\Delta k=0$, Figure 3.6b), the entire SH signal is emitted in the forward direction (Figure 3.7c, twin green lobed). This is the case with interfaces and uniaxial SHG crystals. On the other hand, this is different when dealing with biological tissues. In this case, due to the intrinsic dispersion and randomness of these samples, the phase matching can never be fully satisfied. Consequently, the SHG distribution is in both forward and backward directions [114]. As the coherence length of the backward SHG is relatively smaller than the forward SHG coherence length, the SH signal in the forward direction generally dominates (the SHG emission is formed in the shape of two lobes, Figure 3.7c). However, the forward/backward signal ratio is not fixed. Example

(i): the radiation pattern of the SHG in a small scatterers area (like one collagen fibril) is highly dependent on the scatterers orientation: depending to the angle of the fibrils (Figure 3.7b), the forward SHG can dominate or be equal to the backward SHG [156]. Example (ii): In thick muscle fiber tissues, the forward SHG extremely dominates. However, when the interaction length is less than $\lambda_{2\omega}/2\pi \approx 100\text{nm}$, quasi-phase matching (QPM) is satisfied and SHG is generated partially in both forward and backward directions [162,164].

In Figure 3.7c (blue pattern) alongside the SHG radiation pattern, we can observe the THG (third-harmonic generation) radiation pattern as well. THG is considered to be a volumetric process which is not limited to the requirement of inversion symmetry breaking. In THG, alongside the twin lobe behavior (surface generation), there is conical shape pattern (volumetric generation) [165]. More importantly, SHG also appears and is highly used in volumetric media as well. In volumetric media, SHG is dominated by the noncentrosymmetry of the scatterers (due to molecule properties, arrangement and crystal structure) and the SHG radiation pattern is greatly affected by the focal spot depth on the sample [166,167]. This can lead to a volumetric conical shape radiation (such as in the THG case in Figure 3.7c) [168]. Furthermore, the fundamental wavelength is also highly effective on the backward SHG generation [169].

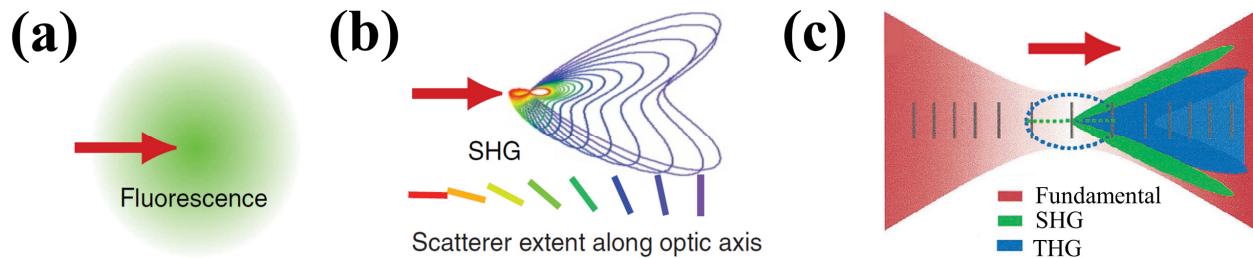


Figure 3.7: (a) Fluorescence has isotropic emission. However (b) SHG directionality is based on the orientation and distribution of the nonlinear dipoles. Extracted from [97]. (c): The SHG and THG radiation patterns in tightly focus microscopy. Extracted from [166]. Backward generation is not shown to simplify the understanding.

In the end, backward detection is a significant feature in SHG microscopy. The SHG backward detection feature provides important information on the spatial distribution of tissue samples with quasi phase matching condition: in this condition the SH signal is quasi-coherent and the distribution pattern is governed by the spatial distribution. To further explain, we need a combination of both forward and backward SHG for the complete comprehension of the spatial distribution [162,164]. Additionally, the SHG backward detection is a true asset when dealing with materials (or samples) that limit forward detection for reasons such as thickness and lack of transmission. Figure 3.8 shows an example of forward and backward SHG detection, using our SHG microscopy system on MoSe₂. In the following section, we will discuss some of the technical aspect in our SHG microscope system.

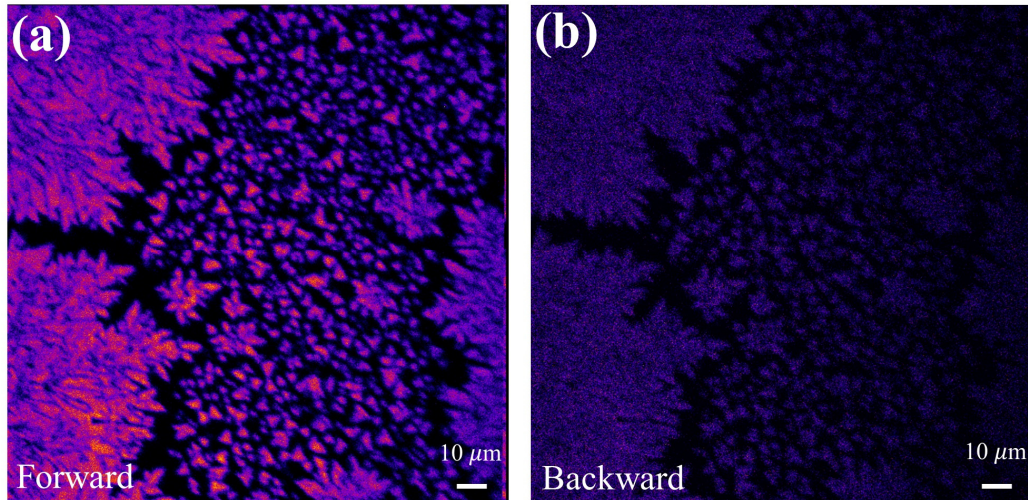


Figure 3.8: SHG microscopy image of MoSe₂ in forward (transmission) and backward (reflection) directions. The SH signal dominates in the forward direction, though backward generation is a real asset, especially when there are limitations in forward detection. Sample was provided by Franz J. F. Löchner, Institute of Applied Physics, Abbe Center of Photonics, Friedrich Schiller University Jena.

3.4 Technical overview of our SHG Microscopy system

Laser source

Here in our group, we use an 80 MHz Ti-Sapphire oscillator as the source of our customized multiphoton microscope. In this system, the output pulse is precisely phased locked either internally or externally by the help of a 3930 Lok-to-Clock system. The repetition rate of this source is set by the factory at 80 MHz and this high repetition rate would produce a low amount of energy per pulse which would avoid ionization and damage in the imaged material. As mentioned at the beginning of this chapter, the wavelength of the SHG microscopy system input source should preferably be chosen in a way to ensure that the SHG wavelength is on the edge of autofluorescence (Figure 3.1) [105]. This is quite significant since we can avoid absorption while maintaining considerable penetration depth [170]. For the following experiments discussed in this chapter our Ti-Sapphire oscillator was mode locked at 810 nm (15 nm bandwidth) producing 150 fs ultrashort pulses.

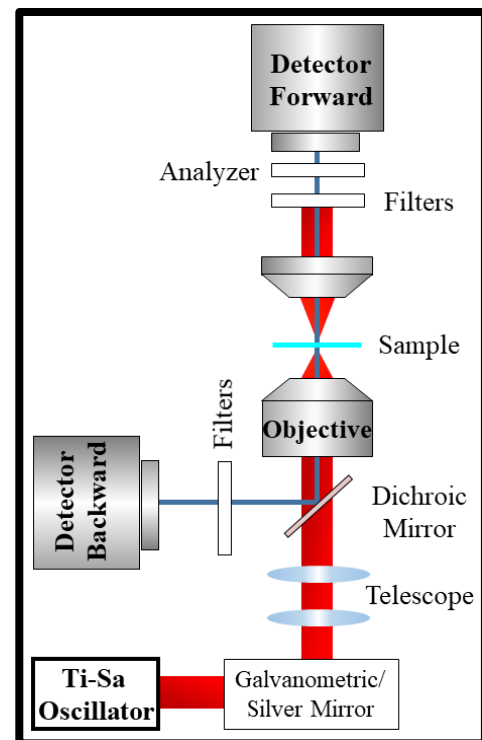


Figure 3.9: Multiphoton Microscope Setup

Microscope System

The customized microscopic system (Figure 3.9) used for the experiments discussed in this chapter has an inverted orientation. The usage of these microscopes are growing rapidly since the inverted stage is more accessible and has a more stable center of mass which would make it more resistant to vibration [75]. There are some downsides with these types of microscopes, for instance, the objective lens can relevantly face a higher chance of getting damaged in this setup.

Here in our system, there are two separate paths to emit the light inside the microscope, first it uses a combination of galvanometric mirrors which allow the system to scan a small area of a sample at high speed. In this method, the focused beam scans laterally across the specimen surface in a rectangular pattern (known as raster scan) by the combination of the two high-speed galvanometric mirrors [171].

The second path uses a simple silver mirror and scans the sample by moving the stage in a pattern [172]. In other words, in the first method the stage is fixed and the input beam is scanning and in the second method, the beam is fixed and the stage is moved to perform the scan. The stage scanning method is preferred for scanning a large area. In this method it's important to enlarge the size of the beam to fully benefit from the high NA [173]. In either of these approaches, the incident beam is tightly focused on a sample by an objective lens (20x,0.75NA, Olympus) and after that, the propagated signal is collected by a condenser and sent toward the detector.

Beam Intensity control

Inside of the microscope, the intensity of the beam can be reduced by the help of natural density filters, which basically moderate the intensity of all wavelengths [75]. Moreover, since the signal intensity in SHG is inversely proportional to the pulse temporal duration, the dispersion of the pulse is controlled by pre-chirping outside of the microscope with the help of a pair of chirped mirrors. The proposed technique in section 2.5.1 could ease the process of characterizing the exact chirp of the pulse directly at the sample holder. This information can be used to compress the pulse which would permit higher SH signal.

Data acquisition

Generally, based on the specific type and application of the multiphoton microscopy, the desired response of light and sample should be collected. The desired response can be based on isolating a specific range of wavelengths or polarizations. To isolate specific wavelengths, we usually use a mixture of band-pass filters and edge filters. Edge filters can be classified into two categories: long pass filters block the short wavelengths, and short pass filters transmit the short wavelengths. On the other hand, band-pass filters block both up and down the desired wavelength, and are generally only suitable for specific purposes [75].

The SHG which is the frequency doubling of the fundamental differs itself from the fundamental so that one can filter the signal out of the excitation easily. Basically, here for our SHG microscopy measurement, the SH signal at a central wavelength of 405 nm is distinguished from fundamental at 810 nm by the use of two low-pass filters (FF01-720/SP-25, Semrock) and a narrow band-pass filter (FF01-405/10, Semrock). In the end, the output of a microscope is an image which is the representation of the emitted signal to the detector. This is why proper filtration is of great importance when dealing with microscopy. In the end, the distinguished signal is amplified with the help of a photomultiplier tube (PMT, R6357, Hamamatsu) with adjustable gain control.

3.5 Illustration of using SHG microscopy to evaluate noncentrosymmetry

In general, the second order nonlinear interaction only occurs into crystalline media with no symmetry at the atomic scale (non-centrosymmetric/ break of inversion symmetry) [22]. Common examples of non-centrosymmetric materials are piezoelectrics [30] and ferroelectrics [31]. SHG is sensitive to any point symmetry violation in the material, and implementing this concept inside a microscopic system creates a powerful measurement technique to analyze the symmetry properties of crystals.

Here in this section, we briefly discuss the data that I acquired as a complementary set of measurements to verify the inversion symmetry break of SrTiO₃ thin films. These films were provided by the team of Prof. Andreas Ruediger in the context of a collaboration. The complete details of the project are outside the scope of this thesis, and this section is mainly an illustration of using SHG microscopy to evaluate noncentrosymmetry in a material.

Brief introduction on the project

Perovskites are a very important class of materials that have suitable properties for a number of applications (electro-optical) since they show a wide range of properties like piezoelectricity, ferroelectricity and pyroelectricity [174–178]. The members of the perovskite family are easily distinguishable since they all follow the general formula of ABO₃ [179].

Bulk Strontium Titanate (SrTiO₃) is a perovskite with a centrosymmetric structure. This material, at cold temperature even in bulk, displays many anomalies that suggest its proximity to a ferroelectric material, including a large rise in the dielectric constant. Besides temperature, previous studies showed that the centrosymmetric behavior of this material can be broken due to external actions such as nanoindentation [180,181].

Theoretical and experimental data suggest that when the size of strontium titanate enters the nanoscale world, this material demonstrates new physical properties associated with symmetry breaking [182]. The main goal of this project was to learn about the unknown nature of these symmetry breaks breaking using tip-enhanced Raman spectroscopy. This work was performed by the group of Prof. Ruediger (Azza Hadj Youssef, Clarick Jiawei Zhang, et al.). Additionally, SHG microscopy was used as a complementary analysis tool to verify inversion symmetry breaking. Here, we will only discuss complementary measurements by SHG microscopy.

Evaluation of inversion symmetry by SHG microscopy.

In this study, there was a learning phase to acquire the ability to grow strained Strontium Titanate nanoislands thin film with a break in inversion symmetry. Unfortunately, our initial measurements using SHG microscopy system (the setup describe in section 3.4) were free of any significant SH signal. Later, by optimization, the collaborator was able to prepare SrTiO₃ thin films with relatively greater SHG active areas. Figure 3.10 represents the distribution of signal over a large area of a sample by stage scanning.

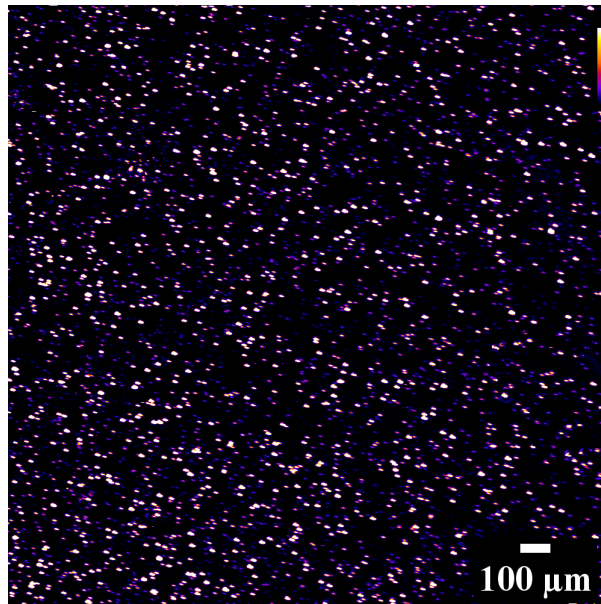


Figure 3.10: A 2000×2000um SHG microscopy image of SrTiO₃ nanoislands.

Here, our filtration was only able to detect a small range of wavelengths (400-410 nm) centered at exactly half of the fundamental wavelength (810 nm). However, this is not sufficient and only capturing a single image cannot certify the nature of this signal (auto fluorescence spectra is broadband and may overlap with SHG spectra, Figure 3.1).

The differences between fluorescence and second harmonic signals can be evaluated only on the basis of their behavior. Firstly, SHG is a nonlinear response which must follow the nonlinear nature of harmonic

generation. SHG depends on the square of the excitation laser intensity (Eq.22). To evaluate this behavior, a scan (Figure 3.11) was conducted in terms of the fundamental power at fixed polarization vs. the produced SH signal. To ensure the quality of the data, for each individual point, 5 images were captured and the data represents the average of them. Overall, the steady increase of the square root of the signal intensity as a function of the power of the fundamental wavelength is in good agreement with the quadratic nature of the harmonic signals [22].

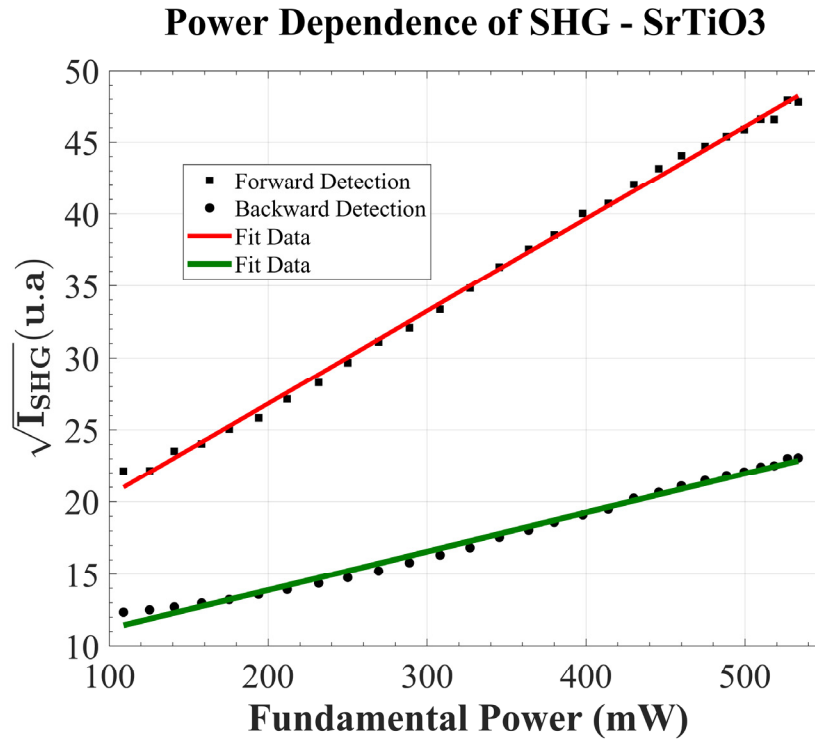


Figure 3.11: SH signal of SrTiO₃ vs. the fundamental power at fixed polarization.

To further distinguish the fluorescence signal from the second harmonic signal, we investigated the signal response in terms of the fundamental incident polarization. Basically, fluorescence power scales as the number of radiating molecules and is independent of the incident polarization. In addition, the phase of the harmonics signal is tightly matched to the fundamental incident light (Figure 3.7). Consequently, the SH signal is significantly subjected to both the orientation of the molecules and fundamental incident polarization [166]. To evaluate this behavior, a scan (Figure 3.12) was conducted as a function of the fundamental polarization at fixed input power. The incident polarization was controlled with the combination of a half wave plate and quarter-wave plate based on the prepared calibration map (Figure 3.5).

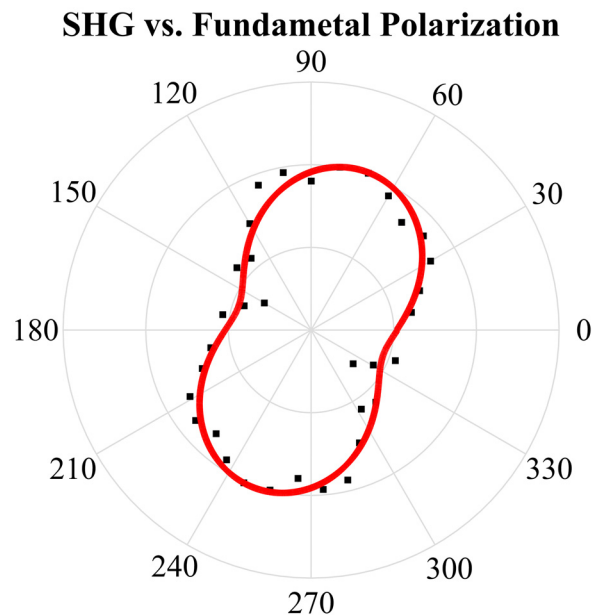


Figure 3.12: SH signal of SrTiO₃ vs. the fundamental polarization.

Overall, the extracted information from Figure 3.11 and Figure 3.12 supports the SHG nature of the signal since it follows the expected intensity power law and is subject to the incident polarization. As mentioned at the beginning of this section, here we illustrated the method to confirm the break of inversion symmetry with the help of SHG microscopy. For this illustration, we used strained Strontium Titanate thin films which shows a break in inversion symmetry without outside influence from nanoindentations and temperature. This fact was demonstrated with the help of SHG microscopy, and the collaborator used tip-enhanced Raman spectroscopy to study the nature of this broken symmetry [183] (Manuscript accepted for publication). Ultimately, this data verifies that the break of inversion symmetry observed by the Raman effect (collaborator).

3.6 Molecular architecture to tune SHG from TMDs

In the previous section, we discussed an approach to recognize the fundamental nature of the SH signal. Here we will go through an experiment to modify the SH signal of TMDs by manipulating the molecular architecture. Alteration of the generated SH signal of TMDs with the help of an electrical gate over the sample has been previously demonstrated by other groups [45,184,185] and here our goal is to alternate and enhance the SH signal by using only an additional molecular layer instead of the electrical gate. This experiment was proposed by the group of Prof. Emanuel Orgiu. Dr. Atiye Pezeshki was responsible for the groundwork involving the preparation of the molecular architecture of TMDs and I have performed SHG measurements and analysis.

3.6.1 Introduction

(i) Two-dimensional materials

Two-dimensional materials (2DMs) refer to a highly interesting family of materials with only a single or few layers of atoms [186]. The most commonly known member of this family graphene, was discovered in 2004 [187] and since then, this type of material has been extensively studied [188–192]. In this family, planes covalently bridged crystalline networks of atoms are clasped together by out-of-plane interlayer van der Waals (vdW) interactions.

Molybdenum ditelluride (MoTe_2), Molybdenum disulphide (MoS_2) and Tungsten diselenide (WSe_2) belong to the transition metal dichalcogenides (TMDs) which is a big part of the 2DMs family [193]. TMDs follow the general formula MX_2 where M represents the transition metal atom (Molybdenum or Tungsten) and X represents chalcogen atom (Tellurium, Sulfur or Selenium) [194]. TMDs cover the whole electrical conductivity spectrum (from insulator, semiconductors to metals) [195] which supports the possibility of making ultra-thin low power transistors [196]. Members of this family are composed of three atomic planes and their hexagonal lattice has three-fold symmetry which can supports the inversion symmetry. TMDs have inter-band transitions, which follow the selection rule arising from inversion symmetry breaking. TMD monolayers represent a promising platform to explore spin and valley physics with the corresponding possible applications. Furthermore, the TMD family gained a huge amount of interest since they have strong optoelectronic properties, tunable excitons and strong bonds [184,197,198].

Depending to the odd or even number of layers in TMDs (Figure 3.13), the inversion symmetry of these materials may be broken which gives rise to the possibility of generating a second harmonic signal from them. To explain further, in TMDs (with a hexagonal phase- 2H) the inversion symmetry breaks in structures with odd number of layers which results in significant SHG in structures with odd layers. In contrast, there is a negligible SHG in structures with even layers since the inversion symmetry is not broken [193,199–201]. However, the mentioned trend is inverse for TMDs in 1T' (monoclinic phase) form [202]. It's noteworthy to mention that a negligible SHG may be observed when the inversion symmetry is not broken which is caused by surface effects of the material [194].

Generally, in TMDs, increment of the number of layers results in a gradual decrease of SH intensity (Figure 3.13a-c). This is caused by the increase in the absorption of SHG photon [203]. In contrast, for MoTe_2 (Figure 3.13d), the SH intensity tends to increase with the number of layers and then decreases. This is caused by the direct to indirect bandgap transition of MoTe_2 when there are more than 5 layers [204].

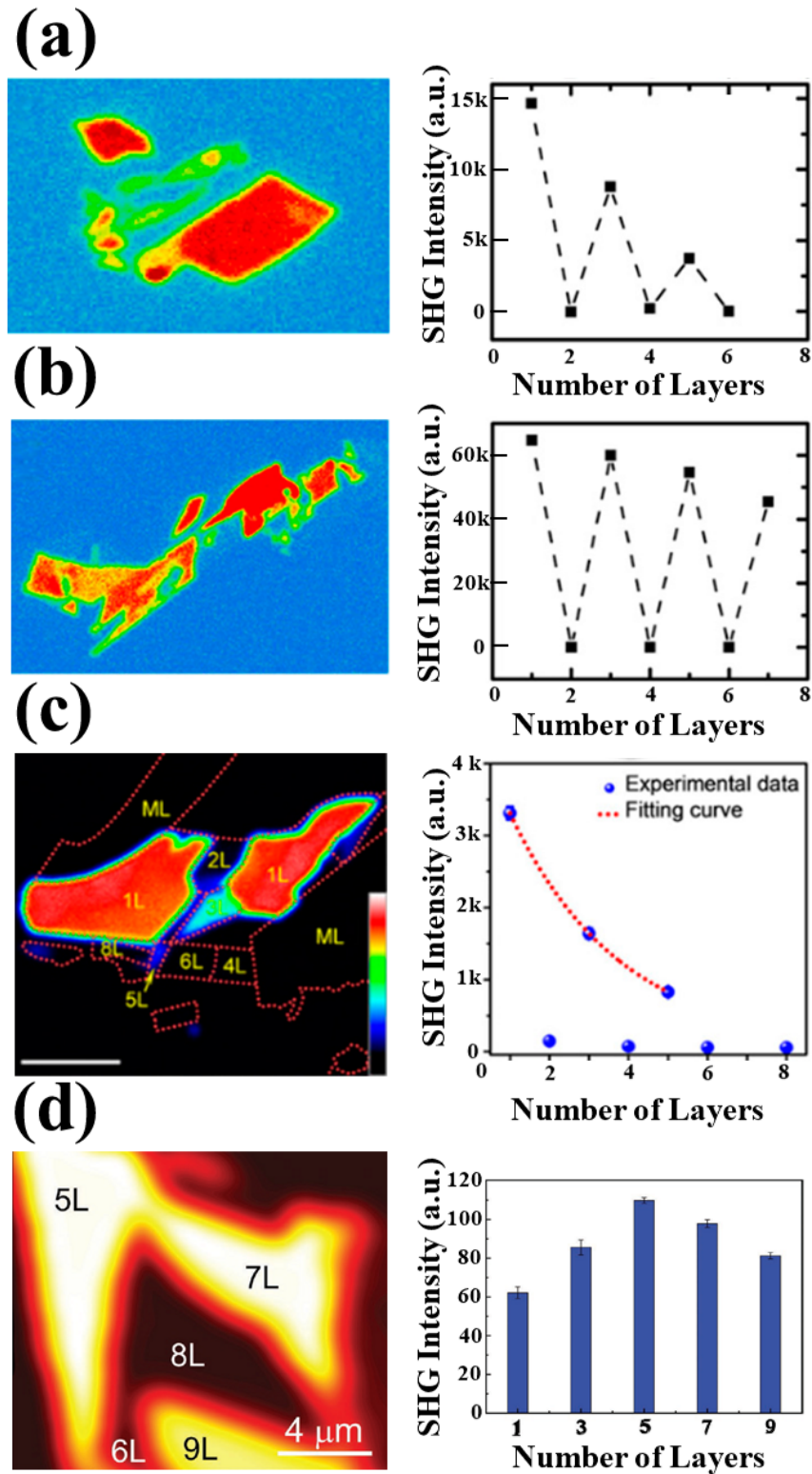


Figure 3.13: The SH intensity of TMDs is highly dependent on the number of layers. The SH image of the following TMDs is shown on the left and the SH intensity as a function of the number of layers is shown on the right. (a): WS₂ and (b): WSe₂ taken from [205]. (c): MoS₂ extracted from [206]. (d): MoTe₂ extracted from [204]. The concept of figure is adapted from [194].

(ii) Electrical control of SH signal in TMDs

The idea of joining electronics with optics is widely used for optical switching [207]. This concept is widely used in linear optics to control material properties such as absorption or refractive index. Extending this concept to nonlinear optics offers additional freedom to control properties. This concept was first demonstrated in 1962 by controlling SH signal produced from calcite using an applied dc electric field [7]. Basically, the electric field would break the inversion symmetry of the material and this concept has been extended to various applications.

As mentioned earlier, TMDs have tunable excitons (exciton: an electron-hole pair bound by Coulomb interaction which is an elementary excitation in solids), and a recent approach to control the SH intensity of TMDs is based on tunable electrical doping of the exciton charges: see the device represented in Figure 3.14a. In this concept, an electric field is used to control the neutral and charged excitons in two-dimensional semiconductors: the exciton resonance decreases with increased electron doping [45].

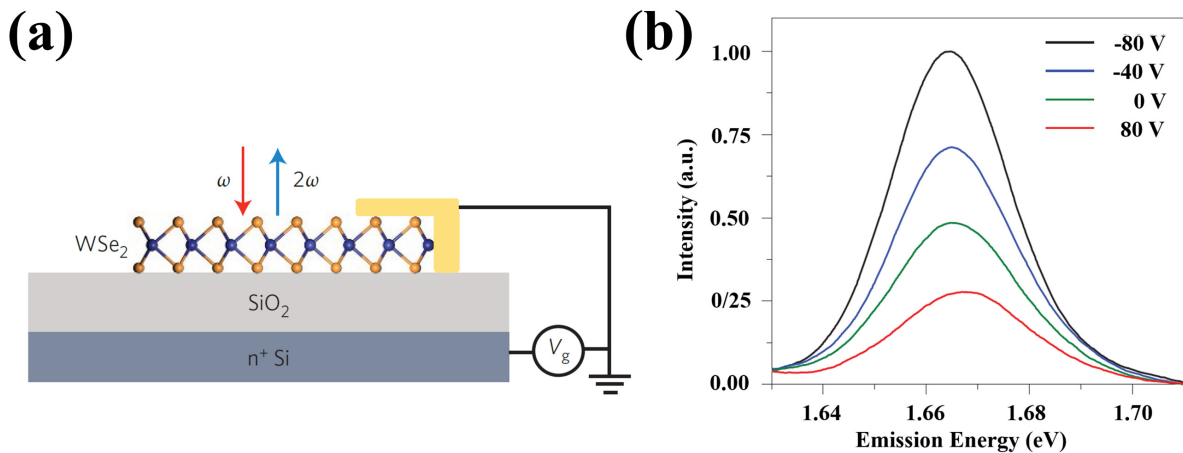


Figure 3.14: (a): Gated monolayer WSe2 (TMD) to tune the SH signal. (b): SHG spectra on resonance with the exciton at selected gate voltages. The tunability origins can be understood by the formation of positive and negative trions at high carrier density. Extracted from [45].

In Figure 3.14b, the successful control of the SH signal by electrostatic doping can be observed. As mentioned earlier, the key feature is the tunability of the exciton charging effects, which basically acts as a transitional state for photon scattering process [45].

Here the electrostatic doping affects the transitional eigen-energy spectrum due to Coulomb interactions between carriers. This phenomenon can be classified into three main situations. The first state is the electrostatic nondoping which involves only neutral excitons. The next state is the large electrostatic doping, which forces an electron-hole pair to gain an extra carrier, creating trions (charged excitons). In the last case, the doping is in a moderate stage which would permit the coexistence of trions and excitons, and tuning

the doping would shift the stage toward one of them. The maximum SH signal was reported for the last case [45].

Electrostatic doping (combined with manipulation of the electron population) has also been reported to successfully shift from the hexagonal phase to the monoclinic phase of a monolayer MoTe_2 while preserving the original hexagonal crystal orientation [185]. In this work, the electrons introduced into a monolayer 2H-phase MoTe_2 will occupy the lowest available energy level in the conduction band (this energy level is higher in 1T' phase than 2H). Injecting enough electrons (through extreme doping) into this energy level in the 2H phase is expected to induce a structural phase transition by changing the ground state from 2H to 1T'[208]. In addition to the classic solid gate (Figure 3.14a), an ionic liquid (DEME-TFSI) field-effect transistor (Figure 3.15a) was used which is capable of improving doping by one order of magnitude through electron population manipulation [209]. As explained earlier, the inversion symmetry break in TMDs is layer and phase dependent (2H: inversion symmetry breaks in odd layers, and 1T': inversion symmetry breaks in even layers). The inversion symmetry of a monolayer (odd number of layers) of 2H MoTe_2 is broken and a SH signal is detected from the sample (Figure 3.15e). Through electrostatic doping the SH intensity of the MoTe_2 monolayer was increased (Figure 3.15b) and then disappeared completely (Figure 3.15f) after transition into complete 1T' phase (inversion symmetry is not broken for 1T' phase in odd layers).

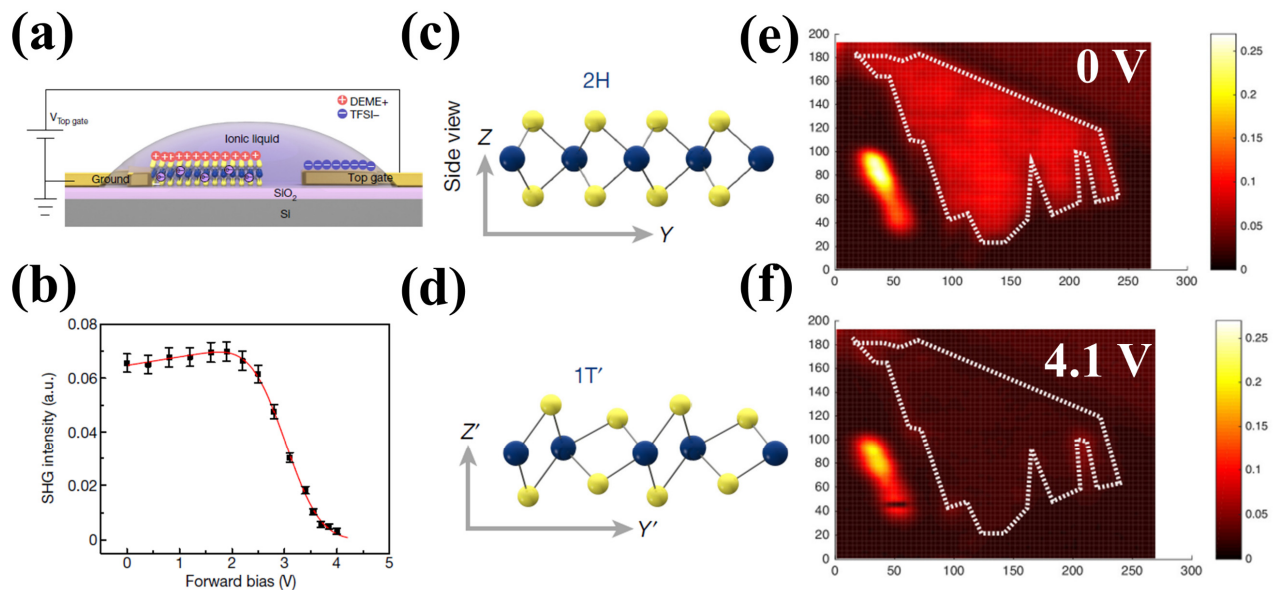


Figure 3.15: (a): Gated monolayer of MoTe_2 combined with a drop of ionic liquid which is capable of manipulating electron population and inducing a phase transition. (b): SH intensity vs. gate voltage. The crystal structure of monolayer of MoTe_2 is represented in (c) 2H phase. and (d) 1T' phase. (e): SHG microscopy image of 2H monolayer of MoTe_2 at 0 V gate. (f): SHG microscopy image of the original 2H monolayer of MoTe_2 at 4.1 V gate which induces a phase transition into 1T'. Adapted from [185].

In the above we have reported two successful demonstrations (by other groups) of SHG tuning of a TMD device by electrical doping [45,185]. In the following section we will go through our own investigation to enhance SHG of TMDs with molecular architecture.

(iii) Hybrid van der Waals heterostructure

The idea of using members of 2DMs family as building blocks (Figure 3.16) to assemble vertically stacked structures (known as van der Waals heterostructures (vdWHs)) is highly studied in the research community [210–217]. Basically, the individual sheets of 2DMs are combined to form a block of superposed planes [51,218]. This leads to obtaining complex structures, whose electronic [219–222], optical [223,224] and magnetic [225–227] properties can be greatly different from the isolated 2DMs.

Yet, the estimated available members of 2DMs are only around a few hundred [228]. However, addition of molecules (a continuous 2D molecular layer) to a 2DM family block would widen the range and potential properties of this family by a big factor. There are an unlimited number of degrees of freedom (Figure 3.17) in molecular design synthesis [229–231] which can change the block's properties. This concept consists in using the artificial architecture of 2D materials to activate specific atomic/molecule properties, and the final properties of the blocks can be selected by careful molecular design. Ultimately, the integration of a crystalline molecular monolayer inside a multilayered van der Waals heterostructure (vdWH) forms a new type of assembly known as hybrid vdWH [232–239].

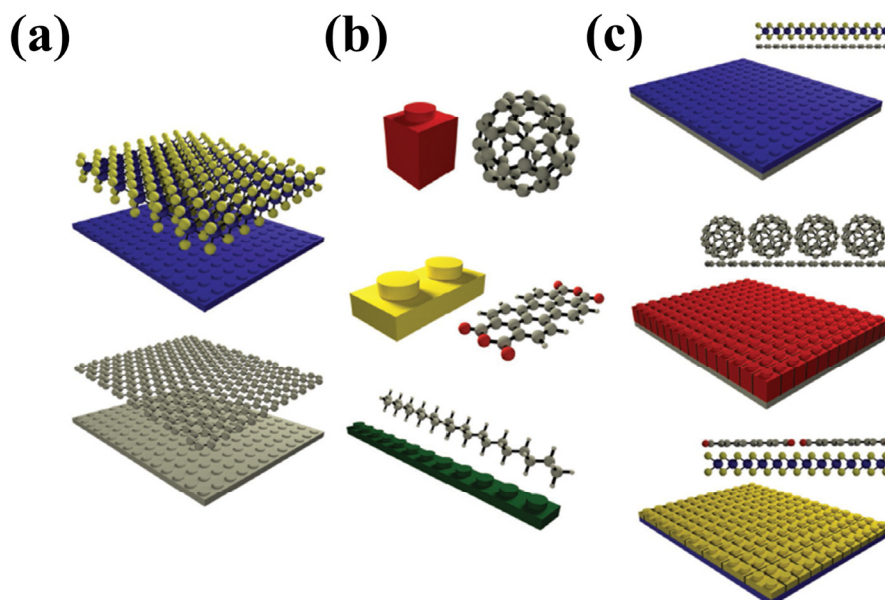


Figure 3.16: The integration of molecular layers into 2DM building blocks widens the range of potential properties. Molecular layers associated with the freedom of (a): shape, (b): class of materials and (c): thickness. Extracted from [51].

3.6.2 Controlling SHG through molecular architecture in TMDs

This experiment was designed to evaluate the possibility of using molecular layers to control the SH signal from TMDs. To understand the magnitude of it, the SHG emission of few TMDs were compared with and without the additional molecular layer (deposited by spin coating). During this study, the samples without an additional molecular layer (continuous 2D molecular layer) are referred as the original samples (TMD) and the sample with an additional molecular layer is referred as the hybrid TMD (or molecular architected TMD).

Here in this experiment, the TMD samples are deposited on a silicon wafer (Si/SiO₂) substrate. However, silicon has strong absorption below 1 μm [240]. As earlier mentioned, the thickness and lack of transmission of the samples can cause limitation in traditional forward SHG measurement (Figure 3.8). Therefore, we only use backward SHG for the upcoming measurements reported in this section.

Investigation of SHG enhancement through molecular architecture in MoTe₂

A technique based on mechanically exfoliating [241] the material onto a silicon dioxide (SiO₂/Si) substrate was used for the preparation of MoTe₂ by the summer intern student (Jean-Francois Martin) in the group of Prof. Emanuel Orgiu. The prepared samples (Figure 3.17) were usually made of a number of MoTe₂ flakes with different sizes and number of layers. As I previously mentioned in section 3.6.10, the inversion symmetry of TMDs may be broken depending on the number of layers and phase (Figure 3.13). Since SHG vanishes in the case of the inversion symmetry, the exact number of layers of the prepared TMD flakes were identified using an atomic force microscope (AFM) system [188]. Finally, among the formed flakes, an optical microscope was used to select the flakes with the appropriate number of layers and size as a reference.

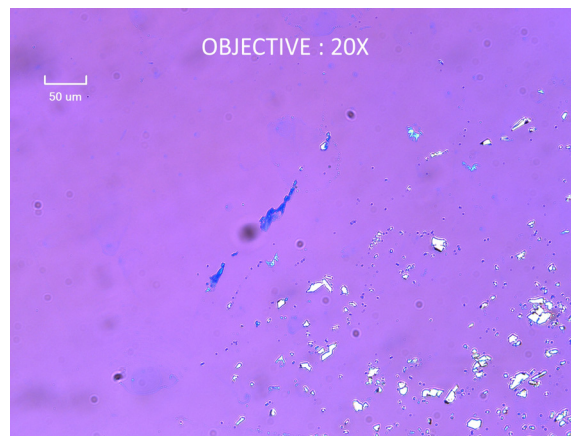


Figure 3.17: The formed MoTe₂ flakes using mechanically exfoliating. This figure was provided by Dr. Atiye Pezeshki using an optical microscope.

After selecting the desired flake, we used our nonlinear optical microscope (Figure 3.9) to evaluate the SHG enhancement. Our objective in this measurement was to analyze the SHG produced by a single TMD flake, and then compare it with this same flake after depositing an additional molecular layer (hybrid TMD) on it. In this measurement, we used a Ti-Sapphire oscillator laser with a central wavelength at 810 nm and a 150 fs pulse duration.

At first sight, finding the SH signal of the flakes using SHG microscope system was exceptionally hard. Basically, the flakes of interest were relatively small (1 - 30 μm), distributed randomly on the surface, and they produced an extremely weak SH signal (Figure 3.18). Locating the exact same flake after deposition of a molecular layer is nearly as hard as finding a needle inside a football court. In summary, we had two issues. First, the incapability to locate the same flake for repeated measurements. Next, the SH signal from any MoTe_2 flake was insufficient (near noise level) and it only appeared at the damage threshold of the flake. Our attempts to look for appropriate MoTe_2 flakes with sufficient SH signal included considering different phases (1T', 2H) with different appropriate number of layers, but we still suffered from the extreme weak SH signal near our detection noise level.

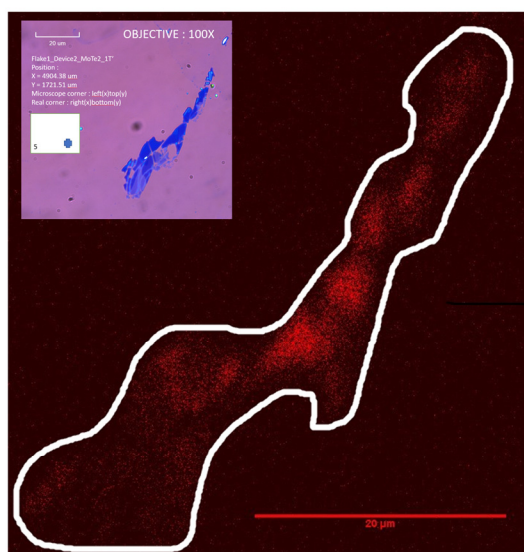


Figure 3.18: SHG image of a MoTe_2 flake. The signal is extremely weak and close to noise level, even at the damage threshold of the sample. The small pink box presents the optical image of the same flake.

To resolve the first issue, a small silver layer was coated around the desired flake: The silver layer acted as a reflecting mirror to guide the fundamental beam toward the backward detector, and by removing the SHG filters on the path were able to obtain an optical image the sample. Since the field of view of our objective lens was too small, the sample has been imaged with stage scanning in a large area. In this approach the coated silver layer around the flake was easily distinguishable (Figure 3.19) which significantly aided finding the flake of interest for repeated measurement.

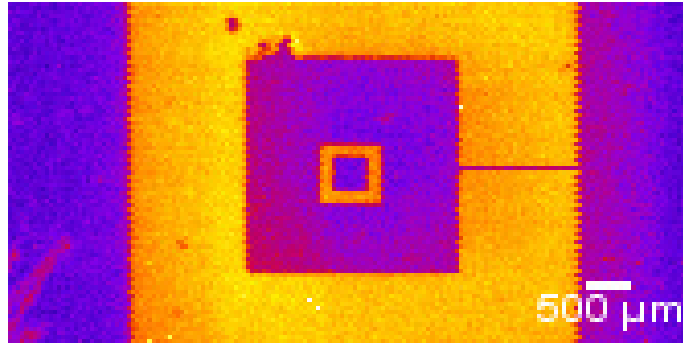


Figure 3.19: Using the reflection of the fundamental beam from silver coat to locate the single flake of interest in different rounds of measurements. The flake is located inside the smaller square.

As mentioned, using MoTe_2 as the TMD layer reference of our investigation introduced a few undesirable difficulties (such as extremely low SH signal). As mentioned earlier, the laser source wavelength of our SHG microscopy system, (Figure 3.9) is centered at 810 nm. However, this wavelength was not suitable for this experiment, since the photoluminescence emission and more importantly the excitonic absorption of MoTe_2 is positioned in the early edge of near-infrared [242]. Ultimately, the SH signal generated from the flake was too weak (Figure 3.18) to be used as a reference for this investigation.

Principally, avoiding this region of spectrum should improve the SH signal. But our only other physically available laser in that laboratory was a solid-state laser Nd:YVO_4 (Vanguard, Spectra-Physics) oscillator with a central wavelength of 1064 nm (this source is used for CARS microscopy in the laboratory). However, the temporal pulse duration of this laser is in the picosecond range which would lead to relatively inefficient generation of nonlinear optical phenomena. In summary, using this source would avoid the excitonic absorption of MoTe_2 (advantage) though SHG is not that efficient since the input optical pulse is much longer (disadvantage). At this stage, we were highly invested to continue the experiment with MoTe_2 and we proceeded to use the long pulse source (1064nm). In the end, the advantage of using Nd:YVO_4 laser outweigh the disadvantage and were finally able to proceed with our investigation: the detected SH signal improved adequately to be beyond the noise level.

Figure 3.20 represents the SH signal of the MoTe_2 flake vs. the fundamental power while keeping the input polarization fixed. The SH signal (Eq.22) is proportional to the square of the intensity and $|\chi^{(2)}|^2$. Therefore, as a function of the average power, we are expecting that the square root of the signal is a linear function. The difference is the slope comes from structure that generates the SH and this is proportional to $|\chi^{(2)}|$ thus explaining that the slope is changing for different material structures: the evaluation of SHG enhancement is based on comparing the slope of the scans. Here it's clear that the scan performed on the hybrid TMD has a relatively lower slope value compared to that of the original flake. and the result does not support any enhancement of SHG from the hybrid TMD.

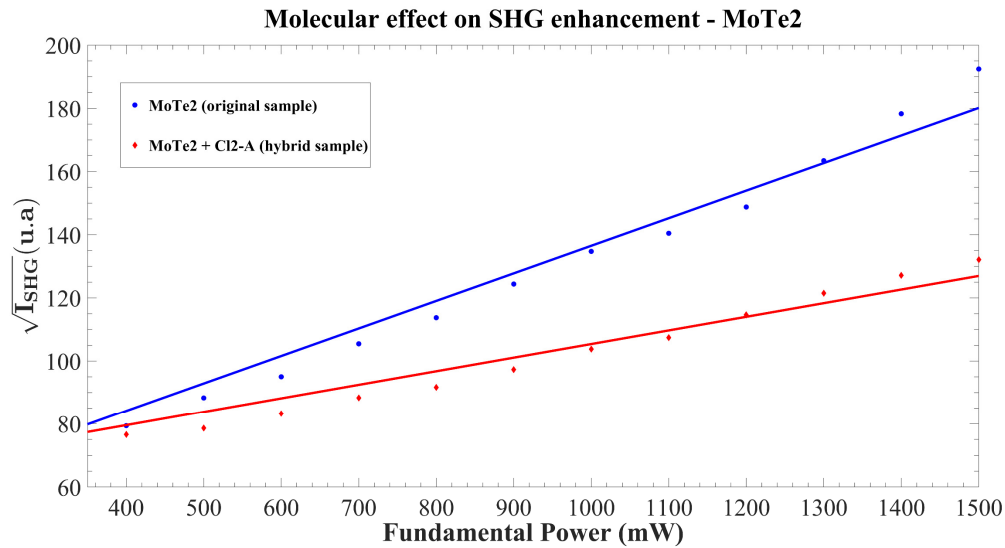


Figure 3.20: SH signal of the MoTe₂ original and hybrid flakes vs. the fundamental power at fixed polarization.

This experiment was repeated in diverse conditions but the result were similar and no SH signal enhancement was observed. This outcome did not agree with the hypothesis of our investigation, and we started looking for the possible causes that may have affected our investigation. Here in Figure 3.21, the optical image of the flake before and after scan is represented. It's clear that the flake was damaged by the laser (like thinning and patterning with layer by layer precision [243]) during the analysis.

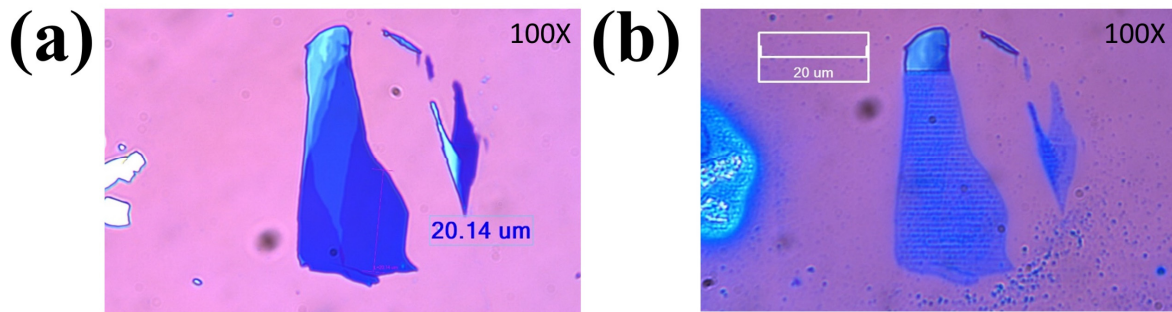


Figure 3.21: Optical image of the flake. (a): before, (b): after scan. The flake was damaged by the laser. This figure was provided by Dr. Atiye Pezeshki using an optical microscope.

Basically, by using 1064 nm laser, we were able to avoid the initial issue and detect the SH signal from the sample. But, the exposure to the laser energy density to observe any SHG from the sample was higher than the damage threshold of the sample with only few layers of atoms. As earlier explained (Eq.19), the SH signal is inversely proportional to the pulse's temporal duration and since the fundamental source pulse duration is around 15 ps, the SH signal is relatively weak.

Ultimately, here we were forced to illuminate the sample at relatively high energy, which is not the most suitable approach for 2D materials since they can easily get damaged. Conversely, failure to observe any SH signal enhancement could not provide a definite conclusion since either the molecule or flake could have been damaged during the process. Here, we have recognized that our current available resources were not the most appropriate to perform this investigation with MoTe_2 flakes.

Investigation of SHG tunability through molecular architecture in MoS_2 and WSe_2

Consequently, we decided to prove the concept using other TMDs, which would be more suitable to our available short pulsed laser source (Ti-Sapphire oscillator laser with central wavelength at 810 nm and 150 fs pulse duration). For this purpose, Molybdenum disulphide (MoS_2) and Tungsten diselenide (WSe_2) substituted the original Molybdenum ditelluride (MoTe_2). Here in Figure 3.22 the device used as the reference of our experiment is represented. This device is an all-inorganic heterostructures (gate-tunable p–n heterojunction) where a p-type device (WSe_2) is combined with a n-type device MoS_2 [223].

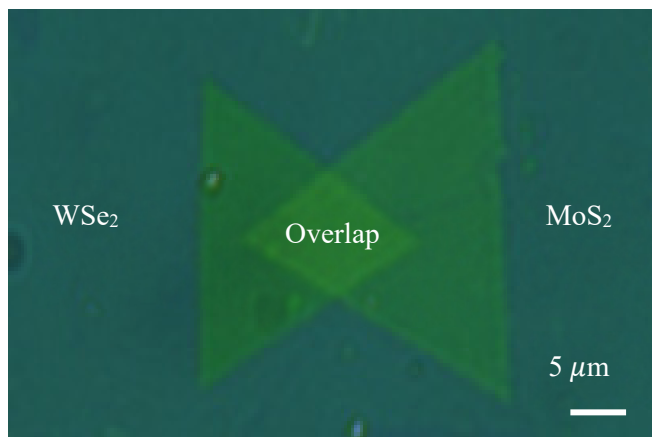


Figure 3.22: Optical image of a p–n heterojunction used as the reference device for our study. The left triangle is a p-type Tungsten diselenide (WSe_2) and the right triangle is a n-type Molybdenum disulphide (MoS_2). The central lozenge is the overlay of WSe_2 on MoS_2 . This figure was provided by Dr. Atiye Pezeshki using an optical microscope.

There are two main reasons to use the new device (Figure 3.22) as the reference of our measurements. First, there are a number of successful reports for SHG measurement on MoS_2 and WSe_2 using a Ti-Sapphire oscillator with a central wavelength around 800 nm [201,206,244–246]. On the contrary MoTe_2 requires a SHG exciting source at least over 992 nm (examples: [185,204,242]) and our only available source in this region damaged the sample (due to the long pulse temporal duration which is relatively inefficient for SHG generation). Basically, the new sample (Figure 3.22) allows us to use our traditional short pulse laser and focus on the main investigation rather than overcoming unnecessary difficulties. Consequently, this allowed us to perform our investigation with a much lower energy threshold and avoid any damage to the molecules

and TMD. During this study the quality of TMD and molecules was monitored (to avoid damaging the flake again, Figure 3.21) using an optical microscope in each round of measurement.

Second, the new device can provide more detailed information about our hypothesis. The effect of molecular doping on a n-type device and p-type device is expected to be opposite of each other. In other words, our expectation is that our hybrid device would show SHG enhancement in WSe₂ and SHG diminution in MoS₂. Basically, our setup can simultaneously measure the expected opposite effects on WSe₂ and MoS₂ by the 2D continuous molecular layer. It's noteworthy to mention that we ignored the lozenge shape overlap of two TMDs (p-n heterojunction) at this stage of our investigation.

However, the initial repeated investigation for WSe₂ was not conclusive. The case is similar to our previous study for MoTe₂, where the hybrid TMD showed relatively weaker signal. Since no SHG enhancement was ever observed, we suspected the occurrence of unwanted effects including scattering. The SH signal of the hybrid TMD must be transmitted through an extra layer (continuous 2D molecular layer) in comparison to the SH signal of the original TMD and this could result in a lower final SHG output.

Till here, we have always compared the SHG generation of the TMD with the hybrid TMD. This allows us to learn specifically about our molecular architectures themselves. Similar to the previous investigation on MoTe₂, the evaluation of SHG enhancement of hybrid TMDs was conducted by plotting the SH signal vs. the fundamental power while keeping the input polarization fixed. For WSe₂ and MoS₂, the slopes of these scans were also compared (Figure 3.23). Here, the control sample (no direct effect on SHG emission is expected from this layer) confirms the indirect effect of the additional 2D molecular layer on the SHG emission of TMDs. In both WSe₂ and MoS₂, the SHG emission of control sample is clearly weaker than the original sample.

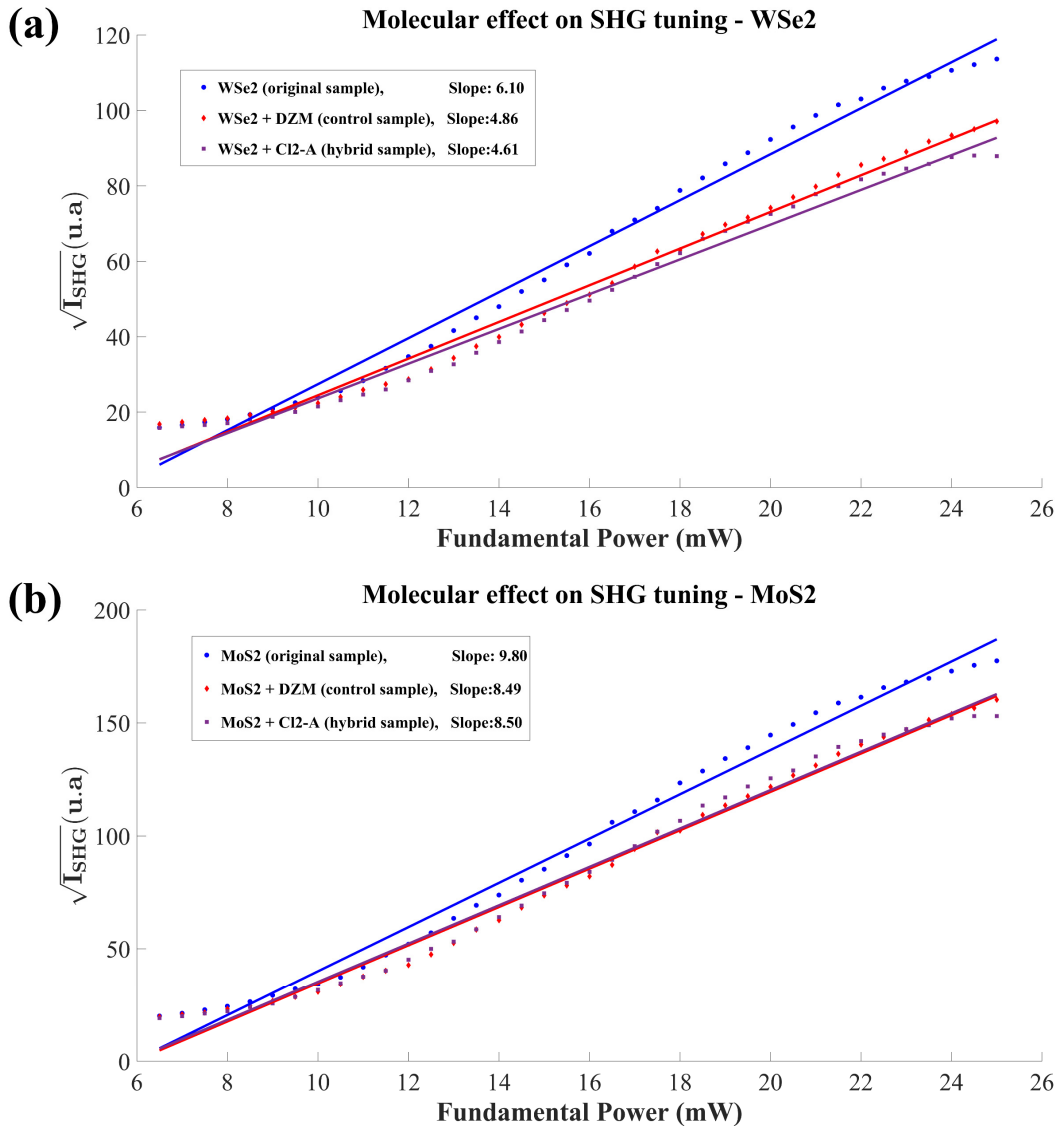


Figure 3.23: Evaluation of SHG tunability using molecular architecture. Original TMDs are represented in blue. Control samples (no direct effect expected) are represented in red. Finally, the molecular architected TMDs are represented in purple. The molecular architected TMDs (purple) are expected to induce (a): SHG enhancement on WSe₂. (b): SHG diminution in MoS₂. However, the data doesn't agree with our expectation.

Here through the control sample, we learned about the indirect effects of the molecular layer. Yet, the investigation about the effect of molecular architecture (Cl₂-A, hybrid sample) is still inconclusive. Basically, even by considering the indirect scattering by the extra molecular layer, still the behavior of our molecular assemblies is not clear even in comparison to the control samples. As mentioned earlier, the hybrid sample should lead to SHG enhancement on WSe₂ (further p doping a p-type TMD), and SHG diminution in MoS₂ (n-type). This experiment was repeated under various conditions (including distinguishing a single flake over a large area). However, the hybrid sample behavior always led to diminution of SHG in both TMDs. Mostly the behaviors of the hybrid sample and the control sample were

quite similar in our repeated measurement. Thus, we initially stopped the project at this stage. A few months later, our collaborator experienced an irregular response from the $\text{Cl}_2\text{-A}$ molecule in their own separate studies as well. Thus, we repeated our investigation with the hybrid TMD using the purified $\text{Cl}_2\text{-A}$ molecule instead. In the end, we finally observed the expected behavior from our 2D continuous $\text{Cl}_2\text{-A}$ molecular layer: SHG enhancement on WSe_2 (further p doping a p-type TMD), and SHG diminution in MoS_2 (n-type). Basically, we observed SHG enhancement on WSe_2 for the first time which verify the significant effect of purifying the molecule used on the 2D molecular layer.

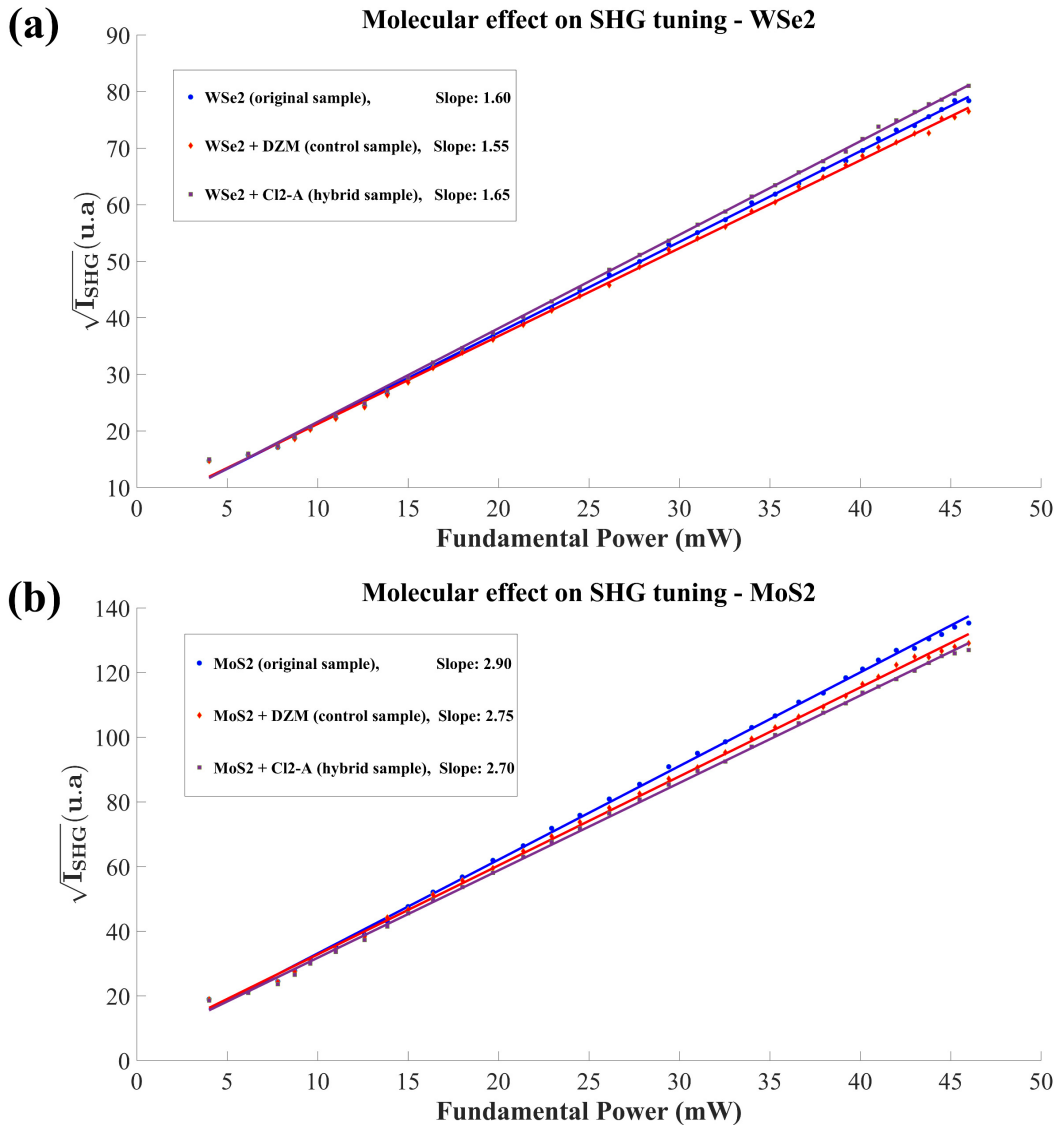


Figure 3.24: Evaluation of SHG tunability using molecular architecture (after purification of the $\text{Cl}_2\text{-A}$ molecule). Original TMDs are represented in blue. Control samples (no direct effect expected) are represented in red. Finally, the molecular architected TMDs are represented in purple. The architected TMDs (purple) are expected to induce (a): SHG enhancement on WSe_2 . (b): SHG diminution in MoS_2 . The data agrees with our expectation.

Overall, our repeated measurements with the control sample support the presence of indirect scattering which results in a lower final SHG output. The SH signal must be transmitted through an extra continuous 2D molecular layer in comparison to the SH signal of the TMD and this results in a lower final SHG output. Moreover, our last measurement supports the hypothesis to tune SHG emission of TMDs through molecular architecture. However, our observed effect is not that significant and only slightly stronger than the indirect scattering observed in control samples.

Here in this chapter, we have demonstrated the possibility to control SHG through the molecular architecture at the surface of TMDs. We suspect this effect can be optimized through further study on the molecular layer. We also suspect we can avoid the indirect effect of SHG scattering through depositing the molecular layer under the TMD since the produced SHG would no longer need to transmit through the additional molecular layer. Overall, optimizing the observed effect can lead to an interesting approach to control SHG in TMDs without using a physical gate.

Chapter 4

Pulse compression and spectral broadening based on Raman molecular response

Light amplification by stimulated emission of radiation commonly known as laser is a great tool for scientific measurement, since they can provide a train of laser pulses with a variety of pulse durations (nanosecond, picosecond, femtosecond). A significant number of applications like THz radiation generation [247], high harmonics generation [248] and laser-plasma electron acceleration [249] demand high pulse energy to reach high peak power. Consequently, low repetition rate amplified laser systems (Hz to kHz) delivering high energy pulses (millijoule and above) are the ideal laser systems for the mentioned applications.

A simple laser system

A simple laser oscillator (Figure 4.1) is the combination of a laser gain medium, a pumping source and an optical cavity [250]. Inside the optical cavity, the light is trapped to amplify by passing through the gain medium material repeatedly (confined in a resonator) and arranged in a way that at least part of it would get extracted as a light beam so it would work as an oscillator [251]. Under normal conditions, there are always more atoms at the lower energy level compared to the excited energy level of the gain medium. However, for the amplification to work properly, the gain medium needs to be kept at a state of population inversion (number of atoms at the upper energy level should be higher than the lower energy level). This condition in a laser oscillator is kept through the pumping mechanism [252].

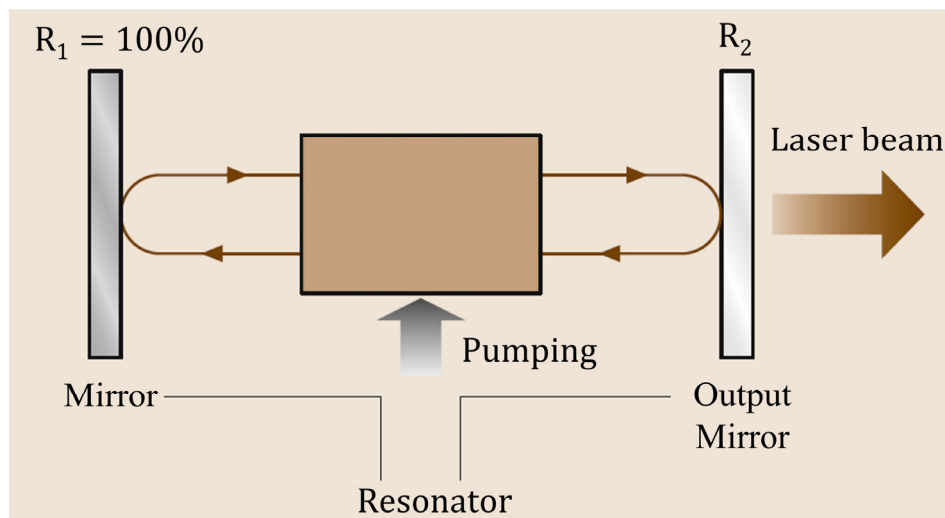


Figure 4.1: Schematic of a laser oscillator. Extracted from [89].

Chirped pulse amplification

Self-focusing challenged the improvement of laser power output for almost two decades (Figure 1.1). This issue was finally circumvented by the introduction of chirped pulse amplification (CPA) in 1985 [253]. Before CPA, the laser systems were forced to keep well under the intensity threshold (GW/cm^2) of self-focusing effect to avoid damaging the optics residing within the system [254,255].

The concept of the CPA technique is based on lowering the optical intensity during the amplification stage. The principle of this task is represented in Figure 4.2.

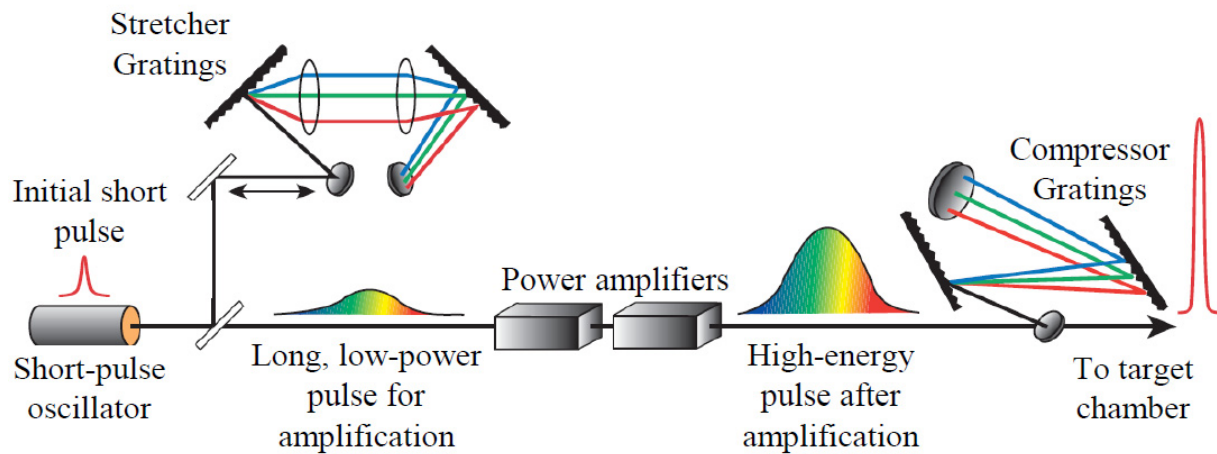


Figure 4.2: The output of an oscillator is used as a seed to be stretched, amplified and then compressed. Extracted from [256].

In CPA, the output of an oscillator is used as a seed pulse and then stretched out temporally by a factor of 1000 to 100000 times with the help of a pair of gratings: This process occurs by manipulating the low frequency components of the pulse to propagate in a shorter route to their higher frequency components, which would introduce a positive chirp [253,257]. In the second step, the stretched pulse will go through an amplification stage and since the intensity is lower than the threshold of the nonlinear effect, it will avoid harming the gain medium. Amplification at this stage can be a factor of a million or even more. In the end, the role of the grating compressor is to do the opposite of the stretcher by introducing a negative chirp [257,258]. CPA is favored in most high peak power ultrafast laser systems [259].

High peak power through pulse temporal compression

As mentioned earlier (Chapter 1), significant development has been achieved through the last six decades to generate intense ultrashort laser pulses [11,13,15,16,20]. Alongside the development of energetic laser sources, post-compression techniques have been developed to generate single-cycle pulses [260]. Basically, in order to benefit from the maximum possible peak intensity, post-compression developments have been quite important since the peak intensity of the pulse is inversely proportional to the pulse temporal duration [22].

The foundation behind every compression method can be divided into two main categories of linear pulse compression and nonlinear pulse compression. The first category belongs to compressing a pulse which was previously chirped. In these methods the chirped pulse will propagate through elements or systems to impose opposite sign dispersion, which would simply cancel the dispersion (like the last stage of CPA). The

common systems to introduce the required dispersion are prism [261], diffraction grating [258,262], chirped mirror [260] and chirped fiber Bragg grating or volume Bragg grating [263].

Principally, the time-bandwidth product (TBP) of a pulse will always be greater than the theoretical minimum [16,264,265]. A pulse with minimum time-bandwidth product is called a transform limited pulse. They are also described as a pulse with a flat spectral phase [61]. This phenomenon motivates the nonlinear post compression techniques, which require the optical bandwidth to increase first. Typically, this occurs by controlling a nonlinear behavior like self-phase modulation to spectrally broaden the pulse before the compression.

Self-phase modulation (SPM) was first observed in 1967 while working on a CS₂ filled cell [266] and in 1978, SPM was scientifically studied in silica-core fibers [267]. Later in 1987, through spectral broadening induced by SPM, single mode fiber was used to compress a 50 fs pulse to 6 fs at 620 nm [14]. Single-mode fibers are limited to the energy range of nJ, which can be labeled as low energy. The limitation occurs due to the permanent damage of ionization. In 1996, with the introduction of a novel technique based on using hollow core fibers (HCF) and noble gases, this issue was overcome and allowed pulse compression at the mJ level [18]: This has been one of the important milestones to enable the generation of isolated attosecond pulses [268]. In a typical single mode fiber, propagation is allowed in a single mode through total internal reflection. Though, a hollow fiber is a lossy waveguide where transmission is optimized by coupling to the fundamental mode. HCFs allow large diameter modes, higher damage threshold, and more control over nonlinearities.

Here in this chapter, we will discuss spectral broadening using gas-filled hollow core fibers. In fact, spectral broadening induced by the instantaneous effect of SPM in noble gases [18] is a well-studied topic with a wide range of applications [269–272] in ultrafast science. One drawback of this technique is the fact that the broadening efficiency based on SPM is inversely proportional to the pulse temporal duration at the HCF input, which makes this method not fully applicable (demands very long fiber) to compress sub-ps pulses directly to few-cycle duration [55]. Before discussing our spectral broadening investigation using molecular gases, we will go through a brief description of pulse evolution through a single mode fiber.

4.1 Pulse evolution through a fiber

The nonlinear Schrödinger equation (Eq.23) provides the theoretical framework which governs propagation through a single mode fiber.

$$i \frac{\partial A}{\partial z} = \frac{i\alpha}{2} A + \frac{\beta_2}{2} \frac{\partial^2 A}{\partial T^2} - \gamma |A|^2 A \quad \text{Eq.23}$$

The three terms in the right side of the Eq.23 are the effect on fiber losses, dispersion and nonlinearity through propagation inside the fiber respectively [273]. Moreover, (A) is a slowly varying amplitude.

The nonlinear length ($L_{NL} = \frac{1}{\gamma P_0}$, P_0 : Peak power, γ : nonlinear response of the media) and the dispersion length ($L_D = \frac{T_0^2}{|\beta_2|}$, β_2 : GVD, T_0 : Input pulse duration, for Gaussian $T_0 = \frac{T_{fwhm}}{2\ln 2}$) are two important parameters that can indicate which phenomena are ruling over the propagation behavior [274–276]. There are four general situations. The first category occurs when the fiber length is much shorter than both the nonlinear length and the dispersion length. In this category, the pulse propagating through the fiber would not be significantly affected by neither SPM nor GVD. This is actually the regime used for optical communication systems, which the fiber acts as the transporter medium. The second category occurs when the fiber length is similar to the dispersion length but much smaller than the nonlinear length. Here, the group velocity dispersion dominates the evolution of the pulse through fiber propagation. The third category belongs to the fiber length much smaller than dispersion length and relatively in close approximation or larger than the nonlinear length. Here, SPM governs the pulse evolution through fiber propagation. The last category occurs when the fiber length is equivalent or larger than both nonlinear length and dispersion length. Basically, here, both SPM and GVD significantly influence the evolution of the pulse through the fiber. The outcome of this category can lead to a distinct behavior compared to the individual behavior of SPM and GVD alone (fiber supports solitons when $\beta_2 < 0$, pulse compression using SPM and GVD when $\beta_2 > 0$) [273].

Here we have discussed the magnitude of SPM and GVD based on fiber length, but we didn't discuss the effect of each of them on the pulse itself. Self-phase modulation is a third order nonlinear event in which an intensity varying signal will experience a change of refractive index ($n(t) = n_0 + n_2 I(t)$, n_0 : medium refractive index, n_2 : nonlinear refractive index).

The phase of the pulse in the fiber is subjected to the refractive index ($\phi = nk_0 L$, L : length of the fiber) thus, the intensity varying signal causes a time-dependent phase shift as well. This phase shift is intensity and time depended, and furthermore, the shape of the pulse through this process will remain unaffected.

$$\phi(t) = (n_0 + n_2 I(t))k_0 L \quad \text{Eq.24}$$

$$\phi_{NL}(t) = n_2 I(t)k_0 L = -\frac{2\pi}{\lambda_0} n_2 I(t)L \quad \text{Eq.25}$$

where λ_0 represents the central wavelength.

The effect of this behavior on the spectrum is clearer by looking at the instantaneous frequency (ω).

$$\omega(t) = \omega_0 + \frac{\partial \phi_{NL}(t)}{\partial t} = \omega_0 - \frac{2\pi}{\lambda_0} n_2 L \frac{dI(t)}{dt} \quad \text{Eq.26}$$

The shift governed by SPM between the instantaneous frequency (ω) from the pulse center (ω_0) is known as the frequency chirp (time dependence of $\delta\omega = \omega(t) - \omega_0$). As represented in Eq.26, the frequencies at the leading edge of the pulse are decreased while frequencies at the trailing edge are increased which modifies the optical spectrum (Figure 4.3). The magnitude of this chirp is increased through the length of the fiber which is basically stating the continuous generation of new frequencies through the fiber. The evolution of the spectral broadening is dependent on the chirp of the input pulse as well [273]. In summary, propagation in hollow core fiber filled with noble gases is mainly governed by SPM.

SPM-broadened spectra for an unchirped Gaussian pulse

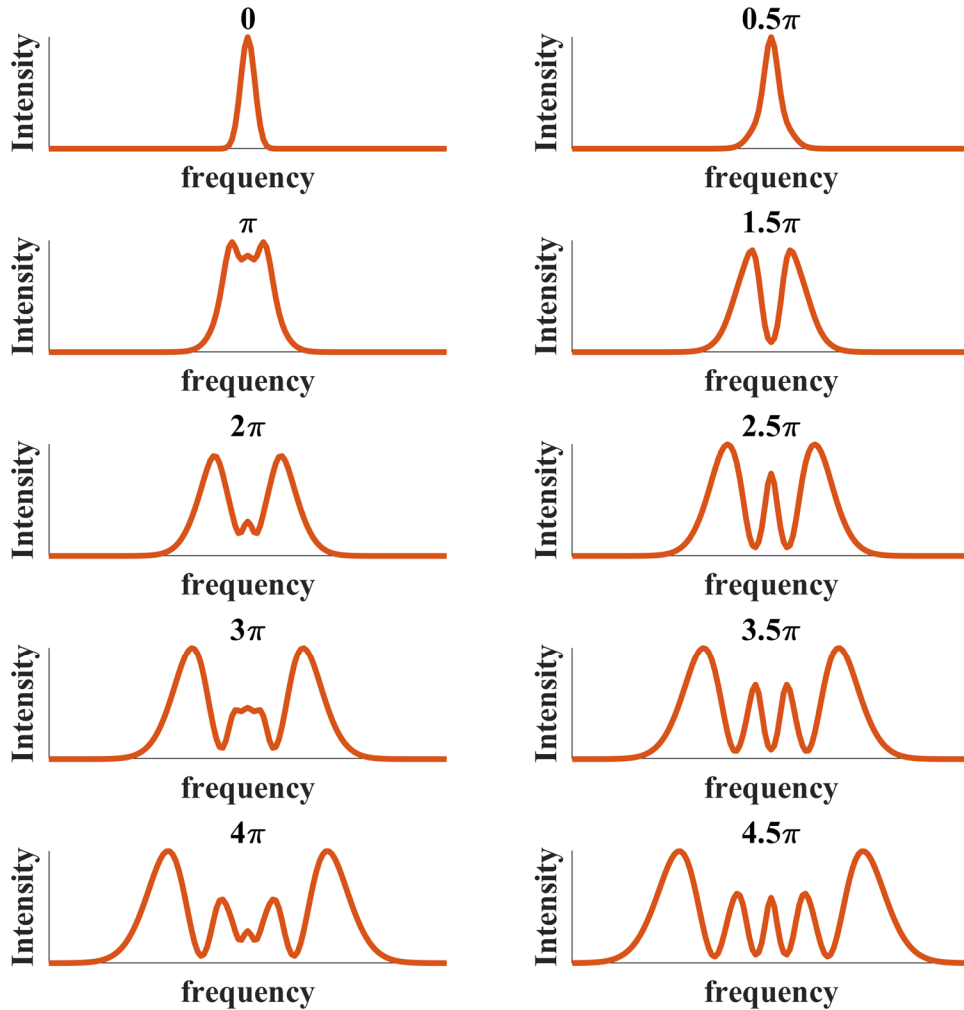


Figure 4.3: SPM-broadened spectra for an unchirped Gaussian pulse. Spectra are labeled by the maximum ϕ_{NL} .

Here we have discussed some of the simplified equations for the propagation of a pulse through a single core fiber. Though since we are mainly going to work with ultrashort pulses below 1ps, it's quite critical to consider higher order terms as well [277]. The generalized nonlinear Schrödinger equation which includes higher order nonlinear effects like self-steepening [278] and intra-pulse Raman scattering is represented in Eq.27

$$\begin{aligned} & \frac{\partial A}{\partial z} + \frac{1}{2} \left(\alpha(\omega_0) + \sum_{l=1}^{\infty} i^l \frac{\alpha_l}{l!} \frac{\partial^l}{\partial t^l} \right) A - i \sum_{n=1}^{\infty} i^n \frac{\beta_n}{n!} \frac{\partial^n A}{\partial t^n} \\ & = i \left(\gamma(\omega_0) + \frac{i}{\omega_0} \frac{\partial}{\partial t} \right) \left(A(z, t) \int_0^{\infty} R(t') |A(z, t - t')|^2 dt' \right) \end{aligned} \quad \text{Eq.27}$$

Where α_l represents the l^{th} order optical loss and β_n is the n^{th} order of dispersion. $\gamma(\omega_0)$ represents the nonlinear response of the media. $R(t')$ function covers nuclear and electronics origin responses.

Self-steepening is considered a higher order nonlinear effect which affects the pulse while propagating through the fiber. This effect is induced by the intensity dependence of the group velocity, which implies that parts of the pulse with higher power will undergo more positive time translation [279,280]. The common outcome of self-steepening is observed as the cause of the asymmetrical broadening through SPM [281–283].

Tunneling ionization in gas-filled HCF

Tunneling ionization occurs when the electrons of an atom/molecule escape by passing through the potential barrier [284]. HCF tolerates high intensities due to their gas medium (rather than glass in solid core fiber). Though, this new regime of intensity can get high enough to activate partial ionization of the gas. Ionization is considered a limit on the peak intensity of the pulse propagating through a gas-filled HCF [285]. The following are some of the common successful approaches to avoid ionization while broadening the spectrum using gas-filled HCFs. (i) Using circular polarization can decrease the ionization rate compared to a linear polarized pulse [286]. (ii): Differential pumping (gradient pumping) of gas medium through the fiber can reduce ionization by keeping the pressure at fiber inlet lower than at the fiber outlet [269].

Generally, pulse compression through SPM is limited by a compression factor [287]. For instance, a 6 meter fiber is required for 33-fold pulse compression of 170 fs pulses [288]. On the contrary, by using molecular response, we can reach a relatively higher compression factor while keeping a more compact setup.

4.2 Spectral broadening via molecular response

Here in this chapter, we will discuss the spectral broadening induced by the molecular response of nitrogen (N_2) and nitrous oxide (N_2O). Noble gases are Raman inactive media, and most of the proposed techniques for spectral broadening and pulse compression in HCFs have been focused on them. Basically, the molecular gases or more specifically Raman active gases were initially neglected since they are subjected to a delayed nonlinear response from the excitation of rotational or vibrational modes [27]. The goal of this study is to understand the behavior and the potential of molecular gases with a strong Raman response for spectral broadening. The applications of this project include super continuum generation [276], pulse temporal compression and extending the cutoff in high harmonic generation [268].

The interaction of a strong laser electric field with molecular gases induces a heavy torque into molecules which drives vibrational motion [289] and rotational alignment [290]. These events depend on the relationship between the incident pulse duration and the molecular motion. For instance, molecules will continue rotating even after the interaction, if the pulse is shorter than the molecular rotation velocity [291]. When the incident pulse duration is comparable with the molecular motion time scale (impulse excitation regime), a motion called kick rotor occurs which preserves the momentum imparted by the laser after the passage of the pulse [292,293]. The spectral broadening established on the rotational response and Raman gain is described as the delayed molecular response function $R(\tau)$ with respect to the input pulse.

$$\Delta n(t) = \int R(\tau)I(t - \tau)d\tau \quad \text{Eq.28}$$

The convolution (Eq.28) presents a sharp rise at the leading edge and a slow fall at the tailing edge. This results in the generation of new frequencies at the leading edge of $\Delta n(t)$ that create an asymmetric spectrum. The overlap of the pulse envelope with the tail and leading edge of $\Delta n(t)$ will determine the asymmetry degree (most steepest slope refer to Figure 3 in [55]). The efficiency of spectral broadening using molecular alignment gets maximized when the duration of the pulse is in the time scale range of the maximum rotational alignment [55].

On the contrary, the spectral broadening based on Kerr response (SPM based, in noble gases) is an instantaneous change of the nonlinear refractive index which is proportional to the intensity profile of laser pulse and therefore if the intensity is symmetric in time, the spectral broadening at the red edge and the blue edge are going to be equal (Eq.29)[55].

$$\begin{aligned} \Delta n(t) &= n_2 I(t) \\ \Delta \omega &= d/dt \Delta n(t) \end{aligned} \quad \text{Eq.29}$$

Here in Figure 4.4, we can observe the clear difference in the spectral broadening evolution of argon (noble gas) and N_2 (molecular gas). This measurement was conducted using a 2-meter HCF with a 500 μm core. In Figure 4.4a, the spectral broadening is induced by SPM and it almost follows symmetric spectral broadening while keeping the central wavelength almost unchanged. The slight asymmetric broadening comes from self-steepening. As discussed in section 4.1, the origin of this symmetry is related to the instantaneous nature of this electronic Kerr response.

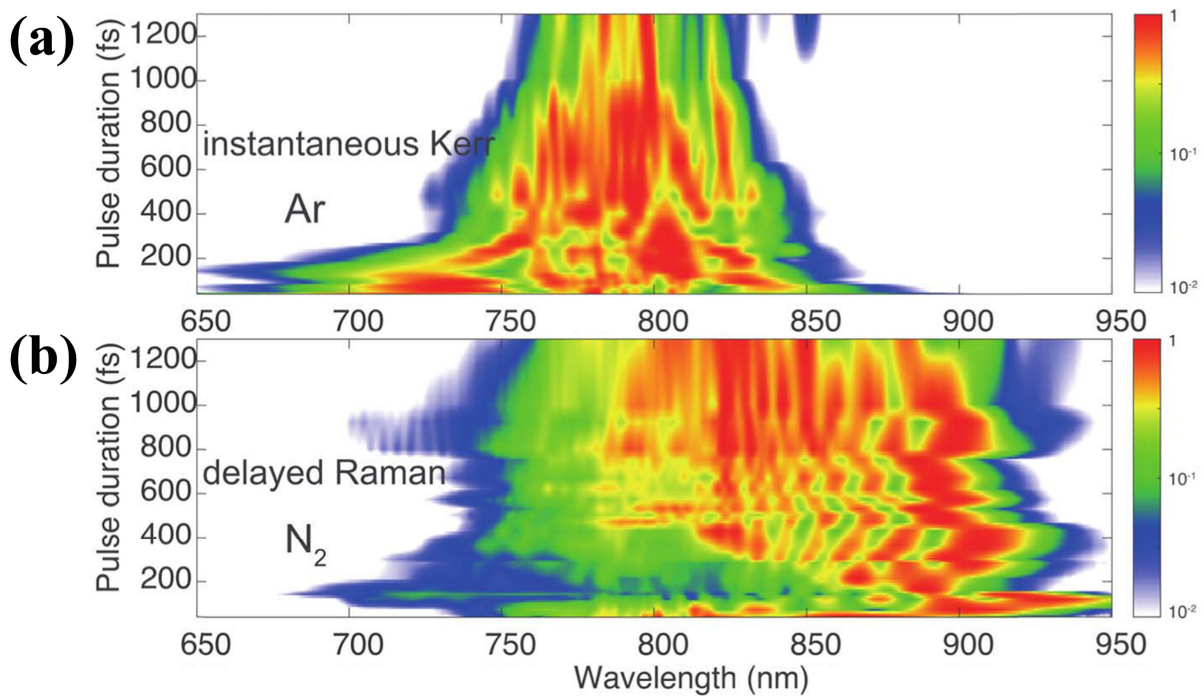


Figure 4.4: Spectral broadening vs. pulse temporal duration at fixed peak power for (a): Kerr medium (Ar) and (b): delayed response medium (N_2) at a fixed pressure of 1000 mbar.

On the other hand, from the broadening observed for the molecular gas (Figure 4.4b), the spectrum is clearly shifted more towards the red region and the broadening is clearly asymmetric. Here, the broadening bandwidth of N_2 is maximum around 120 fs, though it keeps a broad shape even in the ps regime. The overall comparison of a molecular gas and a noble gas spectral broadening clearly suggests the advantage of using molecular gases for longer pulses.

The practicality of spectral broadening and pulse compression using a molecular gas (rotational response and Raman gain) was demonstrated (Figure 4.5) using post compression chirp mirrors. Here the output of the HCF fiber with 120 fs input pulse was compressed with the help of chirped mirrors. Since each bounce inside the chirped mirrors introduced a specific amount of chirp, fused silica was also used for fine tuning. A total of 176 fs^2 negative group dispersion delay was introduced to the pulse, and the main pulse with 50% of energy was compressed to 7.8 fs (Fourier transform limit ~ 6.2 fs).

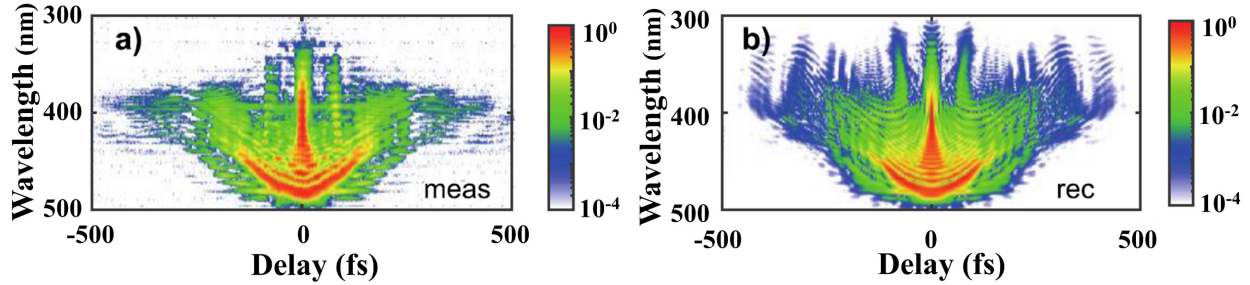


Figure 4.5: SHG FROG pulse characterization (a): measured, (b): reconstructed, 120 fs input pulses were spectrally broadened in HCFs (N_2 gas medium) and then temporally compressed (7.8fs) using chirped mirrors.

Overall, our work on high energy redshifted and enhanced spectral broadening by molecular alignment using N_2 was promising with practical applications for pulse compression using HCFs for longer pulses [55]. This study was further continued in our team which reported for the first time the observation of highly multidimensional solitary states in a molecular gas in large core fibers [53].

4.3 Spectral broadening via molecular response: beyond nitrogen

In the investigation of spectral broadening via N_2 , I was involved as an experimental team member (the data reported in 4.2). As mentioned earlier in Chapter 1, my goal during this master thesis was to gain expertise in different aspects of nonlinear optics. For this purpose, after my participation in the initial study (reported in section 4.2), while the leading team continued to push this study to highly multidimensional solitary states, I pursued this study in another aspect. For this purpose, I built a new experimental setup and started my own investigation for spectral broadening induced by molecular alignment with the help of a relatively slower molecular gas (and larger nonlinearity), nitrous oxide (N_2O). Our goals during this study were to learn about the influence of the input peak power, the input temporal duration, and then to identify the limitation of this broadening at high pressure.

Experimental setup

The overview of the experimental setup is represented in Figure 4.6. A Ti-Sapphire oscillator output is stretched and amplified and compressed again at 100Hz repetition rate, which is the input source of the experiment. This is a CPA system (introduced earlier, Figure 4.2) capable of delivering high peak intensity pulses. The spectral broadening induced by the molecular response was studied using a 2.2 meter HCF with a large core (500 μm). The technical aspects of this experiment are explained in great detail in appendix 0.

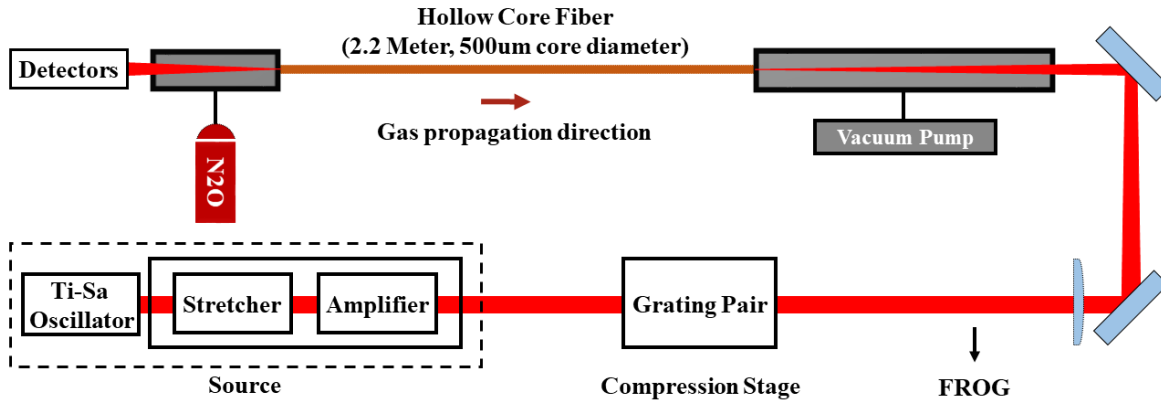


Figure 4.6: Gas-filled HCF spectral broadening experimental setup. The technical details are explained in appendix.

4.3.1 Influence of input pulse temporal duration at molecular gas spectral broadening

In this section, we resume our study of the spectral broadening induced by the molecular response (after the investigation on N₂ discussed in section 4.2), using N₂O. This gas medium was chosen, since it has relatively large nonlinearity compared to N₂. We expect relatively larger broadening due to the bigger nonlinearity of this molecule. In addition, the maximum rotational alignment of N₂ occurred at approximately 120 fs. However, N₂O is a slower gas, and we expect the maximum rotational alignment at approximately 280 fs [294].

Here in this section, we systematically scan the spectral broadening over the input molecular pressure of the system. This scan was repeated for a variety of input pulses (by positively pre-chirping the pulse, as explained in appendix). This technique has proven to be complicated and requires a more comprehensive study. However, we will go through some of the findings based on our measurements. The analysis of this section involved properly stitching the output of two spectrometers, which is explained in great details in the appendix)(iv).

Generally, in molecular gases, when the temporal duration of the pulse gets larger, it induces a larger degree of molecular alignment (enhanced nonlinearity). Moreover, the molecular alignment is delayed with respect to the pulse temporal duration as well. The combination of these two effects leads to a purely red-shifted spectrum [294].

Our CPA-based laser system generates 40 fs Fourier transform limited pulses. This regime is interesting since, we can use this technique for post compression after the output of the CPA. The spectral evolution vs. system pressure is represented in Figure 4.7. In this regime (below 100 fs), the impact of the molecular response on the spectral broadening is relatively small since there is no temporal overlap between the pulse and the delayed response of the molecule [295].

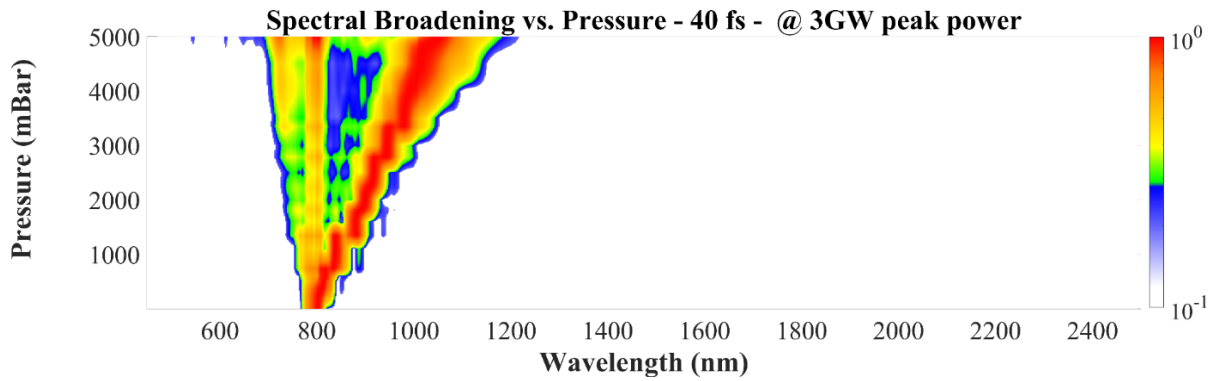


Figure 4.7: Spectral broadening over molecular pressure at 40 fs input pulse with 3GW peak power.

The magnitude of the induced molecular response on the broadening increases for pulses with over 100 fs temporal duration. In this regime, the pulse is long enough to interact with the delayed response of the molecule [296]. In Figure 4.8 we observe a remarkable broadening using 150 fs (positively pre-chirped) input pulses. Our data are in agreement with the recent publication [294] which claims supercontinuum spectra using 150 fs pulses.

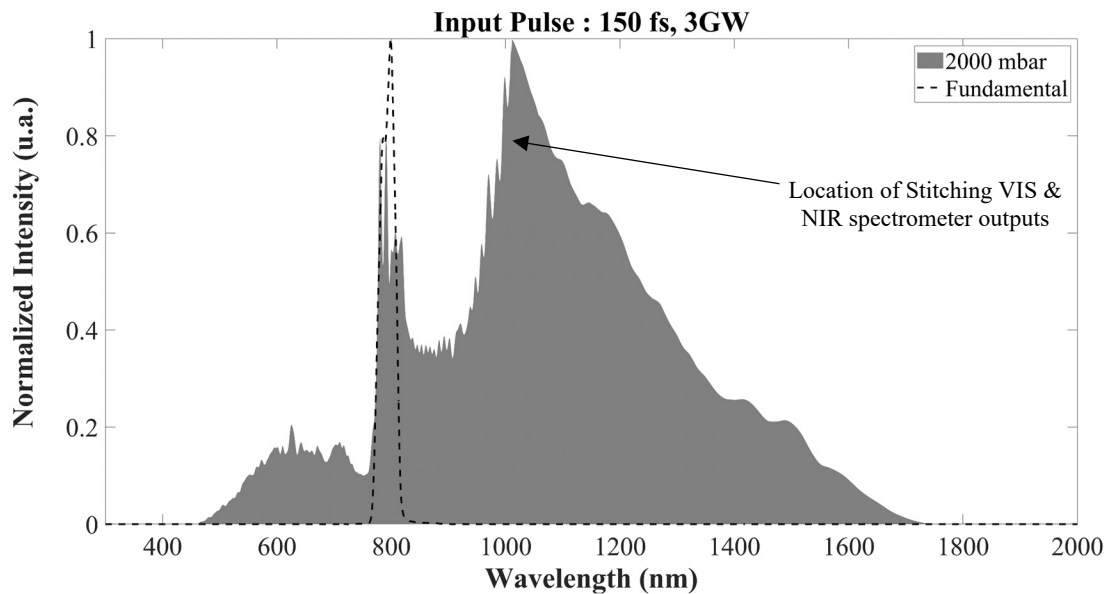


Figure 4.8: Gray area: Ultra-broad spectra measured at the output of HCF using 150 fs input pulses (2000 mbar). Dashed line: Spectra measured at vacuum condition. The delayed molecular response results in the generation of new frequencies at the leading edge of $\Delta n(t)$.

Repeating this scan at 280 fs (positively pre-chirped) leads to a more symmetric spectrum. At this time scale, the peak of the molecular response alignment overlaps with the tailing edge of the pulse which induces a more symmetric broadening.

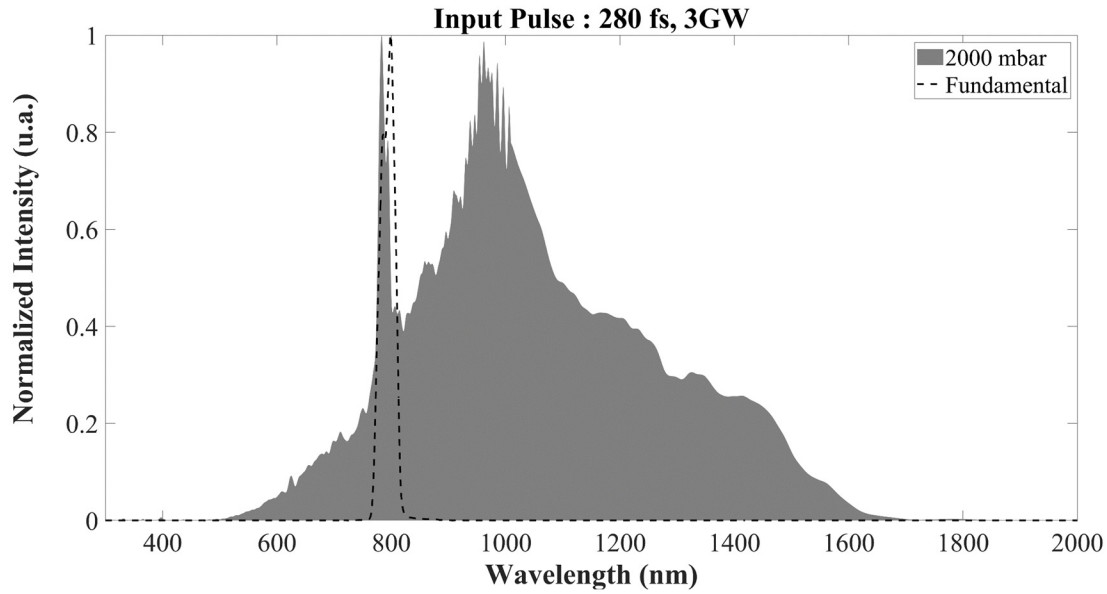


Figure 4.9: Ultra-broad spectra measured at the HCF outlet using 280 fs input pulses (2000 mbar). In this regime, the spectrum is more symmetric since this pulse duration matches the time resolution of scale of the maximum rotational alignment of N_2O molecules.

The overall spectral evolution vs. system pressure for this pulse duration is represented in Figure 4.10. The broadening grows rapidly up to almost 4000 mbar. The main energetic peak (observed at 1000 nm in Figure 4.9) is moves continuously to longer wavelengths and ends up near 1400 nm at 5000 mbar (see the red trace in Figure 4.10).

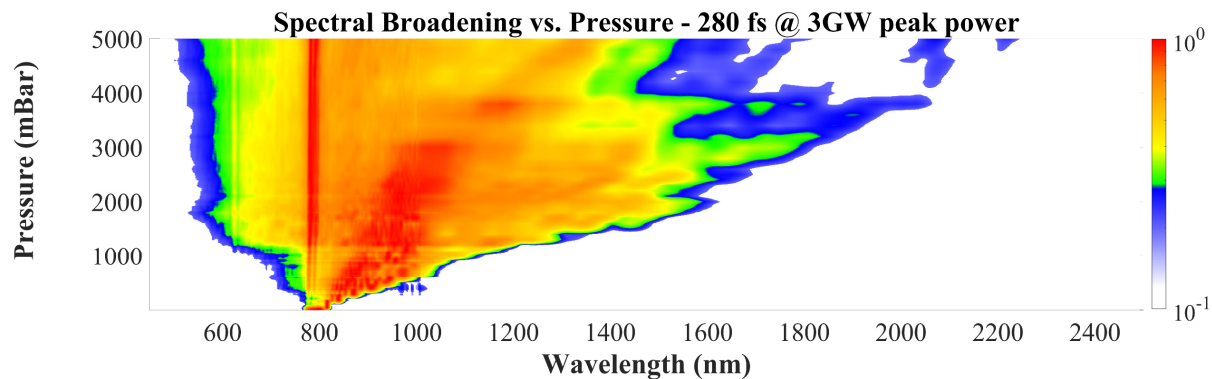


Figure 4.10: Spectral broadening over molecular pressure at 280 fs input pulse with 3GW peak power.

Although the maximum efficiency occurs at 280 fs, this technique remains relatively efficient even with pulses with longer time durations (Figure 4.11).

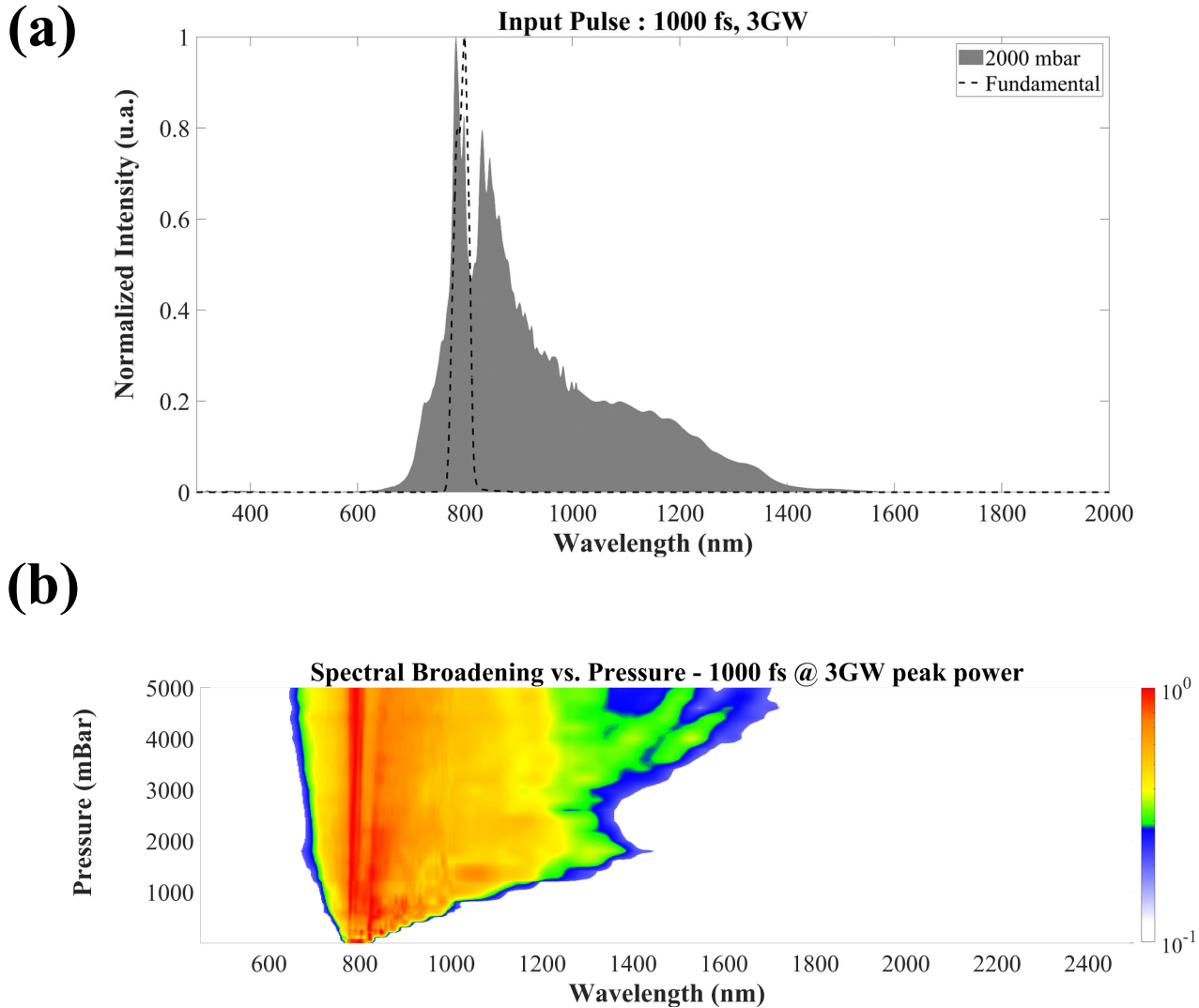


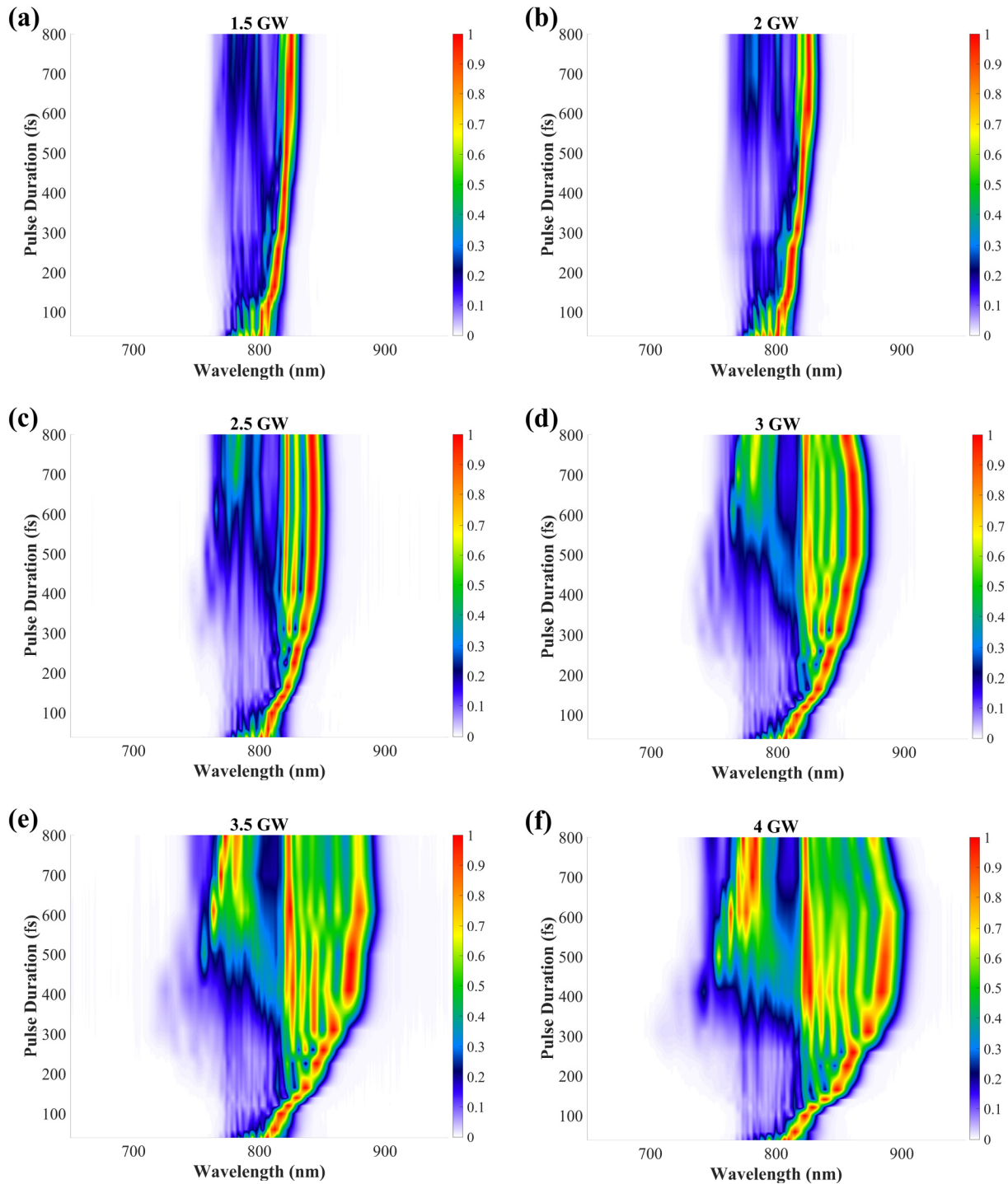
Figure 4.11: (a): Broad spectra measured at the HCF outlet using 1000 fs input pulses (2000 mbar). The broadening is less efficient compared to Figure 4.9 and Figure 4.10 (280 fs). Though the method is still relatively efficient at increasing the bandwidth of input pulse. (b): Spectral broadening over molecular pressure at 1000 fs input pulse with 3GW peak power.

Here we have presented the spectral broadening induced by the molecular response of N_2O at three different regimes of the input pulse duration with respect to the maximum rotational alignment time scale (experimental data for a variety of input pulse durations are provided in appendix).

Overall, the large nonlinearity of N_2O leads to a relatively efficient spectral broadening. As mentioned, our data agree with the initial expectation that the maximum broadening occurs at the maximum rotational alignment time scale. In the next section we will study the influence of input peak power on the spectral broadening.

4.3.2 Influence of the input peak power on the molecular gas spectral broadening

In this section, we study the effect of the input peak power on the spectral broadening induced by the molecular response of N_2O . In Figure 4.12, the system pressure was kept at a relatively low level (200 mbar) to avoid triggering unwanted nonlinear effects.



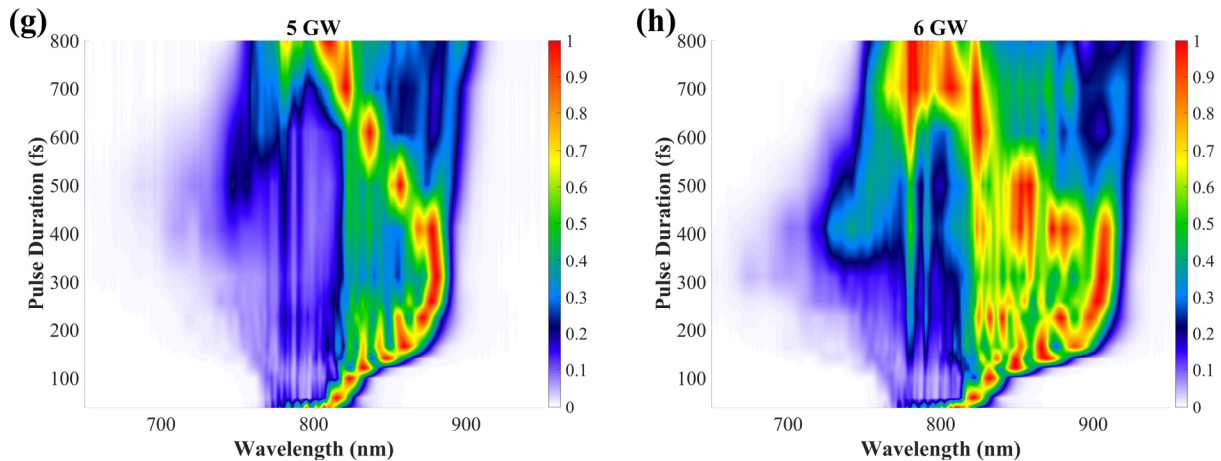


Figure 4.12: Spectral broadening by nitrous oxide at 200mbar for a variety of input peak powers.

In our investigation in the low-pressure regime, a clear difference is observed on the spectral evolution laser powers for below and over 2 GW. In Figure 4.12 a-b (1.5, 2 GW), the main energetic peak moves continuously in the red regime by increasing the input pulse duration. Originally, we expected a maximum broadening for the pulse duration matching the time scale of the maximum rotational alignment. However, this is not the case at least for Figure 4.12a-b.

After surpassing the 2 GW input peak power, we can clearly observe that the main energy peak slowly returns to the fundamental wavelength. This effect is quite clear by comparing the 3.5 GW data with the 4 GW data. Although the broadening bandwidth seems identical for these two measurements, this effect is more pronounced at 4 GW compared to 3 GW. (clear difference at 600 fs to 800 fs). Finally, in the last two measurements with a relatively high peak power (5-6 GW), the energy completely returns to the fundamental at 800 fs and even moves toward the blue region in the last figure.

As mentioned, this technique is complicated and requires a more comprehensive study. Our initial expectation from 1 D simulations and concepts was that the broadening should be maximum for a pulse duration on the time scale of the molecular response. Thus, we expected that the maximum alignment would occur around 280 fs (N_2O), though our data in Figure 4.12 do not support that. The overall trend in Figure 4.12 supports the impression that there is an inverse relationship between the pulse duration and the required peak power to maximize the broadening. Nevertheless, our high-pressure measurements are consistent with the assumption of maximum broadening obtained for a pulse duration corresponding to the time scale of the molecular alignment. In summary, when we are not limited by the input peak power or the system pressure, the maximum broadening efficiency follows the expected behavior. However, the efficiency of the broadening at different input pulse durations is extremely sensitive to the input peak power. Basically, pulses with shorter duration require higher peak power or molecular pressure to reach the maximum available spectral broadening.

Chapter 5

Conclusion

This thesis covers studies in three aspects of nonlinear optics and ultrafast optics. In Chapter 2, the description of ultrashort pulses and some of the fundamental approaches to characterize them was discussed. This discussion was followed with a project to transfer the concept of FROSt for pulse characterization to nonlinear microscopy system. In Chapter 3 we discussed the possibility of using ultrashort laser pulses for material characterization with the help of a nonlinear optical microscope. Finally, in Chapter 4, we discussed the importance of time compression to achieve high peak power sources. This discussion was followed by a project to develop a novel technique for the compression of laser pulses.

In Chapter 2, we discussed a newly developed technique in the ALLS laboratory called FROSt. This spectrographic technique is effective for characterizing ultra-broadband pulses since it doesn't require the phase matching condition for the nonlinear gate be satisfied. The primary requirement to implement a FROSt technique is to have a pump with sufficient intensity to photoexcite the material in order to create a transient gate. The goal of this project was to extend this technique from low repetition rate systems with high energy pulses (proof-of-concept system) to high repetition rate oscillators with much lower energy pulses (and then implement this technique inside the microscope system). There were two main challenges involved with this project: the insufficient intensity to create the transient gate and the effect of the high repetition rate pulses on the transient gate. In our study, we observed a transient gate that clearly appears under 10 MHz. The same gate appeared at 80 MHz, but the signal-to-noise ratio was lower. Although the appearance of the gate led to the drop of intensity in our probe arm, the amount of drop (1%) is not sufficient for the needs of the reconstruction algorithm (minimum 10%). This measurement was conducted at the upper energy limit of our 80 MHz Ti-Sapphire oscillator. Based on our estimation, tighter focusing with the help of an objective microscope lens, would provide the adequate pump fluence to run the reconstruction algorithm. This technique can be integrated into a nonlinear microscopy system in a collinear geometry. We recommend pumping at a different wavelength (like using double frequency of the pump) to avoid contaminating the measurement with the pump signal

In Chapter 3, we discussed the fundamental and technical concepts of our nonlinear microscopy system. This discussion was followed with a project to control the second harmonic generation signal from transition metal dichalcogenide (TMD) media. The properties of an TMD inorganic layer are determined by its pristine atomic arrangement and through molecular architecture we have demonstrated the possibility of controlling SHG at the surface of TMDs. We suspect that we can avoid the indirect effect of SHG scattering by depositing the additional molecular layer under the TMD, since the produced SHG would no longer need to transmit through this layer. Overall, optimizing the observed effect can lead to an interesting approach to control SHG of TMDs without using a physical gate.

High peak pulse energy is the primary obligation of a various number of applications, and pulse time compression is a key factor in achieving this. Alongside the development of energetic laser sources, post-compression techniques have been developed to generate single-cycle pulses. Pulse compression induced by self-phase modulation in HCF using noble gases is a well-known topic, since they have a high ionization potential and insignificant dispersion at low pressure. Noble gases are Raman inactive media, and Raman active gases were initially neglected since they are subjected to a delayed nonlinear response from the excitation of rotational or vibrational modes. When the incident pulse duration is comparable with the molecular motion time scale (impulse excitation regime), a motion called kick rotor occurs which preserves the momentum imparted by the laser after the passage of the pulse. Here, we discussed the spectral broadening induced by the molecular response of nitrogen (N_2) and nitrous oxide (N_2O). Overall, our work on strong redshift energy and enhanced spectral broadening by molecular alignment using N_2 was promising with practical applications for longer pulse compression using HCFs. Furthermore, the large nonlinearity of N_2O leads to a larger spectral broadening. The overall trend of our measurements supports the impression that there is an inverse relationship between the duration of the pulses and the required peak power to maximize broadening.

REFERENCES

1. Mokhiemer TA. On the Quantum Theory of Radiation [Internet]. 2008 [cited 2020 Dec 15]. Available from: [/paper/On-the-Quantum-Theory-of-Radiation-Mokhiemer/779bf2dd1c815af7ef3aa91ac7b341b7889cd8da](#)
2. Ladenburg R. Untersuchungen über die anomale Dispersion angeregter Gase. *Z Für Phys.* 1928 Jan 1;48(1):15–25.
3. MSU Faculty of Mechanics and Mathematics [Internet]. [cited 2020 Dec 15]. Available from: <http://www.famhist.ru/famhist/hal/00bed152.htm>
4. Gordon JP, Zeiger HJ, Townes CH. Molecular Microwave Oscillator and New Hyperfine Structure in the Microwave Spectrum of NH_3 . *Phys Rev.* 1954 Jul 1;95(1):282–4.
5. Hecht J. Short history of laser development. *Opt Eng.* 2010 Sep;49(9):091002.
6. Stimulated Optical Radiation in Ruby | Nature [Internet]. [cited 2020 Dec 15]. Available from: <https://www.nature.com/articles/187493a0>
7. Terhune RW, Maker PD, Savage CM. Optical Harmonic Generation in Calcite. *Phys Rev Lett.* 1962;8(10):404–6.
8. Trebino R. Frequency-Resolved Optical Gating: The Measurement of Ultrashort Laser Pulses [Internet]. New York: Springer; 2000. Available from: <http://site.ebrary.com/lib/alltitles/docDetail.action?docID=10645287>
9. Ian A. Walmsley, Christophe Dorrer. Characterization of ultrashort electromagnetic pulses. *Adv Opt Photonics.* 2009;1(2):308–437.
10. Campagnola P. Second harmonic generation imaging microscopy: applications to diseases diagnostics. *Anal Chem.* 2011;83(9):3224–31.
11. McClung FJ, Hellwarth RW. Giant Optical Pulsations from Ruby: *Journal of Applied Physics*, 33(3), 828-829. *J Appl Phys.* 1962;33(3):828–9.
12. Lamb WE. Theory of an Optical Maser. *Phys Rev.* 1964 Jun 15;134(6A):A1429–50.
13. Ippen E p., Shank C v., Dienes A. Passive mode locking of the cw dye laser. *Appl Phys Lett.* 1972 Oct 15;21(8):348–50.
14. Fork RL, Cruz CH, Becker PC, Shank CV. Compression of optical pulses to six femtoseconds by using cubic phase compensation. *Opt Lett.* 1987;12(7):483–5.
15. Spence DE, Kean PN, Sibbett W. 60-fsec pulse generation from a self-mode-locked Ti:sapphire laser. *Opt Lett.* 1991 Jan 1;16(1):42–4.
16. Strickland D, Mourou G. Compression of amplified chirped optical pulses: *Optics Communications*, 56(3), 219-221. 1985;
17. Kelley PL. Self-Focusing of Optical Beams. *Phys Rev Lett.* 1965 Dec 27;15(26):1005–8.

18. Nisoli M, de Silvestri S, Svelto O. Generation of high energy 10 fs pulses by a new pulse compression technique. *Appl Phys Lett*. 1996;68(20):2793–5.
19. Goulielmakis E, Schultze M, Hofstetter M, Yakovlev VS, Gagnon J, Uiberacker M, Aquila AL, Gullikson EM, Attwood DT, Kienberger R, Krausz F, Kleineberg U. Single-cycle nonlinear optics. *Science*. 2008;320(5883):1614–7.
20. Brabec T, editor. *Strong Field Laser Physics*. New York, NY: Springer New York; 2009. (Springer Series in Optical Sciences; vol. 134).
21. Jeong J, Cho S, Hwang S, Lee B, Yu TJ. Modeling and Analysis of High-Power Ti:sapphire Laser Amplifiers—A Review. *Appl Sci*. 2019 Jan;9(12):2396.
22. Boyd RW. *Nonlinear optics*. Fourth edition. Amsterdam: Academic Press; 2019.
23. M.S.Tyagi RVO. Minority carrier recombination in heavily-doped silicon. 1981;26(6):577–97.
24. Trebino R, DeLong KW, Fittinghoff DN, Sweetser JN, Krumbügel MA, Richman BA, Kane DJ. Measuring ultrashort laser pulses in the time-frequency domain using frequency-resolved optical gating. *Rev Sci Instrum*. 1997;68(9):3277–95.
25. Anderson ME, Monmayrant A, Gorza S-P, Wasylczyk P, Walmsley IA. SPIDER: A decade of measuring ultrashort pulses: *Laser Physics Letters*, 5(4), 259-266. 2008;
26. Leblanc A, Lassonde P, Petit S, Delagnes J-C, Haddad E, Ernotte G, Bionta MR, Gruson V, Schmidt BE, Ibrahim H, Cormier E, Légaré F. Phase-matching-free pulse retrieval based on transient absorption in solids. *Opt Express*. 2019;27(20):28998–9015.
27. Haddad E, Safaei R, Leblanc A, Piccoli R, Jeong Y-G, Ibrahim H, Schmidt BE, Morandotti R, Razzari L, Légaré F, Lassonde P. Molecular gases for pulse compression in hollow core fibers. *Opt Express*. 2018;26(19):25426–36.
28. Thibault P, Dierolf M, Bunk O, Menzel A, Pfeiffer F. Probe retrieval in ptychographic coherent diffractive imaging. *Ultramicroscopy*. 2009;109(4):338–43.
29. Kleinman DA. Theory of Second Harmonic Generation of Light. *Phys Rev*. 1962 Nov 15;128(4):1761–75.
30. OPTICAL SECOND HARMONIC GENERATION IN PIEZOELECTRIC CRYSTALS: *Applied Physics Letters: Vol 5, No 1* [Internet]. [cited 2020 Dec 18]. Available from: <https://aip.scitation.org/doi/abs/10.1063/1.1754022?journalCode=apl>
31. Eguchi K, Tanabe Y, Ogawa T, Tanaka M, Kawabe Y, Hanamura E. Second-harmonic generation from pyroelectric and ferrimagnetic GaFeO₃. *JOSA B*. 2005 Jan 1;22(1):128–37.
32. Collagen reorganization at the tumor-stromal interface facilitates local invasion | *BMC Medicine* | Full Text [Internet]. [cited 2020 Dec 18]. Available from: <https://bmcmmedicine.biomedcentral.com/articles/10.1186/1741-7015-4-38>
33. Conklin MW, Eickhoff JC, Riching KM, Pehlke CA, Eliceiri KW, Provenzano PP, Friedl A, Keely PJ. Aligned collagen is a prognostic signature for survival in human breast carcinoma. *Am J Pathol*. 2011 Mar;178(3):1221–32.

34. Simultaneous imaging of GFP, CFP and collagen in tumors in vivo using multiphoton microscopy | BMC Biotechnology | Full Text [Internet]. [cited 2020 Dec 18]. Available from: <https://bmcbiotechnol.biomedcentral.com/articles/10.1186/1472-6750-5-14>
35. Williams RM, Zipfel WR, Webb WW. Interpreting Second-Harmonic Generation Images of Collagen I Fibrils. *Biophys J*. 2005 Feb 1;88(2):1377–86.
36. Mansfield JC, Winlove CP, Moger J, Matcher SJ. Collagen fiber arrangement in normal and diseased cartilage studied by polarization sensitive nonlinear microscopy. *J Biomed Opt*. 2008 Aug;13(4):044020.
37. Brockbank KGM, MacLellan WR, Xie J, Hamm-Alvarez SF, Chen ZZ, Schenke-Layland K. Quantitative second harmonic generation imaging of cartilage damage. *Cell Tissue Bank*. 2008 Dec;9(4):299–307.
38. Lilledahl MB, Pierce DM, Ricken T, Holzapfel GA, Davies C de L. Structural analysis of articular cartilage using multiphoton microscopy: input for biomechanical modeling. *IEEE Trans Med Imaging*. 2011 Sep;30(9):1635–48.
39. Pfeffer CP, Olsen BR, Ganikhanov F, Légaré F. Imaging skeletal muscle using second harmonic generation and coherent anti-Stokes Raman scattering microscopy. *Biomed Opt Express*. 2011 Apr 27;2(5):1366–76.
40. Ralston E, Swaim B, Czapiga M, Hwu W-L, Chien Y-H, Pittis MG, Bembi B, Schwartz O, Plotz P, Raben N. Detection and Imaging of Non-Contractile Inclusions and Sarcomeric Anomalies in Skeletal Muscle by Second Harmonic Generation Combined with Two-Photon Excited Fluorescence. *J Struct Biol*. 2008 Jun;162(3):500–8.
41. Mertz J. Nonlinear microscopy: new techniques and applications. *Curr Opin Neurobiol*. 2004;14(5):610–6.
42. Lasers and Electro-optics [Internet]. [cited 2020 Dec 20]. Available from: <https://www.cambridge.org/core/books/lasers-and-electrooptics/1299703ECCCB4673F9EE0B41A55B75CE>
43. Sun Z, Martinez A, Wang F. Optical modulators with 2D layered materials. *Nat Photonics*. 2016 Apr;10(4):227–38.
44. Cai W, Vasudev AP, Brongersma ML. Electrically controlled nonlinear generation of light with plasmonics. *Science*. 2011 Sep 23;333(6050):1720–3.
45. Seyler KL, Schaibley JR, Gong P, Rivera P, Jones AM, Wu S, Yan J, Mandrus DG, Yao W, Xu X. Electrical control of second-harmonic generation in a WSe₂ monolayer transistor. *Nat Nanotechnol*. 2015 May;10(5):407–11.
46. Wang G, Marie X, Gerber I, Amand T, Lagarde D, Bouet L, Vidal M, Balocchi A, Urbaszek B. Giant Enhancement of the Optical Second-Harmonic Emission of WSe_2 Monolayers by Laser Excitation at Exciton Resonances. *Phys Rev Lett*. 2015 Mar 4;114(9):097403.
47. Das S, Robinson JA, Dubey M, Terrones H, Terrones M. Beyond Graphene: Progress in Novel Two-Dimensional Materials and van der Waals Solids: *Annual Review of Materials Research*, 45(1), 1-27. 2015;

48. Electric Field Effect in Atomically Thin Carbon Films | Science [Internet]. [cited 2020 Nov 16]. Available from: <https://science.sciencemag.org/content/306/5696/666.abstract>
49. Zeng M, Xiao Y, Liu J, Yang K, Fu L. Exploring Two-Dimensional Materials toward the Next-Generation Circuits: From Monomer Design to Assembly Control. *Chem Rev.* 2018;118(13):6236–96.
50. Ryu YK, Frisenda R, Castellanos-Gomez A. Superlattices based on van der Waals 2D materials. *Chem Commun.* 2019 Sep 24;55(77):11498–510.
51. Gobbi M, Orgiu E, Samorì P. When 2D Materials Meet Molecules: Opportunities and Challenges of Hybrid Organic/Inorganic van der Waals Heterostructures. *Adv Mater Deerfield Beach Fla.* 2018;30(18):e1706103.
52. Cerullo G, Nisoli M, Stagira S, de Silvestri S, Tempea G, Krausz F, Ferencz K. Mirror-dispersion-controlled sub-10-fs optical parametric amplifier in the visible. *Opt Lett.* 1999;24(21):1529–31.
53. Safaei R, Fan G, Kwon O, Légaré K, Lassonde P, Schmidt BE, Ibrahim H, Légaré F. High-energy multidimensional solitary states in hollow-core fibres. *Nat Photonics.* 2020 Dec;14(12):733–9.
54. OSA | Raman effect in the spectral broadening of ultrashort laser pulses in saturated versus unsaturated hydrocarbon molecules [Internet]. [cited 2020 Dec 15]. Available from: <https://www.osapublishing.org/oe/fulltext.cfm?uri=oe-28-2-980&id=425669>
55. Fan G, Safaei R, Kwon O, Schuster V, Légaré K, Lassonde P, Ehteshami A, Arias L, Laramée A, Beaudoin-Bertrand J, Limpert J, Tao Z, Spanner M, Schmidt BE, Ibrahim H, Baltuška A, Légaré F. High energy redshifted and enhanced spectral broadening by molecular alignment. *Opt Lett.* 2020;45(11):3013.
56. Lavenu L, Natile M, Guichard F, Zaouter Y, Hanna M, Mottay E, Georges P. High-energy few-cycle Yb-doped fiber amplifier source based on a single nonlinear compression stage. *Opt Express.* 2017 Apr 3;25(7):7530–7.
57. Mansour BF, Anis H, Zeidler D, Corkum PB, Villeneuve DM. Generation of 11 fs pulses by using hollow-core gas-filled fibers at a 100 kHz repetition rate. *Opt Lett.* 2006 Nov 1;31(21):3185–7.
58. Chen B-H, Kretschmar M, Ehberger D, Blumenstein A, Simon P, Baum P, Nagy T. Compression of picosecond pulses from a thin-disk laser to 30fs at 4W average power. *Opt Express.* 2018 Feb 19;26(4):3861–9.
59. Rothhardt J, Hädrich S, Carstens H, Herrick N, Demmler S, Limpert J, Tünnermann A. 1 MHz repetition rate hollow fiber pulse compression to sub-100-fs duration at 100 W average power. *Opt Lett.* 2011 Dec 1;36(23):4605–7.
60. Hädrich S, Rothhardt J, Eidam T, Limpert J, Tünnermann A. High energy ultrashort pulses via hollow fiber compression of a fiber chirped pulse amplification system. *Opt Express.* 2009 Mar 2;17(5):3913–22.
61. Trebino R. *Frequency-Resolved Optical Gating: The Measurement of Ultrashort Laser Pulses* [Internet]. New York: Springer; 2000. Available from: <http://site.ebrary.com/lib/alltitles/docDetail.action?docID=10645287>

62. Kane DJ, Trebino R. Single-shot measurement of the intensity and phase of an arbitrary ultrashort pulse by using frequency-resolved optical gating. *Opt Lett.* 1993;18(10):823–5.
63. Armstrong JA. MEASUREMENT OF PICOSECOND LASER PULSE WIDTHS. *Appl Phys Lett.* 1967;10(1):16–8.
64. Dantus M, Bowman RM, Zewail AH. Femtosecond laser observations of molecular vibration and rotation. *Nature.* 1990 Feb;343(6260):737–9.
65. Miranda M, Arnold CL, Fordell T, Silva F, Alonso B, Weigand R, L’Huillier A, Crespo H. Characterization of broadband few-cycle laser pulses with the d-scan technique. *Opt Express.* 2012 Aug 13;20(17):18732–43.
66. Wong V, Walmsley IA. Analysis of ultrashort pulse-shape measurement using linear interferometers. *Opt Lett.* 1994;19(4):287.
67. Dorrer C, Kang I. Highly sensitive direct characterization of femtosecond pulses by electro-optic spectral shearing interferometry. *Opt Lett.* 2003;28(6):477–9.
68. Kang I, Dorrer C, Quochi F. Implementation of electro-optic spectral shearing interferometry for ultrashort pulse characterization. *Opt Lett.* 2003;28(22):2264–6.
69. Birge JR, Ell R, Kärtner FX. Two-dimensional spectral shearing interferometry for few-cycle pulse characterization. *Opt Lett.* 2006;31(13):2063–5.
70. Iaconis C, Walmsley IA. Spectral phase interferometry for direct electric-field reconstruction of ultrashort optical pulses. *Opt Lett.* 1998;23(10):792–4.
71. Walker BH. *Optical engineering fundamentals*. 2nd ed. Bellingham, Wash. (1000 20th St. Bellingham WA 98225-6705 USA): SPIE; 2008. (Tutorial texts in optical engineering; vol. v. TT82).
72. Chartier G. *Introduction to Optics* [Internet]. New York, NY: Springer Science+Business Media Inc; 2005. (Advanced texts in physics). Available from: <http://site.ebrary.com/lib/alltitles/docDetail.action?docID=10228890>
73. electromagnetic spectrum | Definition, Diagram, & Uses | Britannica [Internet]. [cited 2020 Dec 9]. Available from: <https://www.britannica.com/science/electromagnetic-spectrum>
74. Paschotta R. *Monochromatic Light* [Internet]. 2020. Available from: https://www.rp-photonics.com/monochromatic_light.html
75. Murphy DB, Davidson MW. *Fundamentals of light microscopy and electronic imaging* [Internet]. 2nd ed. Hoboken, N.J: Wiley-Blackwell; 2013. Available from: <http://search.ebscohost.com/login.aspx?direct=true&scope=site&db=nlebk&db=nlabk&AN=489132>
76. Nolte S, Schrepel F, Dausinger F, editors. *Ultrashort Pulse Laser Technology: Laser Sources and Applications*. 1st ed. 2016. Cham and Heidelberg and New York and Dordrecht and London: Springer; 2016. (Springer Series in Optical Sciences; vol. 195).
77. Maiman TH. Stimulated Optical Radiation in Ruby. *Nature.* 1960 Aug;187(4736):493–4.

78. Franken PA, Hill AE, Peters CW, Weinreich G. Generation of Optical Harmonics. *Phys Rev Lett.* 1961 Aug 15;7(4):118–9.
79. Sauter EG. *Nonlinear Optics*. New York: Wiley-Interscience; 1996. 232 p.
80. Bass M, Franken PA, Hill AE, Peters CW, Weinreich G. Optical Mixing. *Phys Rev Lett.* 1962 Jan 1;8(1):18–18.
81. Bass M, Franken PA, Ward JF, Weinreich G. Optical Rectification. *Phys Rev Lett.* 1962 Dec 1;9(11):446–8.
82. *Principles of Lasers* | Orazio Svelto | Springer [Internet]. [cited 2021 Jan 10]. Available from: <https://www.springer.com/gp/book/9781441913012>
83. Trebino R. Lecture notes. Georgia Tech;
84. Shapiro SL. *Ultrashort Light Pulses: Picosecond Techniques and Applications*. Berlin and Heidelberg: Springer; 1977. (Topics in Applied Physics; vol. 18).
85. Milonni PW, Eberly JH. *Laser physics* [Internet]. Hoboken: Wiley; 2010. Available from: <http://site.ebrary.com/lib/academiccompletetitles/home.action>
86. Duling IN, editor. *Compact sources of ultrashort pulses*. Cambridge: Cambridge University Press; 1995. (Cambridge studies in modern optics; vol. 18).
87. Theodor P. Time-frequency analysis, by L. Cohen, Prentice Hall Signal Processing Series, Prentice Hall, Englewood Cliffs, New Jersey, 1995 - Book review. *Control Eng Pract.* 1997 Feb 1;5:292–4.
88. Hwang SI, Park SB, Mun J, Cho W, Nam CH, Kim KT. Generation of a single-cycle pulse using a two-stage compressor and its temporal characterization using a tunnelling ionization method. *Sci Rep.* 2019 Feb 7;9(1):1613.
89. Träger F. *Springer Handbook of Lasers and Optics*. Springer Science & Business Media; 2012. 1704 p.
90. Weber HP. Method for Pulsewidth Measurement of Ultrashort Light Pulses Generated by Phase-Locked Lasers using Nonlinear Optics. *J Appl Phys.* 1967 Apr 1;38(5):2231–4.
91. Giordmaine JA, Rentzepis PM, Shapiro SL, Wecht KW. Two-Photon Excitation of Fluorescence by Picosecond Light Pulses. *Appl Phys Lett.* 1967 Oct 1;11:216–8.
92. Shapiro SL. SECOND HARMONIC GENERATION IN LiNbO₃ BY PICOSECOND PULSES. *Appl Phys Lett.* 1968 Jul 1;13(1):19–21.
93. Auston DH. Measurement of picosecond pulse shape and background level. *Appl Phys Lett.* 1971 Mar 15;18(6):249–51.
94. Sala K, Kenney-Wallace G, Hall G. CW autocorrelation measurements of picosecond laser pulses. *IEEE J Quantum Electron.* 1980 Sep;16(9):990–6.
95. Akutowicz EJ. On the determination of the phase of a Fourier integral. II. *Proc Am Math Soc.* 1957;8(2):234.

96. Peatross J, Rundquist A. Temporal decorrelation of short laser pulses. *J Opt Soc Am B*. 1998;15(1):216.
97. Qian S, Chen D. Joint time-frequency analysis: Methods and applications. Upper Saddle River, NJ: Prentice Hall PTR; 1996.
98. Cohen L. Time-frequency distributions-a review. *Proc IEEE*. 1989 Jul;77(7):941–81.
99. Kane DJ, Trebino R. Characterization of arbitrary femtosecond pulses using frequency-resolved optical gating. *IEEE J Quantum Electron*. 1993 Feb;29(2):571–9.
100. DeLong KW, Fittinghoff DN, Trebino R, Kohler B, Wilson K. Pulse retrieval in frequency-resolved optical gating based on the method of generalized projections. *Opt Lett*. 1994 Dec 15;19(24):2152–4.
101. Jafari R, Jones T, Trebino R. 100% reliable algorithm for second-harmonic-generation frequency-resolved optical gating. *Opt Express*. 2019 Feb 4;27(3):2112–24.
102. Sweetser JN, Fittinghoff DN, Trebino R. Transient-grating frequency-resolved optical gating. *Opt Lett*. 1997 Apr 15;22(8):519–21.
103. Zipfel WR, Williams RM, Webb WW. Nonlinear magic: multiphoton microscopy in the biosciences. *Nat Biotechnol*. 2003 Nov;21(11):1369–77.
104. SHG Microscopy and Its Comparison with THG, CARS, and Multiphoton Excited Fluorescence Imaging - Second Harmonic Generation Imaging - page 81 [Internet]. [cited 2020 Nov 4]. Available from: <http://what-when-how.com/Tutorial/topic-5i5p4f/Second-Harmonic-Generation-Imaging-102.html>
105. SECOND HARMONIC GENERATION IMAGING. [S.l.]: CRC PRESS; 2019.
106. Society NG. Microscopes [Internet]. National Geographic Society. 2019 [cited 2020 Dec 30]. Available from: <http://www.nationalgeographic.org/encyclopedia/microscopes/>
107. SIMPLE MICROSCOPES [Internet]. [cited 2020 Dec 30]. Available from: <https://www.microscope-antiques.com/simple.html>
108. Microscope [Internet]. DK Find Out! [cited 2020 Dec 30]. Available from: <https://www.dkfindout.com/uk/science/amazing-inventions/microscope/>
109. Di Gianfrancesco A. Technologies for chemical analyses, microstructural and inspection investigations. In: *Materials for Ultra-Supercritical and Advanced Ultra-Supercritical Power Plants* [Internet]. Elsevier; 2017 [cited 2020 Nov 4]. p. 197–245. Available from: <https://linkinghub.elsevier.com/retrieve/pii/B9780081005521000087>
110. Rd A, Gb D, G N. The zeiss-Nomarski differential interference equipment for transmitted-light microscopy. *Z Wiss Mikrosk Mikrosk Tech*. 1969 Nov 1;69(4):193–221.
111. Maurer C, Jesacher A, Bernet S, Ritsch-Marte M. Phase contrast microscopy with full numerical aperture illumination. *Opt Express*. 2008 Nov 24;16(24):19821.

112. Polarization recovery through scattering media | Science Advances [Internet]. [cited 2020 Nov 4]. Available from: <https://advances.sciencemag.org/content/3/9/e1600743>
113. Zernike F. How I Discovered Phase Contrast. *Science*. 1955 Mar 11;121(3141):345–9.
114. Kumar V, Coluccelli N, Polli D. Chapter 5 - Coherent Optical Spectroscopy/Microscopy and Applications. In: Gupta VP, editor. *Molecular and Laser Spectroscopy* [Internet]. Elsevier; 2018 [cited 2020 Dec 30]. p. 87–115. Available from: <http://www.sciencedirect.com/science/article/pii/B978012849883500005X>
115. Elementary processes with two quantum transitions - Göppert-Mayer - 2009 - *Annalen der Physik* - Wiley Online Library [Internet]. [cited 2020 Dec 27]. Available from: <https://onlinelibrary.wiley.com/doi/epdf/10.1002/andp.200910358>
116. Über Elementarakte mit zwei Quantensprüngen - Göppert-Mayer - 1931 - *Annalen der Physik* - Wiley Online Library [Internet]. [cited 2020 Dec 27]. Available from: <https://onlinelibrary.wiley.com/doi/abs/10.1002/andp.19314010303>
117. Kaiser W, Garrett CGB. Two-Photon Excitation in $\text{Ca}\{\text{F}\}_2$: Eu^{2+} . *Phys Rev Lett*. 1961 Sep 15;7(6):229–31.
118. Hsieh C-L, Hsieh C-L, Grange R, Pu Y, Pu Y, Psaltis D, Psaltis D. Harmonic Holography. In: *Advances in Imaging* (2009), paper DTuA1 [Internet]. Optical Society of America; 2009 [cited 2020 Dec 26]. p. DTuA1. Available from: <https://www.osapublishing.org/abstract.cfm?uri=DH-2009-DTuA1>
119. Masters BR, So PT, Gratton E. Multiphoton excitation fluorescence microscopy and spectroscopy of in vivo human skin. *Biophys J*. 1997 Jun;72(6):2405–12.
120. So PT, Dong CY, Masters BR, Berland KM. Two-photon excitation fluorescence microscopy. *Annu Rev Biomed Eng*. 2000;2:399–429.
121. OSA | Confocal microscopy and multi-photon excitation microscopy of human skin in vivo [Internet]. [cited 2020 Dec 26]. Available from: <https://www.osapublishing.org/oe/fulltext.cfm?uri=oe-8-1-2&id=63565>
122. Denk W, Strickler JH, Webb WW. Two-photon laser scanning fluorescence microscopy. *Science*. 1990;248(4951):73–6.
123. Ragan TM, Huang H, So PTC. [22]In Vivo and ex Vivo tissue applications of two-photon microscopy. In: *Methods in Enzymology* [Internet]. Academic Press; 2003 [cited 2020 Dec 26]. p. 481–505. (Biophotonics, Part B; vol. 361). Available from: <http://www.sciencedirect.com/science/article/pii/S0076687903610244>
124. Sandison DR, Williams RM, Wells KS, Strickler J, Webb WW. Quantitative Fluorescence Confocal Laser Scanning Microscopy (CLSM). In: Pawley JB, editor. *Handbook of Biological Confocal Microscopy* [Internet]. Boston, MA: Springer US; 1995 [cited 2020 Dec 26]. p. 39–53. Available from: https://doi.org/10.1007/978-1-4757-5348-6_3
125. Hanson KM, Bardeen CJ. Application of nonlinear optical microscopy for imaging skin. *Photochem Photobiol*. 2009 Feb;85(1):33–44.

126. Sheppard CJR, Kompfner R. Resonant scanning optical microscope. *Appl Opt.* 1978 Sep 15;17(18):2879–82.
127. Duncan MD, Reintjes J, Manuccia TJ. Scanning coherent anti-Stokes Raman microscope. *Opt Lett.* 1982 Aug 1;7(8):350–2.
128. Svoboda K, Tank DW, Denk W. Direct measurement of coupling between dendritic spines and shafts. *Science.* 1996 May 3;272(5262):716–9.
129. Yuste R, Denk W. Dendritic spines as basic functional units of neuronal integration. *Nature.* 1995 Jun;375(6533):682–4.
130. Svoboda K, Denk W, Kleinfeld D, Tank DW. In vivo dendritic calcium dynamics in neocortical pyramidal neurons. *Nature.* 1997 Jan;385(6612):161–5.
131. Ladewig T, Kloppenburg P, Lalley PM, Zipfel WR, Webb WW, Keller BU. Spatial profiles of store-dependent calcium release in motoneurons of the nucleus hypoglossus from newborn mouse. *J Physiol.* 2003 Mar 15;547(Pt 3):775–87.
132. Balu M, Baldacchini T, Carter J, Krasieva TB, Zadoyan R, Tromberg BJ. Effect of excitation wavelength on penetration depth in nonlinear optical microscopy of turbid media. *J Biomed Opt.* 2009 Feb;14(1):010508.
133. Hellwarth R, Christensen P. Nonlinear optical microscopic examination of structure in polycrystalline ZnSe. *Opt Commun.* 1974 Nov 1;12(3):318–22.
134. Second-harmonic imaging in the scanning optical microscope | SpringerLink [Internet]. [cited 2020 Dec 27]. Available from: <https://link.springer.com/article/10.1007/BF00620308>
135. Freund I, Deutsch M. Second-harmonic microscopy of biological tissue. *Opt Lett.* 1986 Feb 1;11(2):94–6.
136. Tai S-P, Tsai T-H, Lee W-J, Shieh D-B, Liao Y-H, Huang H-Y, Zhang K, Liu H-L, Sun C-K. Optical biopsy of fixed human skin with backward-collected optical harmonics signals. *Opt Express.* 2005 Oct 3;13(20):8231–42.
137. Zoumi A, Lu X, Kassab GS, Tromberg BJ. Imaging coronary artery microstructure using second-harmonic and two-photon fluorescence microscopy. *Biophys J.* 2004 Oct;87(4):2778–86.
138. Theodossiou TA, Thrasivoulou C, Ekwobi C, Becker DL. Second harmonic generation confocal microscopy of collagen type I from rat tendon cryosections. *Biophys J.* 2006 Dec 15;91(12):4665–77.
139. Yeh AT, Choi B, Nelson JS, Tromberg BJ. Reversible dissociation of collagen in tissues. *J Invest Dermatol.* 2003 Dec;121(6):1332–5.
140. Stoller P, Kim B-M, Rubenchik AM, Reiser KM, Da Silva LB. Polarization-dependent optical second-harmonic imaging of a rat-tail tendon. *J Biomed Opt.* 2002 Apr;7(2):205–14.
141. P S, Km R, Pm C, Am R. Polarization-modulated second harmonic generation in collagen. *Biophys J.* 2002 Jun 1;82(6):3330–42.

142. Lin S-J, Jee S-H, Kuo C-J, Wu R-J, Lin W-C, Chen J-S, Liao Y-H, Hsu C-J, Tsai T-F, Chen Y-F, Dong C-Y. Discrimination of basal cell carcinoma from normal dermal stroma by quantitative multiphoton imaging. *Opt Lett*. 2006 Sep 15;31(18):2756–8.
143. Han M, Giese G, Bille J. Second harmonic generation imaging of collagen fibrils in cornea and sclera. *Opt Express*. 2005 Jul 25;13(15):5791–7.
144. Han M, Zickler L, Giese G, Walter M, Loesel FH, Bille JF. Second-harmonic imaging of cornea after intrastromal femtosecond laser ablation. *J Biomed Opt*. 2004 Aug;9(4):760–6.
145. Cox G, Kable E, Jones A, Fraser I, Manconi F, Gorrell MD. 3-dimensional imaging of collagen using second harmonic generation. *J Struct Biol*. 2003 Jan;141(1):53–62.
146. Pena A-M, Fabre A, Débarre D, Marchal-Somme J, Crestani B, Martin J-L, Beaurepaire E, Schanne-Klein M-C. Three-dimensional investigation and scoring of extracellular matrix remodeling during lung fibrosis using multiphoton microscopy. *Microsc Res Tech*. 2007 Feb;70(2):162–70.
147. Drury JL, Mooney DJ. Hydrogels for tissue engineering: scaffold design variables and applications. *Biomaterials*. 2003 Nov;24(24):4337–51.
148. Odin C, Le Grand Y, Renault A, Gailhouste L, Baffet G. Orientation fields of nonlinear biological fibrils by second harmonic generation microscopy. *J Microsc*. 2008 Jan;229(Pt 1):32–8.
149. Kwon GP, Schroeder JL, Amar MJ, Remaley AT, Balaban RS. Contribution of macromolecular structure to the retention of low-density lipoprotein at arterial branch points. *Circulation*. 2008 Jun 3;117(22):2919–27.
150. Campagnola PJ, Loew LM. Second-harmonic imaging microscopy for visualizing biomolecular arrays in cells, tissues and organisms. *Nat Biotechnol*. 2003;21(11):1356–60.
151. Sutherland RL, McLean DG, Kirkpatrick S. *Handbook of nonlinear optics*. 2nd ed., rev.expanded. New York: Marcel Dekker; 2003. 971 p. (Optical engineering).
152. Bancelin S, Vigne S, Hossain N, Chaker M, Légaré F. Nonlinear optical properties of calcium barium niobate epitaxial thin films. *Opt Express*. 2016 Jul 25;24(15):17497–504.
153. Roth S, Freund I. Second harmonic generation in collagen. 1979;
154. Gusachenko I, Tran V, Houssen YG, Allain J-M, Schanne-Klein M-C. Polarization-Resolved Second-Harmonic Generation in Tendon upon Mechanical Stretching. *Biophys J*. 2012 May 2;102(9):2220–9.
155. Campagnola PJ, Millard AC, Terasaki M, Hoppe PE, Malone CJ, Mohler WA. Three-Dimensional High-Resolution Second-Harmonic Generation Imaging of Endogenous Structural Proteins in Biological Tissues. *Biophys J*. 2002 Jan 1;82(1):493–508.
156. Zipfel WR, Williams RM, Christie R, Nikitin AY, Hyman BT, Webb WW. Live tissue intrinsic emission microscopy using multiphoton-excited native fluorescence and second harmonic generation. *Proc Natl Acad Sci U S A*. 2003 Jun 10;100(12):7075–80.

157. Strupler M, Pena A-M, Hernest M, Tharaux P-L, Martin J-L, Beaurepaire E, Schanne-Klein M-C. Second harmonic imaging and scoring of collagen in fibrotic tissues. *Opt Express*. 2007 Apr 2;15(7):4054–65.
158. Deniset-Besseau A, De Sa Peixoto P, Mosser G, Schanne-Klein M-C. Nonlinear optical imaging of lyotropic cholesteric liquid crystals. *Opt Express*. 2010 Jan 18;18(2):1113–21.
159. Kumar R, Grønhaug KM, Romijn EI, Finnøy A, Davies CL, Drogset JO, Lilledahl MB. Polarization second harmonic generation microscopy provides quantitative enhanced molecular specificity for tissue diagnostics. *J Biophotonics*. 2015 Sep;8(9):730–9.
160. Brideau C, Stys PK. Automated control of optical polarization for nonlinear microscopy. In: Periasamy A, König K, So PTC, editors. *Multiphoton Microscopy in the Biomedical Sciences XII*. SPIE; 2012. p. 82263A. (SPIE Proceedings).
161. Keijzer M, Richards-Kortum RR, Jacques SL, Feld MS. Fluorescence spectroscopy of turbid media: Autofluorescence of the human aorta. *Appl Opt*. 1989 Oct 15;28(20):4286–92.
162. Mertz J, Moreaux L. Second-harmonic generation by focused excitation of inhomogeneously distributed scatterers. *Opt Commun*. 2001 Sep 1;196(1):325–30.
163. Moreaux L, Sandre O, Mertz J. Membrane imaging by second-harmonic generation microscopy. *JOSA B*. 2000 Oct 1;17(10):1685–94.
164. Chu S-W, Tai S-P, Liu T-M, Sun C-K, Lin C-H. Selective imaging in second-harmonic-generation microscopy with anisotropic radiation. *J Biomed Opt*. 2009 Jan;14(1):010504.
165. Cheng J-X, Xie XS. Green's function formulation for third-harmonic generation microscopy. *JOSA B*. 2002 Jul 1;19(7):1604–10.
166. Moreaux L, Sandre O, Charpak S, Blanchard-Desce M, Mertz J. Coherent Scattering in Multi-Harmonic Light Microscopy. *Biophys J*. 2001 Mar 1;80(3):1568–74.
167. OSA | The structural origin of second harmonic generation in fascia [Internet]. [cited 2020 Dec 28]. Available from: <https://www.osapublishing.org/boe/fulltext.cfm?uri=boe-2-1-26&id=208482>
168. Rivard M. *Imagerie tissulaire par microscopie de seconde harmonique interférométrique*. INRS EMT; 2015.
169. Green NH, Delaine-Smith R, Askew HJ, Byers R, Reilly GC, Matcher SJ. A new mode of contrast in biological second harmonic generation microscopy. *Sci Rep* [Internet]. 2017 Oct 17 [cited 2020 Dec 28];7. Available from: <https://doi.org/10.1038/s41598-017-13752-y>
170. Millard AC, Campagnola PJ, Mohler W, Lewis A, Loew LM. [3] Second harmonic imaging microscopy. In: Marriott G, Parker I, editors. *Biophotonics*. Amsterdam and London: Academic Press; 2003. p. 47–69. (Methods in Enzymology; vol. 361).
171. Bancelin S, Couture C-A, Légaré K, Pinsard M, Rivard M, Brown C, Légaré F. Fast interferometric second harmonic generation microscopy. *Biomed Opt Express*. 2016 Feb 1;7(2):399–408.

172. Pinsard M, Schmeltz M, Kolk J van der, Patten SA, Ibrahim H, Ramunno L, Schanne-Klein M-C, Légaré F. Elimination of imaging artifacts in second harmonic generation microscopy using interferometry. *Biomed Opt Express*. 2019 Aug 1;10(8):3938–52.
173. Pinsard M, Belley L-P, Piau J-M, Coté C-Y, Ibrahim H, Légaré F. Single-scan interferometric second harmonic generation microscopy using a kHz phase-scanner. *Opt Express*. 2019 Dec 23;27(26):38435–50.
174. Schlom DG, Chen L-Q, Eom C-B, Rabe KM, Streiffer SK, Triscone J-M. Strain Tuning of Ferroelectric Thin Films. *Annu Rev Mater Res*. 2007;37(1):589–626.
175. Haeni JH, Irvin P, Chang W, Uecker R, Reiche P, Li YL, Choudhury S, Tian W, Hawley ME, Craigo B, Tagantsev AK, Pan XQ, Streiffer SK, Chen LQ, Kirchoefer SW, Levy J, Schlom DG. Room-temperature ferroelectricity in strained SrTiO₃. *Nature*. 2004 Aug 12;430(7001):758–61.
176. Joshi PC, Krupanidhi SB. Structural and electrical characteristics of SrTiO₃ thin films for dynamic random access memory applications. *J Appl Phys*. 1993 Jun 1;73(11):7627–34.
177. Saad MM, Baxter P, Bowman RM, Gregg JM, Morrison FD, Scott JF. Intrinsic dielectric response in ferroelectric nano-capacitors. *J Phys Condens Matter*. 2004 Oct;16(41):L451–6.
178. Mk H, Y Z, N J, D M, Y Z, R V, S P. BaTiO₃ integration with nanostructured epitaxial (100), (110), and (111) germanium for multifunctional devices. *ACS Appl Mater Interfaces*. 2013 Nov 1;5(21):11446–52.
179. Grabowska E. Selected perovskite oxides: Characterization, preparation and photocatalytic properties—A review. *Appl Catal B Environ*. 2016;186:97–126.
180. Kolhatkar G, Nicklaus M, Hadj Youssef A, Cojocar C, Rivard M, Merlen A, Légaré F, Ruediger A. Second Harmonic Generation Investigation of Symmetry Breaking and Flexoelectricity Induced by Nanoindentations in SrTiO₃. *Adv Funct Mater*. 2019;29(36):1901266.
181. Nova TF, Disa AS, Fechner M, Cavalleri A. Metastable ferroelectricity in optically strained SrTiO₃. *Science*. 2019;364(6445):1075–9.
182. Sun F, Khassaf H, Alpay SP. Strain engineering of piezoelectric properties of strontium titanate thin films. *J Mater Sci*. 2014;49(17):5978–85.
183. Hadj Youssef A, Zhang J, Ehteshami A, Kolhatkar G, Dab C, Berthomieu D, Merlen A, Légaré F, Ruediger A. Symmetry-Forbidden-Mode Detection in SrTiO₃ Nanoislands with Tip-Enhanced Raman Spectroscopy. *J Phys Chem C [Internet]*. 2021 Mar 11 [cited 2021 Mar 14]; Available from: <https://doi.org/10.1021/acs.jpcc.0c10938>
184. Ross JS, Wu S, Yu H, Ghimire NJ, Jones AM, Aivazian G, Yan J, Mandrus DG, Xiao D, Yao W, Xu X. Electrical control of neutral and charged excitons in a monolayer semiconductor. *Nat Commun*. 2013 Feb 12;4(1):1474.
185. Wang Y, Xiao J, Zhu H, Li Y, Alsaïd Y, Fong KY, Zhou Y, Wang S, Shi W, Wang Y, Zettl A, Reed EJ, Zhang X. Structural phase transition in monolayer MoTe₂ driven by electrostatic doping. *Nature*. 2017 Oct;550(7677):487–91.

186. Novoselov KS, Jiang D, Schedin F, Booth TJ, Khotkevich VV, Morozov SV, Geim AK. Two-dimensional atomic crystals. *Proc Natl Acad Sci*. 2005 Jul 26;102(30):10451–3.
187. Novoselov KS, Geim AK, Morozov SV, Jiang D, Zhang Y, Dubonos SV, Grigorieva IV, Firsov AA. Electric Field Effect in Atomically Thin Carbon Films. *Science*. 2004 Oct 22;306(5696):666–9.
188. Wang Y, Xiao J, Yang S, Wang Y, Zhang X. Second harmonic generation spectroscopy on two-dimensional materials [Invited]. *Opt Mater Express*. 2019;9(3):1136.
189. Anasori B, Lukatskaya MR, Gogotsi Y. 2D metal carbides and nitrides (MXenes) for energy storage. *Nat Rev Mater*. 2017 Jan 17;2(2):1–17.
190. Kostarelos K. Translating graphene and 2D materials into medicine. 2016;
191. Wang T, Xu Y-Q. Photonic Structure-Integrated Two-Dimensional Material Optoelectronics. *Electronics*. 2016 Dec;5(4):93.
192. Tang L, Meng X, Deng D, Bao X. Confinement Catalysis with 2D Materials for Energy Conversion. *Adv Mater Deerfield Beach Fla*. 2019 Dec;31(50):e1901996.
193. Wagoner GA, Persans PD, van Wagenen EA, Korenowski GM. Second-harmonic generation in molybdenum disulfide. *J Opt Soc Am B*. 1998;15(3):1017.
194. Zhou L, Fu H, Lv T, Wang C, Gao H, Li D, Deng L, Xiong W. Nonlinear Optical Characterization of 2D Materials. *Nanomaterials*. 2020 Nov;10(11):2263.
195. Wang QH, Kalantar-Zadeh K, Kis A, Coleman JN, Strano MS. Electronics and optoelectronics of two-dimensional transition metal dichalcogenides. *Nat Nanotechnol*. 2012 Nov;7(11):699–712.
196. Radisavljevic B, Radenovic A, Brivio J, Giacometti V, Kis A. Single-layer MoS₂ transistors. *Nat Nanotechnol*. 2011 Mar;6(3):147–50.
197. Mak KF, He K, Lee C, Lee GH, Hone J, Heinz TF, Shan J. Tightly bound trions in monolayer MoS₂. *Nat Mater*. 2013 Mar;12(3):207–11.
198. Ramasubramaniam A. Large excitonic effects in monolayers of molybdenum and tungsten dichalcogenides. *Phys Rev B*. 2012 Sep 6;86(11):115409.
199. Probing Symmetry Properties of Few-Layer MoS₂ and h-BN by Optical Second-Harmonic Generation | *Nano Letters* [Internet]. [cited 2020 Dec 18]. Available from: <https://pubs.acs.org/doi/10.1021/nl401561r>
200. *Phys. Rev. B* 87, 201401(R) (2013) - Observation of intense second harmonic generation from MoS₂ atomic crystals [Internet]. [cited 2020 Dec 28]. Available from: <https://journals.aps.org/prb/abstract/10.1103/PhysRevB.87.201401>
201. Kumar N, Najmaei S, Cui Q, Ceballos F, Ajayan PM, Lou J, Zhao H. Second harmonic microscopy of monolayer MoS₂. *Phys Rev B*. 2013 Apr 15;87(16):161403.
202. Song Y, Hu S, Lin M-L, Gan X, Tan P, Zhao J. Extraordinary Second Harmonic Generation in ReS₂ Atomic Crystals. 2018;

203. Wen X, Gong Z, Li D. Nonlinear optics of two-dimensional transition metal dichalcogenides. *InfoMat*. 2019;1(3):317–37.
204. Song Y, Tian R, Yang J, Yin R, Zhao J, Gan X. Second harmonic generation in atomically thin MoTe₂ [Internet]. 2018. Available from: <https://arxiv.org/pdf/1805.09489>
205. Zeng H, Liu G-B, Dai J, Yan Y, Zhu B, He R, Xie L, Xu S, Chen X, Yao W, Cui X. Optical signature of symmetry variations and spin-valley coupling in atomically thin tungsten dichalcogenides. *Sci Rep* [Internet]. 2013 Apr 11 [cited 2021 Jan 3];3. Available from: <https://www.ncbi.nlm.nih.gov/pmc/articles/PMC3622914/>
206. Li D, Xiong W, Jiang L, Xiao Z, Golgir HR, Wang M, Huang X, Zhou Y, Lin Z, Song J, Ducharme S, Jiang L, Silvain JF, Lu Y. Multimodal Nonlinear Optical Imaging of MoS₂ and MoS₂-Based van der Waals Heterostructures. *ACS Nano*. 2016 Mar 22;10(3):3766–75.
207. Li BJ. 2 - Electro-optical switches. In: Li B, Chua SJ, editors. *Optical Switches* [Internet]. Woodhead Publishing; 2010 [cited 2020 Nov 20]. p. 5-e8. (Woodhead Publishing Series in Electronic and Optical Materials). Available from: <http://www.sciencedirect.com/science/article/pii/B9781845695798500024>
208. Li Y, Duerloo K-AN, Wauson K, Reed EJ. Structural semiconductor-to-semimetal phase transition in two-dimensional materials induced by electrostatic gating. *Nat Commun*. 2016 Feb 12;7(1):10671.
209. Superconducting Dome in a Gate-Tuned Band Insulator | *Science* [Internet]. [cited 2021 Jan 6]. Available from: <https://science.sciencemag.org/content/338/6111/1193>
210. Patra N, Wang B, Král P. Nanodroplet Activated and Guided Folding of Graphene Nanostructures. *Nano Lett*. 2009 Nov 11;9(11):3766–71.
211. Zhu S, Galginaitis J, Li T. Critical Dispersion Distance of Silicon Nanoparticles Intercalated between Graphene Layers. *J Nanomater* [Internet]. 2012;2012. Available from: <https://www.hindawi.com/journals/jnm/2012/375289/>
212. Braga SF, Coluci VR, Legoas SB, Giro R, Galvão DS, Baughman RH. Structure and Dynamics of Carbon Nanoscrolls. *Nano Lett*. 2004 May 1;4(5):881–4.
213. Zhang Z, Li T. Carbon nanotube initiated formation of carbon nanoscrolls. *Appl Phys Lett*. 2010 Aug 23;97(8):081909.
214. Yu D, Liu F. Synthesis of Carbon Nanotubes by Rolling up Patterned Graphene Nanoribbons Using Selective Atomic Adsorption. *Nano Lett*. 2007 Oct 1;7(10):3046–50.
215. Zhang Z, Li T. Ultrafast nano-oscillators based on interlayer-bridged carbon nanoscrolls. *Nanoscale Res Lett*. 2011 Jul 25;6(1):470.
216. Xie X, Ju L, Feng X, Sun Y, Zhou R, Liu K, Fan S, Li Q, Jiang K. Controlled Fabrication of High-Quality Carbon Nanoscrolls from Monolayer Graphene. *Nano Lett*. 2009 Jul 8;9(7):2565–70.
217. Shuze Zhu, Teng Li. Hydrogenation enabled scrolling of graphene. *J Phys Appl Phys*. 2013;46(7):075301.

218. Li S-L, Tsukagoshi K, Orgiu E, Samori P. Charge transport and mobility engineering in two-dimensional transition metal chalcogenide semiconductors. *Chem Soc Rev.* 2016;45(1):118–51.
219. Dean CR, Wang L, Maher P, Forsythe C, Ghahari F, Gao Y, Katoch J, Ishigami M, Moon P, Koshino M, Taniguchi T, Watanabe K, Shepard KL, Hone J, Kim P. Hofstadter’s butterfly and the fractal quantum Hall effect in moiré superlattices. *Nature.* 2013 May 30;497(7451):598–602.
220. Ponomarenko LA, Gorbachev RV, Yu GL, Elias DC, Jalil R, Patel AA, Mishchenko A, Mayorov AS, Woods CR, Wallbank JR, Mucha-Kruczynski M, Piot BA, Potemski M, Grigorieva IV, Novoselov KS, Guinea F, Fal’ko VI, Geim AK. Cloning of Dirac fermions in graphene superlattices. *Nature.* 2013 May 30;497(7451):594–7.
221. Gorbachev RV, Song JCW, Yu GL, Kretinin AV, Withers F, Cao Y, Mishchenko A, Grigorieva IV, Novoselov KS, Levitov LS, Geim AK. Detecting topological currents in graphene superlattices. *Science.* 2014 Oct 24;346(6208):448–51.
222. Hunt B, Sanchez-Yamagishi JD, Young AF, Yankowitz M, LeRoy BJ, Watanabe K, Taniguchi T, Moon P, Koshino M, Jarillo-Herrero P, Ashoori RC. Massive Dirac fermions and Hofstadter butterfly in a van der Waals heterostructure. *Science.* 2013 Jun 21;340(6139):1427–30.
223. Lee C-H, Lee G-H, van der Zande AM, Chen W, Li Y, Han M, Cui X, Arefe G, Nuckolls C, Heinz TF, Guo J, Hone J, Kim P. Atomically thin p-n junctions with van der Waals heterointerfaces. *Nat Nanotechnol.* 2014 Sep;9(9):676–81.
224. Furchi MM, Pospischil A, Libisch F, Burgdörfer J, Mueller T. Photovoltaic effect in an electrically tunable van der Waals heterojunction. *Nano Lett.* 2014 Aug 13;14(8):4785–91.
225. A. Avsar, J. Y. Tan, T. Taychatanapat, J. Balakrishnan, G.K.W. Koon, Y. Yeo, J. Lahiri, A. Carvalho, A. S. Rodin, E.C.T. O’Farrell, G. Eda, A. H. Castro Neto, B. Özyilmaz. Spin–orbit proximity effect in graphene. *Nat Commun.* 5(1):1–6.
226. Wang Z, Ki D-K, Chen H, Berger H, MacDonald AH, Morpurgo AF. Strong interface-induced spin-orbit interaction in graphene on WS₂. *Nat Commun.* 2015 Sep 22;6:8339.
227. Yan W, Txoperena O, Llopis R, Dery H, Hueso LE, Casanova F. A two-dimensional spin field-effect switch. *Nat Commun* [Internet]. 2016 Nov 11 [cited 2021 Jan 3];7(1). Available from: <https://nottingham-repository.worktribe.com/output/3084918/a-two-dimensional-spin-field-effect-switch>
228. Ashton M, Paul J, Sinnott SB, Hennig RG. Topology-Scaling Identification of Layered Solids and Stable Exfoliated 2D Materials. *Phys Rev Lett.* 2017 Mar 7;118(10):106101.
229. Oligothiophene-Functionalized Perylene Bisimide System: Synthesis, Characterization, and Electrochemical Polymerization Properties | *Chemistry of Materials* [Internet]. [cited 2020 Nov 19]. Available from: <https://pubs.acs.org/doi/abs/10.1021/cm048642z>
230. Wu W, Liu Y, Zhu D. π -Conjugated molecules with fused rings for organic field-effect transistors: design, synthesis and applications. *Chem Soc Rev.* 2010 Apr 26;39(5):1489–502.
231. Molecular Design and Ordering Effects in π -Functional Materials for Transistor and Solar Cell Applications | *Journal of the American Chemical Society* [Internet]. [cited 2020 Nov 19]. Available from: <https://pubs.acs.org/doi/10.1021/ja2073643>

232. Liu F, Chow WL, He X, Hu P, Zheng S, Wang X, Zhou J, Fu Q, Fu W, Yu P, Zeng Q, Fan HJ, Tay BK, Kloc C, Liu Z. Van der Waals p–n Junction Based on an Organic–Inorganic Heterostructure. *Adv Funct Mater.* 2015;25(36):5865–71.
233. Vélez S, Ciudad D, Island J, Buscema M, Txoperena O, Parui S, Steele GA, Casanova F, Zant HSJ van der, Castellanos-Gomez A, Hueso LE. Gate-tunable diode and photovoltaic effect in an organic–2D layered material p–n junction. *Nanoscale.* 2015 Sep 21;7(37):15442–9.
234. Jariwala D, Howell SL, Chen KS, Kang J, Sangwan VK, Filippone SA, Turrisi R, Marks TJ, Lauhon LJ, Hersam MC. Hybrid, Gate-Tunable, van der Waals p-n Heterojunctions from Pentacene and MoS₂. *Nano Lett.* 2016 Jan 13;16(1):497–503.
235. Shih C-J, Pfattner R, Chiu Y-C, Liu N, Lei T, Kong D, Kim Y, Chou H-H, Bae W-G, Bao Z. Partially-Screened Field Effect and Selective Carrier Injection at Organic Semiconductor/Graphene Heterointerface. *Nano Lett.* 2015 Nov 11;15(11):7587–95.
236. Ojeda-Aristizabal C, Bao W, Fuhrer MS. Thin-film barristor: A gate-tunable vertical graphene-pentacene device. *Phys Rev B.* 2013 Jul 22;88(3):035435.
237. H H, Ch K, F C, Cy N, Ra B, N P, J H, I K. Low-voltage organic electronics based on a gate-tunable injection barrier in vertical graphene-organic semiconductor heterostructures. *Nano Lett.* 2014 Dec 30;15(1):69–74.
238. Energy Barriers: Gate-Controlled Energy Barrier at a Graphene/Molecular Semiconductor Junction (*Adv. Funct. Mater.* 20/2015) - Parui - 2015 - *Advanced Functional Materials* - Wiley Online Library [Internet]. [cited 2021 Jan 3]. Available from: <https://onlinelibrary.wiley.com/doi/abs/10.1002/adfm.201570137>
239. Structural and Electrical Investigation of C60–Graphene Vertical Heterostructures | *ACS Nano* [Internet]. [cited 2021 Jan 3]. Available from: <https://pubs.acs.org/doi/abs/10.1021/acsnano.5b00581>
240. The Correct Material for Infrared (IR) Applications [Internet]. [cited 2020 Dec 28]. Available from: <https://www.edmundoptics.com/knowledge-center/application-notes/optics/the-correct-material-for-infrared-applications/>
241. Universal mechanical exfoliation of large-area 2D crystals | *Nature Communications* [Internet]. [cited 2020 Nov 17]. Available from: <https://www.nature.com/articles/s41467-020-16266-w>
242. Characterization of Few-Layer 1T' MoTe₂ by Polarization-Resolved Second Harmonic Generation and Raman Scattering | *ACS Nano* [Internet]. [cited 2020 Nov 17]. Available from: <https://pubs.acs.org/doi/10.1021/acsnano.6b05127>
243. Hu L, Shan X, Wu Y, Zhao J, Lu X. Laser Thinning and Patterning of MoS₂ with Layer-by-Layer Precision. *Sci Rep.* 2017 Nov 14;7(1):15538.
244. Malard LM, Alencar TV, Barboza APM, Mak KF, de Paula AM. Observation of intense second harmonic generation from MoS₂ atomic crystals. *Phys Rev B.* 2013 May 13;87(20):201401.
245. Balla NK, O'Brien M, McEvoy N, Duesberg GS, Rigneault H, Brasselet S, McCloskey D. Effects of Excitonic Resonance on Second and Third Order Nonlinear Scattering from Few-Layer MoS₂. *ACS Photonics.* 2018 Apr 18;5(4):1235–40.

246. Mennel L, Paur M, Mueller T. Second harmonic generation in strained transition metal dichalcogenide monolayers: MoS₂, MoSe₂, WS₂, and WSe₂. *APL Photonics*. 2018 Dec 12;4(3):034404.
247. Segmented terahertz electron accelerator and manipulator (STEAM) | *Nature Photonics* [Internet]. [cited 2020 Nov 27]. Available from: <https://www.nature.com/articles/s41566-018-0138-z>
248. Direct observation of attosecond light bunching | *Nature* [Internet]. [cited 2020 Nov 27]. Available from: <https://www.nature.com/articles/nature02091>
249. Relativistic-intensity near-single-cycle light waveforms at kHz repetition rate | *Light: Science & Applications* [Internet]. [cited 2020 Nov 27]. Available from: <https://www.nature.com/articles/s41377-020-0280-5>
250. Liu J-M, editor. Laser Oscillation. In: *Principles of Photonics* [Internet]. Cambridge: Cambridge University Press; 2016 [cited 2020 Dec 4]. p. 274–96. Available from: <https://www.cambridge.org/core/books/principles-of-photonics/laser-oscillation/EAE57C0DF25BCAC5FD21ECF4984F72C9>
251. Rullière C. *Femtosecond Laser Pulses: Principles and Experiments* [Internet]. 2. ed. [Online-Ausg.]. New York, NY: Springer Science+Business Media Inc; 2005. (Advanced texts in physics). Available from: <https://ebookcentral.proquest.com/lib/subhh/detail.action?docID=3062277>
252. Thyagarajan K, Ghatak A. *Lasers: Fundamentals and Applications* [Internet]. 2. ed. Boston, MA: Springer Science+Business Media LLC; 2010. (Graduate Texts in Physics). Available from: <http://site.ebrary.com/lib/alltitles/docDetail.action?docID=10421207>
253. Pessot M, Maine P, Mourou G. 1000 times expansion/compression of optical pulses for chirped pulse amplification. *Opt Commun*. 1987;62(6):419–21.
254. Basov N, Kertes I, Kryukov P, Matveets Y, Senatsky Y, chekalin sergey. Nonlinear Losses in Generators and Amplifiers of Ultrashort Light Pulses. *J Exp Theor Phys - J EXP THEOR PHYS*. 1971 Jan 1;33.
255. Basov N, Kryukov P, Senatsky Y, chekalin sergey. Production of Powerful Ultrashort Light Pulses in a Neodymium Glass Laser. *J Exp Theor Phys - J EXP THEOR PHYS*. 1970 Apr 1;10:641–5.
256. Zuegel JD. “Laser Fusion for Laser Jocks: Basic Principles and Laser Applications Meeting a Grand Challenge.” In: *Conference on Lasers and Electro-Optics 2010 (2010)*, paper AThA1 [Internet]. Optical Society of America; 2010 [cited 2021 Jan 14]. p. AThA1. Available from: https://www.osapublishing.org/abstract.cfm?uri=CLEO_Apps-2010-AThA1
257. Maine P, Strickland D, Bado P, Pessot M, Mourou G. Generation of ultrahigh peak power pulses by chirped pulse amplification. *IEEE J Quantum Electron*. 1988;24(2):398–403.
258. Treacy E. Optical pulse compression with diffraction gratings. *IEEE J Quantum Electron*. 1969;5(9):454–8.
259. Chirped Pulse Amplification – Center for Ultrafast Optical Science [Internet]. 2020. Available from: <https://cuos.engin.umich.edu/researchgroups/hfs/facilities/chirped-pulse-amplification/>

260. Timmers H, Kobayashi Y, Chang KF, Reduzzi M, Neumark DM, Leone SR. Generating high-contrast, near single-cycle waveforms with third-order dispersion compensation. *Opt Lett*. 2017 Feb 15;42(4):811–4.
261. Rl F, Oe M, Jp G. Negative dispersion using pairs of prisms [Internet]. Vol. 9, *Optics letters*. *Opt Lett*; 1984 [cited 2020 Dec 2]. Available from: <https://pubmed.ncbi.nlm.nih.gov/19721526/>
262. Martinez OE, Gordon JP, Fork RL. Negative group-velocity dispersion using refraction. *JOSA A*. 1984 Oct 1;1(10):1003–6.
263. Liao K-H, Cheng M-Y, Flecher E, Smirnov VI, Glebov LB, Galvanauskas A. Large-aperture chirped volume Bragg grating based fiber CPA system. *Opt Express*. 2007 Apr 16;15(8):4876–82.
264. Webster A. Useful Mathematical Formulas for Transform Limited Pulses. :13.
265. Yu TJ, Lee SK, Sung JH, Yoon JW, Jeong TM, Lee J. Generation of high-contrast, 30 fs, 1.5 PW laser pulses from chirped-pulse amplification Ti:sapphire laser. *Opt Express*. 2012 May 7;20(10):10807–15.
266. Shimizu F. Frequency Broadening in Liquids by a Short Light Pulse. *Phys Rev Lett*. 1967 Nov 6;19(19):1097–100.
267. Stolen RH, Lin C. Self-phase-modulation in silica optical fibers. *Phys Rev A*. 1978 Apr 1;17(4):1448–53.
268. Krausz F, Ivanov M. Attosecond physics. *Rev Mod Phys*. 2009 Feb 2;81(1):163–234.
269. Suda A, Hatayama M, Nagasaka K, Midorikawa K. Generation of sub-10-fs, 5-mJ-optical pulses using a hollow fiber with a pressure gradient. *Appl Phys Lett*. 2005 Mar 10;86(11):111116.
270. OSA | CEP stable 1.6 cycle laser pulses at 1.8 μm [Internet]. [cited 2021 Jan 18]. Available from: <https://www.osapublishing.org/oe/fulltext.cfm?uri=oe-19-7-6858&id=211312>
271. Cardin V, Thiré N, Beaulieu S, Wanie V, Légaré F, Schmidt BE. 0.42 TW 2-cycle pulses at 1.8 μm via hollow-core fiber compression. *Appl Phys Lett*. 2015 Nov 2;107(18):181101.
272. Fan G, Balčiūnas T, Kanai T, Flöry T, Andriukaitis G, Schmidt BE, Légaré F, Baltuška A. Hollow-core-waveguide compression of multi-millijoule CEP-stable 3.2 μm pulses. *Optica*. 2016 Dec 20;3(12):1308–11.
273. *Nonlinear Fiber Optics - 4th Edition* [Internet]. [cited 2020 Nov 27]. Available from: <https://www.elsevier.com/books/nonlinear-fiber-optics/agrawal/978-0-12-369516-1>
274. Dianov EM, Nikonova ZS, Serkin VN. Influence of optical losses on the dynamics of nonlinear propagation of pulses in single-mode fiber waveguides. *Sov J Quantum Electron*. 1986 Feb 28;16(2):219.
275. Akhmanov, Vysloukh VA, Chirkin AS. *Optics of Femtosecond Laser Pulses* [Internet]. AIP-Press; 1992 [cited 2020 Nov 27]. Available from: <https://www.springer.com/gp/book/9780883188514>

276. Alfano RR, editor. *The Supercontinuum Laser Source: Fundamentals with Updated References* [Internet]. 2nd ed. New York: Springer-Verlag; 2006 [cited 2020 Nov 27]. Available from: <https://www.springer.com/gp/book/9781441920324>
277. Agrawal GP. *Nonlinear Fiber Optics: Formerly Quantum Electronics*. Academic Press; 2013. 612 p.
278. DeMartini F, Townes CH, Gustafson TK, Kelley PL. Self-Steepening of Light Pulses. *Phys Rev*. 1967 Dec 10;164(2):312–23.
279. Grischkowsky D, Courtens E, Armstrong JA. Observation of Self-Steepening of Optical Pulses with Possible Shock Formation. *Phys Rev Lett*. 1973 Aug 13;31(7):422–5.
280. Tzoar N, Jain M. Self-phase modulation in long-geometry optical waveguides. *Phys Rev A*. 1981 Mar 1;23(3):1266–70.
281. OSA | Femtosecond white-light continuum pulses [Internet]. [cited 2020 Nov 28]. Available from: <https://www.osapublishing.org/ol/abstract.cfm?uri=ol-8-1-1>
282. Yang G, Shen YR. Spectral broadening of ultrashort pulses in a nonlinear medium. *Opt Lett*. 1984 Nov 1;9(11):510–2.
283. Alfano RR, Li QX, Jimbo T, Manassah JT, Ho PP. Induced spectral broadening of a weak picosecond pulse in glass produced by an intense picosecond pulse. *Opt Lett*. 1986 Oct 1;11(10):626–8.
284. Keldysh LV. IONIZATION IN THE FIELD OF A STRONG ELECTROMAGNETIC WAVE. *Zh Eksperim Teor Fiz* [Internet]. 1964 Nov 1 [cited 2020 Nov 28];Vol: 47. Available from: <https://www.osti.gov/biblio/4662394-ionization-field-strong-electromagnetic-wave>
285. Chang W, Nazarkin A, Travers J, Nold J, Hölzer P, Joly N, Russell P. Influence of ionization on ultrafast gas-based nonlinear fiber optics. *Opt Express*. 2011 Oct 10;19:21018–27.
286. Chen X, Jullien A, Malvache A, Canova L, Borot A, Trisorio A, Durfee CG, Lopez-Martens R. Generation of 4.3 fs, 1 mJ laser pulses via compression of circularly polarized pulses in a gas-filled hollow-core fiber. *Opt Lett*. 2009 May 15;34(10):1588–90.
287. Vozzi C, Nisoli M, Sansone G, Stagira S, De Silvestri S. Optimal spectral broadening in hollow-fiber compressor systems. *Appl Phys B*. 2005 Mar 1;80(3):285–9.
288. Jeong Y-G, Piccoli R, Ferachou D, Cardin V, Chini M, Hädrich S, Limpert J, Morandotti R, Légaré F, Schmidt BE, Razzari L. Direct compression of 170-fs 50-cycle pulses down to 1.5 cycles with 70% transmission. *Sci Rep*. 2018 Aug 7;8(1):11794.
289. Li W, Zhou X, Lock R, Patchkovskii S, Stolow A, Kapteyn HC, Murnane MM. Time-resolved dynamics in N₂O₄ probed using high harmonic generation. *Science*. 2008 Nov 21;322(5905):1207–11.
290. Koch CP, Lemesko M, Sugny D. Quantum control of molecular rotation. *Rev Mod Phys*. 2019 Sep 18;91(3):035005.
291. Hasegawa H, Ohshima Y. Nonadiabatic Molecular Alignment and Orientation. In: Yamanouchi K, editor. *Progress in ultrafast intense laser science, volume XII*. Cham: Springer; 2015. p. 45–64. (Springer Series in Chemical Physics; vol. 112).

292. Time evolution of pendular states created by the interaction of molecular polarizability with a pulsed nonresonant laser field: *The Journal of Chemical Physics*: Vol 110, No 8 [Internet]. [cited 2020 Nov 28]. Available from: <https://aip.scitation.org/doi/10.1063/1.478241>
293. *Phys. Rev. Lett.* 83, 4971 (1999) - Revival Structure of Aligned Rotational Wave Packets [Internet]. [cited 2020 Nov 28]. Available from: <https://journals.aps.org/prl/abstract/10.1103/PhysRevLett.83.4971>
294. Beetar JE, Nrisimhamurty M, Truong T-C, Nagar GC, Liu Y, Nesper J, Suarez O, Rivas F, Wu Y, Shim B, Chini M. Multioctave supercontinuum generation and frequency conversion based on rotational nonlinearity. *Sci Adv.* 2020 Aug 1;6(34):eabb5375.
295. Zheltikov AM. Understanding the nonlinear phase and frequency shift of an ultrashort light pulse induced by an inertial third-order optical nonlinearity. *Phys Rev A.* 2009 Feb 19;79(2):023823.
296. *Phys. Rev. A* 85, 043820 (2012) - Absolute measurement of the transient optical nonlinearity in N_2 , O_2 , N_2O , and Ar [Internet]. [cited 2021 Jan 17]. Available from: <https://journals.aps.org/prl/abstract/10.1103/PhysRevA.85.043820>
297. Chen H, Song Q, Tang G, Feng Q, Lin L. The Combined Optimization of Savitzky-Golay Smoothing and Multiplicative Scatter Correction for FT-NIR PLS Models [Internet]. Vol. 2013, *ISRN Spectroscopy*. Hindawi; 2013 [cited 2020 Dec 8]. p. e642190. Available from: <https://www.hindawi.com/journals/isrn/2013/642190/>

APPENDIX

Appendix I: Technical aspects of the spectral broadening investigation

(i) Temporal variation of input pulses

The pair of grating inside the compressor (last stage of CPA) is capable of introducing an adjustable amount of group delay dispersion (GDD) which can be used to adjust the pulse temporal duration. Using the pair of gratings, the input pulse duration was scanned to monitor the spectral broadening, since the induced molecular response broadening is associated the molecular rotation time scale. For this purpose, the output of the compression stage was scanned (Figure A) in terms of grating position which provides the required information for adjusting the pulse duration at any time.

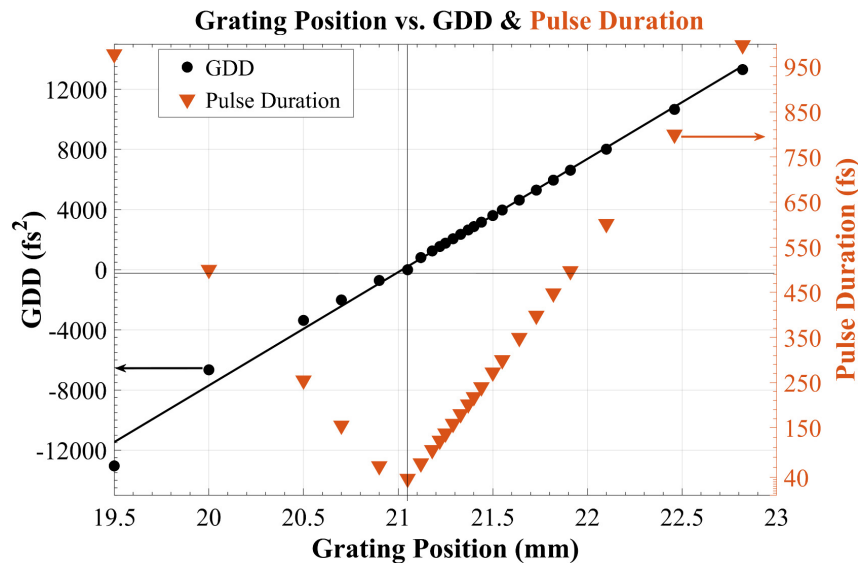


Figure A: Grating position vs. pulse duration. Reference table to change the pulse duration.

This scan was conducted with the help of a SHG FROG (introduced in section 2.3) which is capable of characterizing ultrashort pulses. To improve the accuracy of this measurement, for each grating position, the output pulse was characterized three to five distinct times.

(ii) Gas-filled HCF setup

This experiment is based on the propagation of ultrashort pulses through a gas-filled HCF. To ensure high output vs. input (O/I) transmission, the input beam is focused at the entrance of the fiber to reach a 350 μm focal diameter beam waist (Figure B) which is near $1/e^2$ of the 500 μm HCF core diameter. This ultimately tolerates proper coupling of the beam into the fiber of more than 75% O/I transmission.

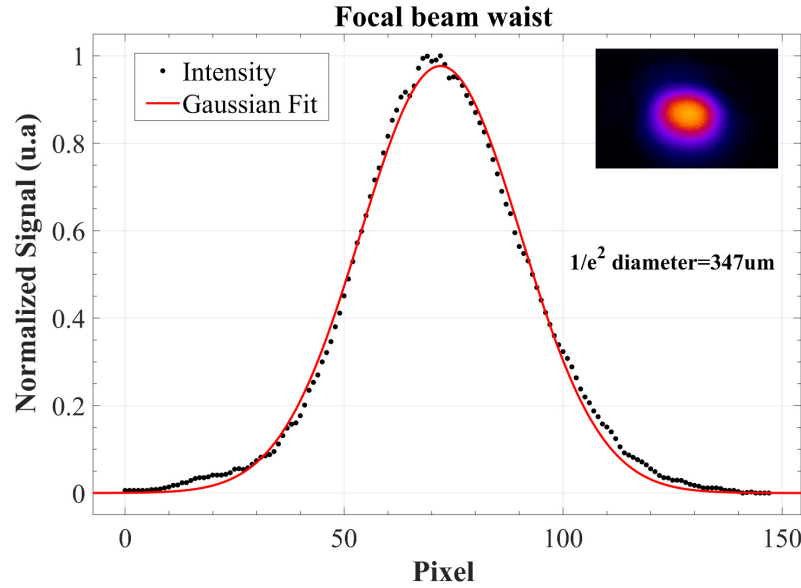


Figure B: Reduction of the beam waist to ensure high O/I transmission inside the HCF.

Our goal here is to study the effect of a specific molecular gas on the spectral broadening of laser pulses. For this purpose, first, we need to eliminate any unwanted gas medium (including $O_2 \sim$ air) and then fill it with the intended gas. To this end, a pumping system was added at the inlet and outlet of the fiber in order to create a pressure differential. This system should be sealed in a way to maintain minimal leakage of the system.

(iii) Leakage of the system

A typical spectral broadening scan vs. input pulse duration (or vs. system pressure) can take a significant amount of time. A study was conducted to understand the influence of gas leaks on the measurements. For this purpose, the system was stabilized at the specific pressure (and a particular input pulse duration) and then spectral measurements were made at several minutes interval.: The output spectrum was recorded every five minutes for a total period of 45 minutes. Figure C shows the result of this study for the system at 200 mbar. At this pressure, the output spectrum remains unchanged for the first 10 minutes, and after that, the spectrum is gradually altered due to air intrusion into the system. This is an issue, since a typical spectral broadening scan vs. input pulse duration takes 30 – 40 minutes (changing the grating for each pulse duration and then carefully replicating the conditions).

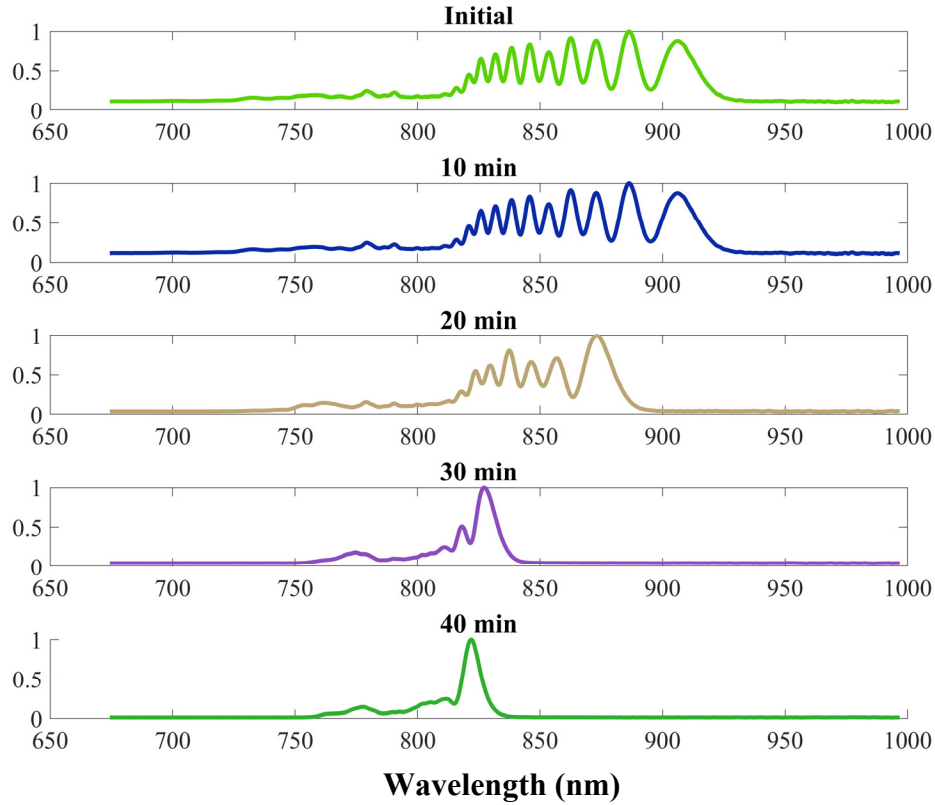


Figure C: Evaluation of the gas contamination by spectral measurements made at different times for a pressure of 200 mbar.

We repeated this study for different system pressures. For example, Figure D represents the case at 1000 mbar. The data recorded over a 45-minute period for 1000 mbar and above are found to be free of any significant alterations.

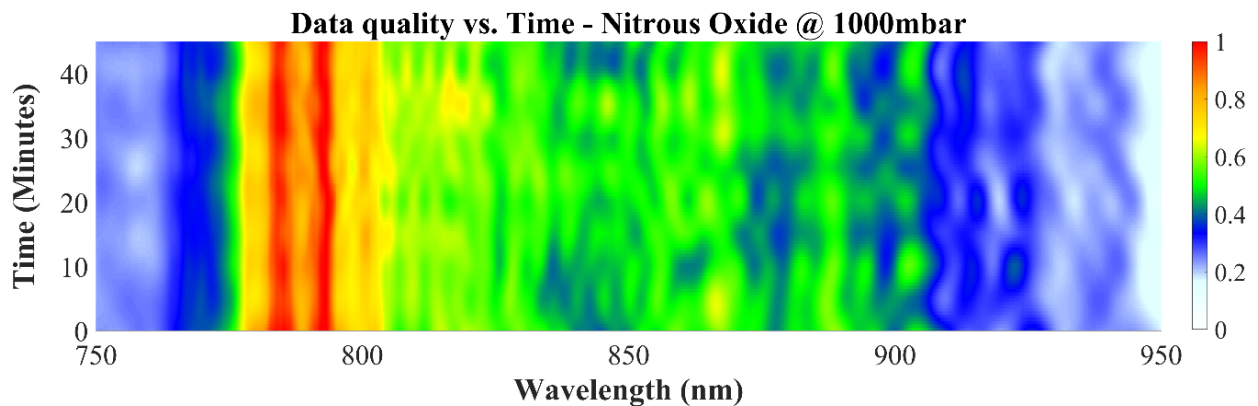


Figure D: External contamination evaluation by scanning the broadening over period of time at 1000 mbar.

In summary, when the system is operating below the room pressure, the open air goes into the HCF due to leakage. On the contrary, while operating over the room pressure, since the system pressure is higher than that of the atmosphere, nothing can enter. To resolve this issue and avoid the contamination of data due to

leakage, during the measurement reported in section 4.3, all gas in the system was evacuated and then refilled with fresh N_2O gas every 10 minutes while working below the atmosphere pressure. To certify the quality of the data, the spectrum in a particular condition was matched before and after changing the atmosphere of the system. Our investigation strongly suggests that following this procedure ensures data quality and reproducibility.

(iv) Data treatment – calibration factor

The spectral broadenings obtained in this study spread the frequencies beyond the range of our basic detector (Avantes spectrometer in the visible: 166.66 to 1160.16 nm). To obtain complete spectra, we used an additional detector (Avantes NIR spectrometer) covering a complementary spectral range between 944.55 and 2495.90 nm.

The spectra were combined by a process called stitching. The two spectrometers share a small spectral range (Figure E) between 944 and 1160 nm, which was used for calibration. However, the response of the spectrometers in this common range is poor. Thus, finding the appropriate calibration factor is not a simple task. In a similar work, a third spectrometer was used to ensure an appropriate calibration between the first two detectors [294].

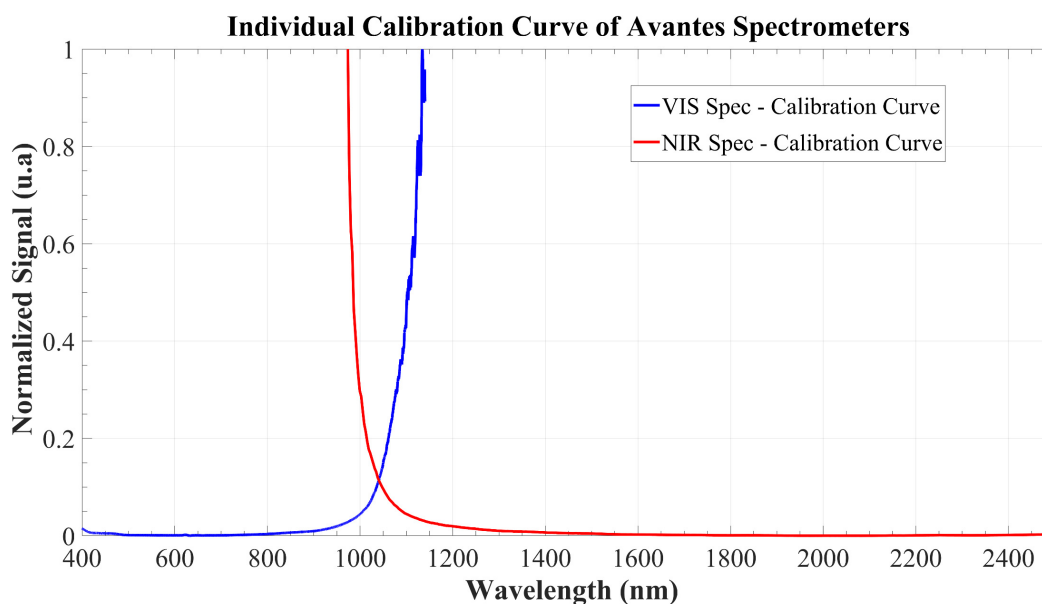


Figure E: Calibration curves of the visible and NIR spectrometers.

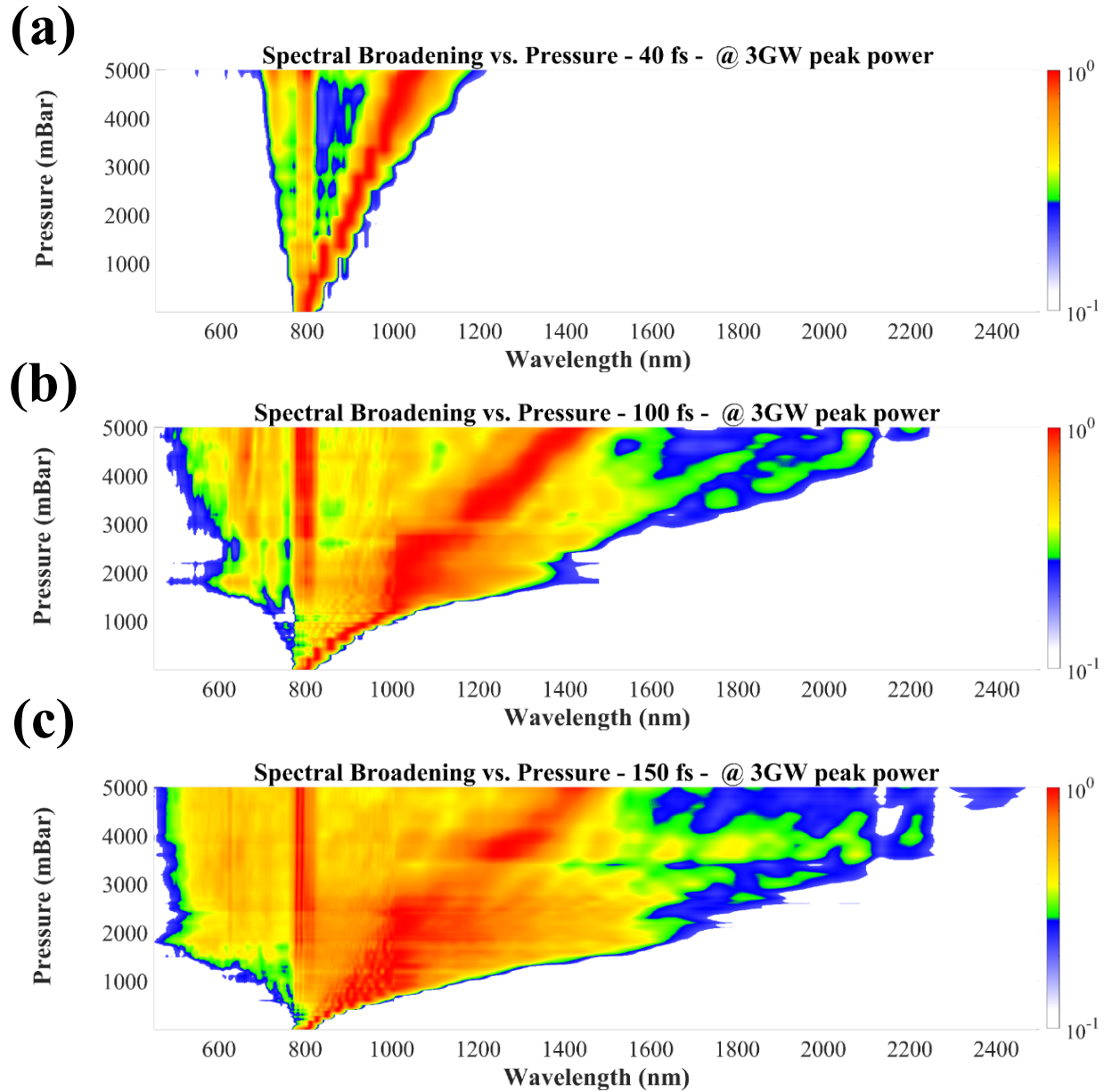
The stitching of the two spectrometers poses two problems. First, the common spectral range does not actually mean that the recorded values are at exactly the same wavelengths. To explain further, the visible spectrometer recorded 535 wavelengths in this common spectral range while the NIR spectrometer recorded only 36 wavelengths in this range. In fact, the resolution of the NIR spectrometer is much lower than that

of the visible spectrometer. In addition, the NIR spectrometer has a higher noise level. To solve this problem, each NIR spectrum was first processed by the Savitzky-Golay filter algorithm [297] and then interpolated. It is worth mentioning that data accuracy was prioritized over smoothness and a narrow-edge filter was used. The second issue when stitching the data is the sensitivity to the shared spectrum range for each of these spectrometers. That is, each has a strong calibration curve (Figure E) that must be accounted for over almost half of the shared range.

Finally, the calibration curve (Figure E) provided by the manufacturer of the visible and NIR spectrometers was first applied to the data to ensure the correct distribution of the intensity signal from each spectrometer. As we have seen previously, there are only a few common wavelengths between these two spectrometers and after several trials, a number of them were chosen to correctly assemble the results from these two spectrometers. The quality of this task is the crucial part of this study since it is necessary to obtain the correct calibration factor of these two spectrometers to analyze the data.

Appendix II: Experimental data for several input pulse durations

The spectral broadening induced by the molecular response of N_2O was discussed in section 4.3. The results of the section 4.3 as well as results for other input pulse durations are presented in this section.

(i) Influence of molecular gas pressure at spectral broadening – 3GW peak power

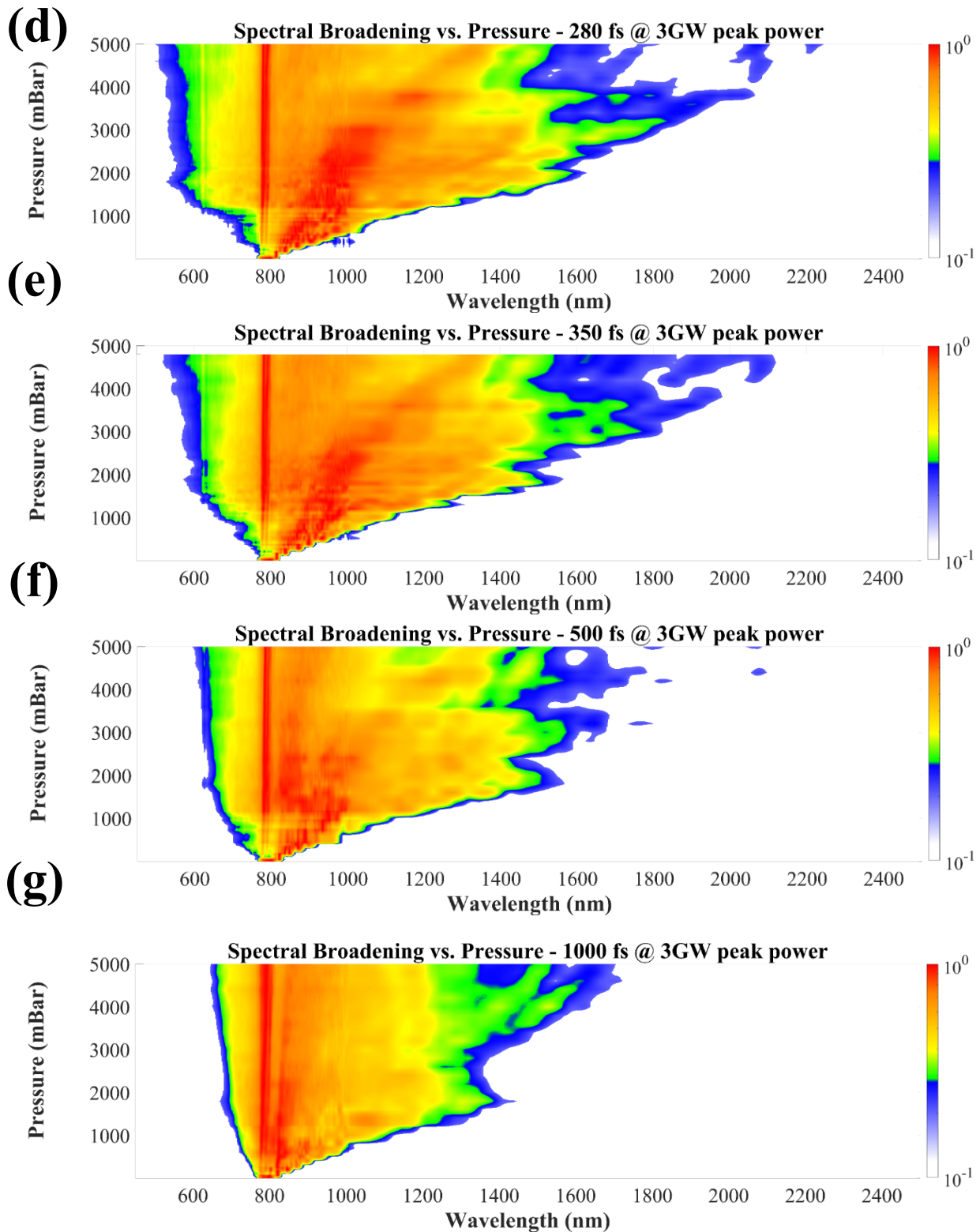


Figure F: Spectral broadening over molecular pressure with 3 GW peak power. Input pulse duration (a): 40 fs, (b): 100 fs, (c): 150 fs, (d): 280 fs, (e): 350fs, (f): 500fs, (g): 1000fs.

(ii) Influence of the molecular gas pressure on the spectral broadening – 8GW peak power:

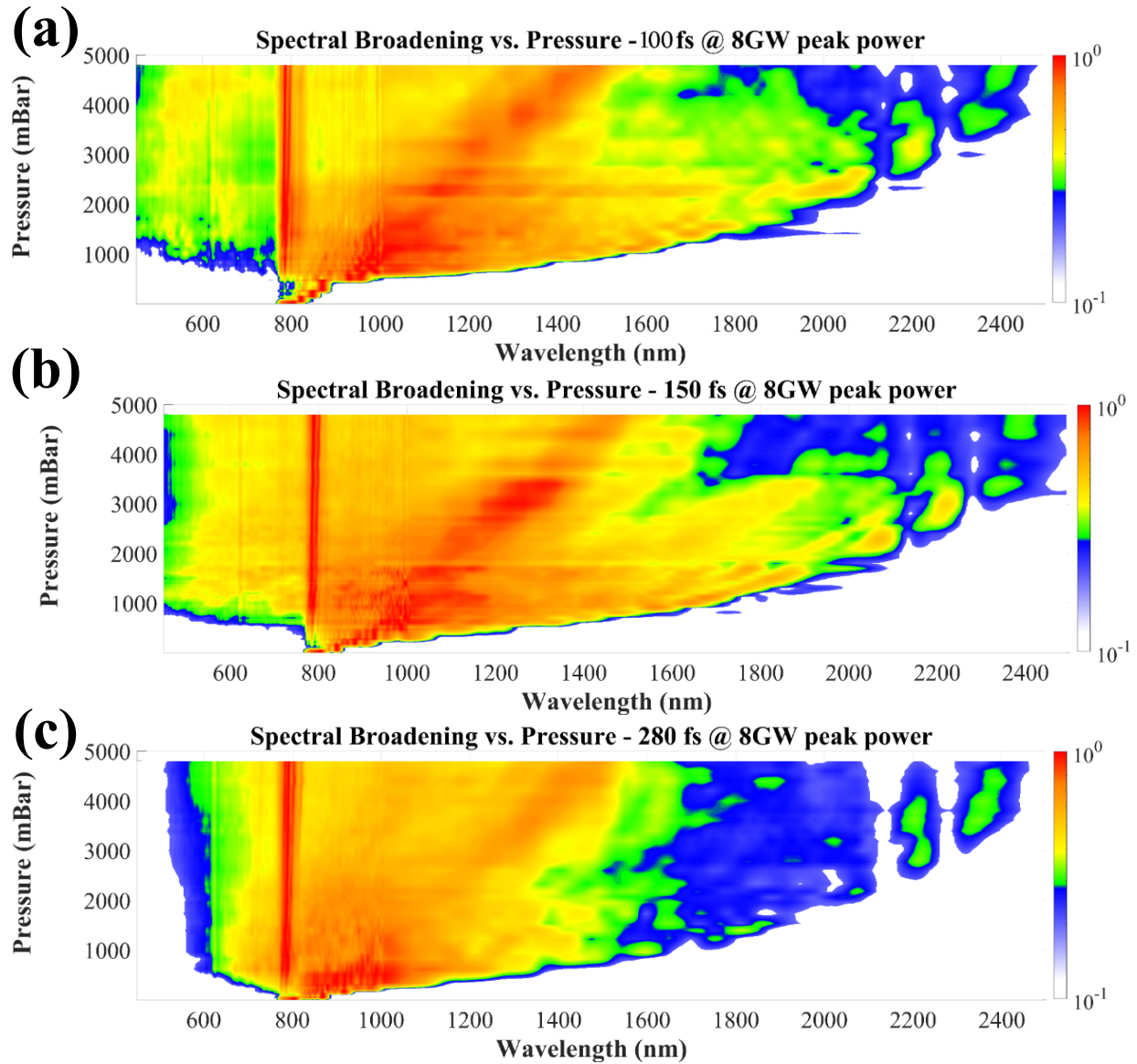


Figure G: Spectral broadening over molecular pressure with 8 GW peak power. Input pulse duration (a): 100 fs, (b): 150 fs, (c): 280 fs.

(iii) Measured HCF transmission vs. pressure:

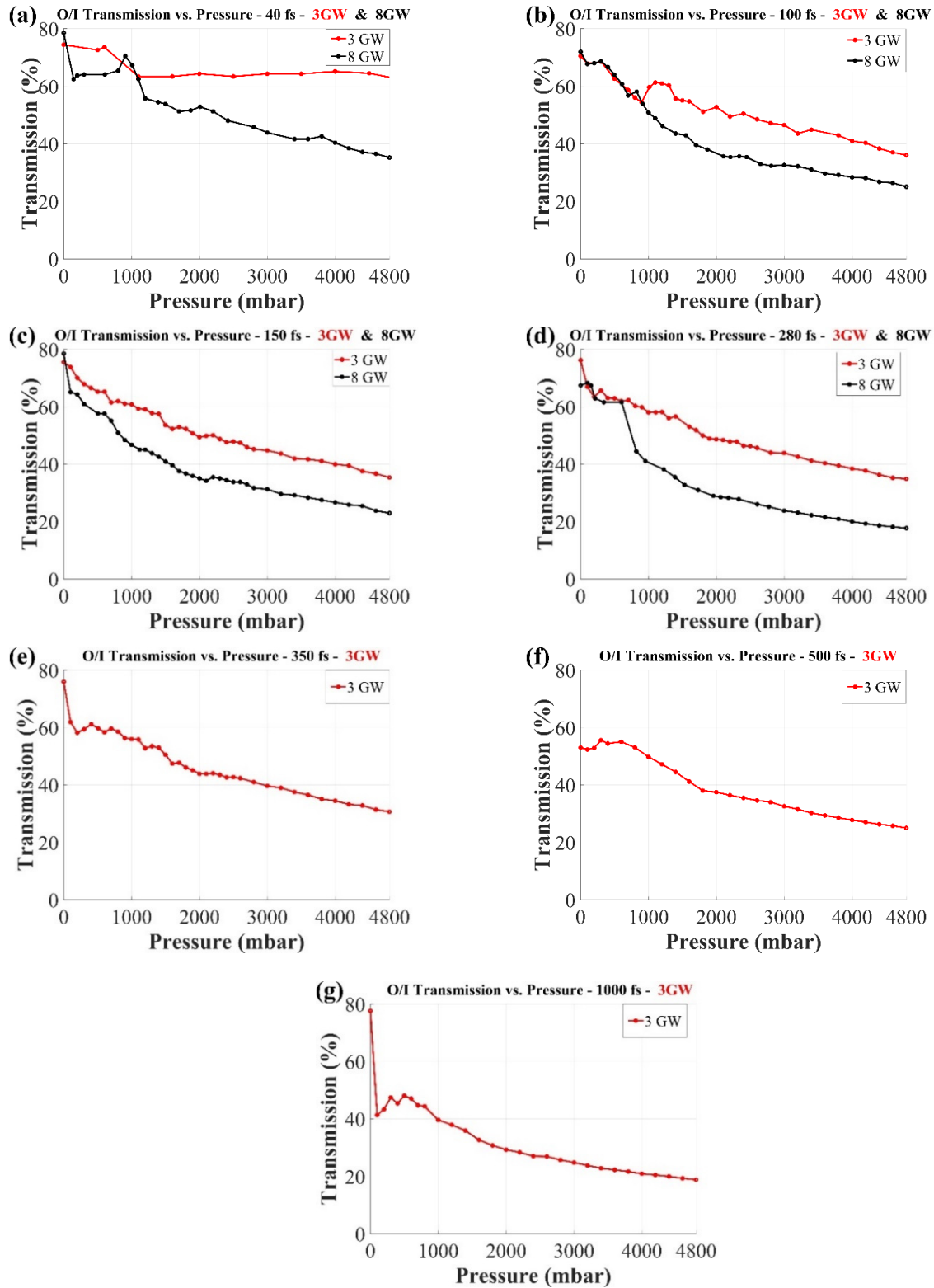


Figure H: Output/Input HCF transmission of the experimental results presented in Figure F and Figure G. (a): 40 fs, (b): 100 fs, (c): 150 fs, (d): 280 fs, (e): 350fs, (f): 500fs, (g): 1000fs.